Dissertation

submitted to the

Combined Faculty of Mathematics, Engineering and Natural Sciences

of Heidelberg University, Germany

for the degree of

Doctor of Natural Sciences

Put forward by

David Freire Fernández

born in: Fuente Vaqueros, Granada, Spain

Oral examination: 21.06.2024

First nuclear two-photon decay measurements at storage rings

Referees: Prof. Dr. Klaus Blaum

Prof. Dr. Johanna Stachel

Erste Messungen des nuklearen Zwei-Photonen-Zerfalls an Speicherringen

Zusammenfassung - In dieser Arbeit wird ein neuartiger Ansatz vorgestellt, bei dem Schottky- und Isochron-Massenspektrometrie (S+IMS) kombiniert werden, um die nukleare Zwei-Photonen- oder Doppel-Gamma-Zerfallsrate (2γ) im Niederenergiebereich unterhalb der Elektron-Positron-Paarbildungsschwelle direkt zu messen. Diese Methode erweitert die zerstörungsfreie Lebensdauerspektroskopie zu kürzerlebigen Spezies ($\gtrsim 1$ ms) und erzielt ein mit IMS bisher noch nie erreichtes Massenauflösungsvermögen von 9.1×10^5. Dank dieser Fähigkeit konnten wir erfolgreich angeregte Zustände mit einer Energie von bis zu 101 keV, wie der des Isomers in ^{72}Br auflösen. Wir haben die Halbwertszeit für den 2γ-Zerfall des ersten angeregten 0^+-Zustands in reinen ^{72}Ge-Ionen mit $23.9\,(6)$ ms bestimmt, ein Ergebnis, das erheblich von den bisherigen Erwartungen abweicht. Diese Abweichung ergibt sich möglicherweise aus der Struktur dieses Kernes im Vergleich zu den Strukturen der bisher gemessenen magischen und doppeltmagischen Kerne. Weitere Untersuchungen sind erforderlich, um diese Diskrepanzen vollständig zu verstehen.

Darüber hinaus präsentiert diese Arbeit einige der präzisesten Massenmessungen, die jemals an Speicherringen durchgeführt wurden. Wir haben insbesondere die Massenunsicherheit für ^{69}As verbessert und eine signifikante Abweichung ($> 3\sigma$) für ^{72}As von den zuvor angegebenen Werten festgestellt.

Diese Ergebnisse zeigen das Potenzial unserer Technik für Massenmessungen und für die Erforschung bisher unzugänglicher nuklearer Zerfallsprozesse und eröffnen dadurch neue Möglichkeiten für künftige Forschungen an Speicherringen.

First nuclear two-photon decay measurements at storage rings

Summary - This thesis introduces a pioneering approach by combining Schottky and Isochronous Mass Spectrometry (S+IMS) to directly measure the nuclear two-photon or double-gamma (2γ) decay rate in the low-energy regime, below the electron-positron pair creation threshold. This method extends non-destructive lifetime spectroscopy to include shorter-lived species ($\gtrsim 1$ ms), and achieves an unprecedented mass resolving power of 9.1×10^5 for IMS. This capability allowed us to successfully resolve excited states, down to the 101 keV isomer in ^{72}Br. We determined the half-life for the 2γ decay of the first-excited 0^+ state in bare ^{72}Ge ions to be $23.9\,(6)$ ms, a finding that significantly diverges from prior expectations. This divergence potentially results from the structure of this mid-shell nucleus in comparison to the structures of the so far measured semi-magic and doubly-magic nuclei. Further investigations are required to fully understand these discrepancies.

Furthermore, this work presents some of the most precise mass measurements ever achieved at storage rings. We notably improved the mass uncertainty for ^{69}As and identified a significant deviation ($> 3\sigma$) for ^{72}As from previously tabulated values.

These results demonstrate the potential of our technique for mass measurements and for exploring nuclear decay pathways previously inaccessible, opening new venues for future research at storage rings.

Acknowledgements

"Yo soy yo y mi circunstancia, y si no la salvo a ella no me salvo yo"
("Ich bin ich und mein Lebensumstand, und wenn ich ihn nicht rette, dann rette ich auch mich nicht.")
— J. Ortega y Gasset, *Meditaciones del Quijote (1914)*

This quote encapsulates the notion that self-understanding is deeply linked with an understanding of one's surroundings. As such, my journey here has been shaped not just by my own actions, but by the world around me. Consequently, **I am thankful to everyone I have ever shared a moment or space with**.

Yet, there are some people I want to thank specifically, those who had a higher weight during my PhD journey (without any preferred order):

- I would like to thank my bachelor colleagues, especially: David Sánchez and Pedro J. Gea.

- Related to my university time, I would also thank my first research colleagues: Joaquín Berrocal, Fran Domínguez and Emilio Altozano.

- An especial mention to Manuel J. Gutiérrez, whom I initially met in Granada and later found again at GSI. Thanks for being a great training partner (when you could make it 😉), and for demonstrating passion for science and learning every day. You truly embody what a PostDoc should be. I wish you the best luck in your future, I am sure you will do great wherever you are.

- Thanks to my GSI colleagues. I truly enjoyed sharing my results (almost) **every** Wednesday, with RuiJiu Chen, Jan Glorius, Yuri Litvinov, Wolfram Korten, Shahab Sanjari and Sophia Dellmann. I thank Alex Gumberidze, Nikos Petridis, Sergiy Trotsenko and Shahab Sanjari for the (free 😄) coffee breaks and the variety of topics we discussed, always with a funny note. I also thank the students who transitioned KBW 3.029 (my office) during this two and half years: George Hudson-Chang, Johannes Krempel-Hesse, Dima Dmytriiev, Ragan Sidhu, Maria Selina, Quanchao Song, among others.

- I thank the people I met during my two months in Orsay. Special mention to Jing, who picked my up at the Paris Bus Station after 9 hours of bus with my bike, backpack, suitcase and a big bag. He showed me the area and even cooked some traditional delicious Chinese food. Following, I thank my Bulgarian friends Desi Kalaydjieva and Konstantin Stoychev. I really enjoyed our trip to Legnaro and surroundings. It would have been really boring without you.

- I thank Johanna Stachel for happily agreeing to act as the second referee of my thesis. It is a privilege to have such a distinguished researcher examine my work from a different perspective.

- Now is the turn for Der Kalligraph von Kermanshah, the supervisor in the shadows, my mentor+colleague+friend Shahab. You are an inspiration and motivation for any student, always with a smile, funny, charismatic, very thoughtful, intelligent and creative, without you GSI would not be the same. Thanks for everything 😉😃.

- I would like to thank Klaus Blaum for welcoming me into his group as a PhD candidate, allowing me to conduct pioneering research, and enabling my doctoral studies at Heidelberg University. Thanks for your time and scientific advice throughout all these years, especially at the last stages of my PhD. Moreover, thanks for the financial support and trust; any opportunity that I got, I could pursue without any doubt. I am still surprised that he is always the first one in answering any email, always with a concise and transparent message 😃. He is an exceptional team leader, and he will continue to be.

- I thank Yuri A. Litvinov (I still have not discovered what the "A." stands for) for providing the best working environment possible at GSI. I thank him for allowing me to conduct independent research, without never ever asking me to do anything outside the scope of my thesis. I also thank him for providing me with the best tools possible for working without questioning, and for his support, advice and expertise.

- I would also like to thank Wolfram Korten, for making the experiment possible, for pushing the theoreticians, and for keeping pursuing the nuclear two-photon decay. I have been in multiple experiments alongside Wolfram, all of them were successful, and I do not think it was a coincidence 😉. I enjoyed working together.

- Finally, I would like to thank the persons with the highest impact, my family. Querría agradecer a mi familia por todo su apoyo a lo largo de mi vida, dándome el lujo de estudiar sin ninguna preocupación. Gracias a mi papá (Paco), a mi mamá (Yolanda), y a mis hermanos Borja y Fran. Ich möchte mich auch bei meiner Schwiegerfamilie bedanken, dass sie mich in die Familie aufgenommen hat, insbesondere bei Lothar und Marlen.

❤ Sophia, du bist das Beste, was mir je passiert ist. Vielen Dank für deine tägliche Unterstützung und Liebe. Neben dir fühle ich, dass ich glücklich strahlen kann, bis zum letzten Akt.

Darmstadt, 08.04.2024

Contents

Chapter 1

Introduction

Within this introductory chapter, I discuss the fundamental concepts and main motivations of the thesis; starting with the discussion of the importance of masses and half-lives of atomic nuclei in §1.1.

To achieve precise measurements, mass spectrometry and half-life spectroscopy techniques are reviewed, with a particular focus on storage ring mass spectrometry as discussed in §1.2.0.2 and in §1.2.1.

Radioactive decays play a pivotal role in nuclear physics, and are shortly explored in §1.3. This includes overviews of alpha decay (§1.3.1), beta decay (§1.3.2), electromagnetic decays (§1.3.3), with a particular emphasis on $E0$ transitions (§1.3.4), each revealing different aspects of nuclear behavior and stability.

Furthermore, the existence of isomers, as addressed in §1.4, offers unique insights into the deformation (§1.4.1) and shape coexistence (§1.4.2) within nuclei. The role of isomers in nucleosynthesis is discussed in §1.4.3.

1.1 Masses and half-lives

Understanding the masses and half-lives of nuclei, along with the reaction rates of nuclear collisions, is crucial for deciphering the underlying principles of nuclear processes. Mass measurements elucidate the energy dynamics within nuclear reactions and decays through the mass-energy equivalence [1] (see Eq. (1.1)). This principle states a direct relationship between the mass of an object and its energy content, stressing the importance of mass in determining the energy release during nuclear decay:

$$E = mc^2. \tag{1.1}$$

A significant consequence of mass-energy equivalence is that the energy released in a nuclear process can be determined simply by measuring the mass difference between the initial (parent nucleus)

and final state (daughter nucleus). This relationship is crucial for the decay to be energetically feasible. A decay process where a lighter mass nucleus would transform into a heavier mass nucleus is not possible under normal circumstances.

The atomic mass unit ($u \approx 931.49\ \mathrm{MeV}/c^2$ [2]) serves as a standardized measure of the mass, defined as $\frac{1}{12}$ the mass of a $^{12}\mathrm{C}$ atom [3]. It is smaller than the mass of a proton ($\sim 938.27\ \mathrm{MeV}/c^2$ [2]) or a neutron ($\sim\ 939.56\ \mathrm{MeV}/c^2$ [2]) since it includes the nuclear and atomic binding energy of the $^{12}\mathrm{C}$ atom constituents. The concept of mass excess (defect) makes more convenient to quantify the nuclear binding energy and the energetics of nuclear reactions, therefore it is more commonly used to tabulate atomic masses. The mass excess of an atom with A nucleons is defined as:

$$\Delta M = M_{\mathrm{atom}} - A \cdot u. \tag{1.2}$$

As a consequence, the mass excess for $^{12}\mathrm{C}$ atom is 0.

Most of the mass measurements (see §1.2) yield atomic masses M_{atom} or masses of ions. The nuclear mass M_{nuclear} can be obtained by accounting for electron masses M_{e^-}, the binding energies B_{e^-} of electrons, the proton number Z and (if applicable) the excitation energy ω:

$$M_{\mathrm{nuclear}} = M_{\mathrm{atom}} - Z \cdot M_{e^-} + \frac{B_{e^-}(Z)}{c^2} + \frac{\omega}{c^2}. \tag{1.3}$$

Since compared to the masses of protons and neutrons (even to the electron mass), the electron binding energies are small (often in the order of a few eV to keV), they usually can be neglected in calculations. Although, not when performing high-precision measurements, as e.g. with the Penning-trap mass spectrometer PENTATRAP [4] on highly charged ions [5].

On the other hand, the half-life of a nuclear state reflects its stability. Short-lived states indicate less stable configurations, while long-lived states suggest greater stability. Measuring the half-life of an excited nuclear state or a radioactive isotope gives insights into the nuclear structure through the dynamics of nuclear reactions and decay processes.

These measurements are essential in nuclear astrophysics, particularly in understanding stellar nucleosynthesis [6] (more information in §1.4.3). In addition, half-lives and reaction rates of subatomic particles and nuclei can be used to test the predictions of the Standard Model [7], providing opportunities to discover new physics [8] or confirm existing theories. Knowledge of nuclear lifetimes and reaction rates is also crucial in various applications, such as nuclear medicine by using radioisotopes.

1.2 Mass-and half-life spectrometry

The fields of mass spectrometry and half-life spectroscopy have been dominated mainly by Penning traps (§1.2.0.1) and storage rings (§1.2.0.2), both based on stored ions [9]. Their main differences

originate from their geometry, i.e. the volume in which the ions are confined, which constrains the energy of the stored ions.

1.2.0.1 Penning traps

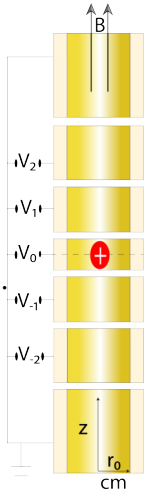

In Penning traps, the ions are confined in very small volumes ($\sim$ cm^3) by the superposition of a constant magnetic field in the axial direction (confining therefore in the radial direction) and a quadrupolar electrostatic potential for confining in the axial direction [10]. This allows for extremely precise manipulation and control over the ions, which translates into ultra high-precision mass measurements [11, 12].

The most precise mass measurements are realized by this technique, specially of stable species [13]. Stable since, the potential well in which the ions are trapped is too shallow and low in energy, therefore if radioactive isotopes are produced, they need extensive cooling to reach a few kiloelectronvolts before trapping them, this takes time, limiting the half-lives to milliseconds. Also, the number of interactions between the confined ions is reduced to the Coulomb repulsion, due to the small energies. Therefore, unlike in storage rings, no nuclear reactions with targets, e.g. proton capture, can be observed.

1.2.0.2 Storage rings

On the other hand, we have storage rings [14] where the ions are confined with relativistic energies in huge ellipsoid-like volumes ($\sim$ m^3), and even more due to the periodicity of the ring, this volume is extended N times if the ions revolve N times the storage ring. This offers unique capabilities no other mass spectrometry technique can offer.

This large volume allows for the simultaneous storage and manipulation of various ion species, in contrast to traps. When coupled to an in-flight radioactive-ion beam production facility, this set-up enables the simultaneous measurement of masses and half-lives of short-lived (exotic) nuclear states. It also enables the detection of decays with large Q values, as the daughter particles remain confined within the (large) volume [15]. The ability to place targets at fixed positions in storage rings facilitates a higher number of reactions and interactions, which is crucial for studies of nuclear reactions, simulating astrophysical conditions [16–18], such as with proton targets [19] (or, in the future, neutron targets [20, 21]). The capability to recirculate enhances the number of reactions (luminosity) without necessitating denser targets. However, the drawbacks compared to Penning traps include more complex ion dynamics and, a priori, lower precision in mass measurements for species that can be measured by Penning traps.

In the context of this thesis, the term STORAGE RINGS specifically refer to heavy-ion storage rings. Currently, there are three in operation: the COOLER-STORAGE RING [22] (CSRe) at the Institute of Modern Physics (IMP) of the Chinese Academy of Sciences, the RARE RI

RING [23] (R3) at RIKEN, and the, firstly developed, EXPERIMENTAL STORAGE RING [24] (ESR) at the Gesellschaft für Schwerionenforschung (GSI).

1.2.1 Storage ring mass spectrometry

At storage rings (like the one in Fig. 3.3), the revolution frequency (f) of the revolving ions is related to the mass-over-charge (m/q) ratio and to the velocity spread (Δv) by the relation [25]:

$$\frac{\Delta f}{f} = -\frac{1}{\gamma_t^2}\frac{\Delta(m/q)}{m/q} + \left(1 - \frac{\gamma^2}{\gamma_t^2}\right)\frac{\Delta v}{v}, \tag{1.4}$$

where v and γ are the velocity and the Lorentz factor of the ions, respectively. The machine parameter γ_t is related to the relative change of the orbit length, C, caused by a relative change of magnetic rigidity [26]:

$$B\rho = mv\gamma/q. \tag{1.5}$$

Ideally, we would like to have a one-to-one mapping between a specific revolution frequency and a unique mass-to-charge ratio. However, the second term in Eq. (1.4) prohibits this. Mathematically, if we would like to eliminate this second term we could: either reduce the momentum spread between ions to zero ($\Delta v \to 0$) or cancel out the term in parentheses by tuning $\gamma \to \gamma_t$. Based on these two approaches, two different mass spectrometry techniques emerge: SCHOTTKY MASS SPECTROMETRY [27] (SMS) and ISOCHRONOUS MASS SPECTROMETRY [28] (IMS).

1.2.1.1 SMS

This technique, sketched in Fig. 1.1, focuses on minimizing the velocity spread (Δv) of the ions as much as possible, usually achieving relative velocity spreads of $\Delta v/v \sim 10^{-7}$ [29] for particle numbers $< 10^3$, which suites radionuclides. This is accomplished by employing advanced cooling methods to stabilize the ion velocities (more on this in §1.2.2). Therefore, this technique should be known as COOLED MASS SPECTROMETRY (CMS), although traditionally CMS is accompanied by the use of SCHOTTKY DETECTORS (more in §3.1.3.1), hence the name Schottky Mass Spectrometry (SMS). Schottky detectors are used due to their non-destructive nature, i.e. they do not modify the benefits obtained at cooling.

1.2.1.2 IMS

In contrast, IMS aims to align the Lorentz factor of the ions (γ) with the TRANSITION ENERGY (γ_t). This is done by fine-tuning the energy of the ions so that it closely matches the ion-optical parameter γ_t, creating a condition where the mass measurement is less affected by the velocity spread of the ions. This arises because, although the velocity spread remains unchanged, particles with different velocities follow different paths, with the fastest particles travelling a longer path

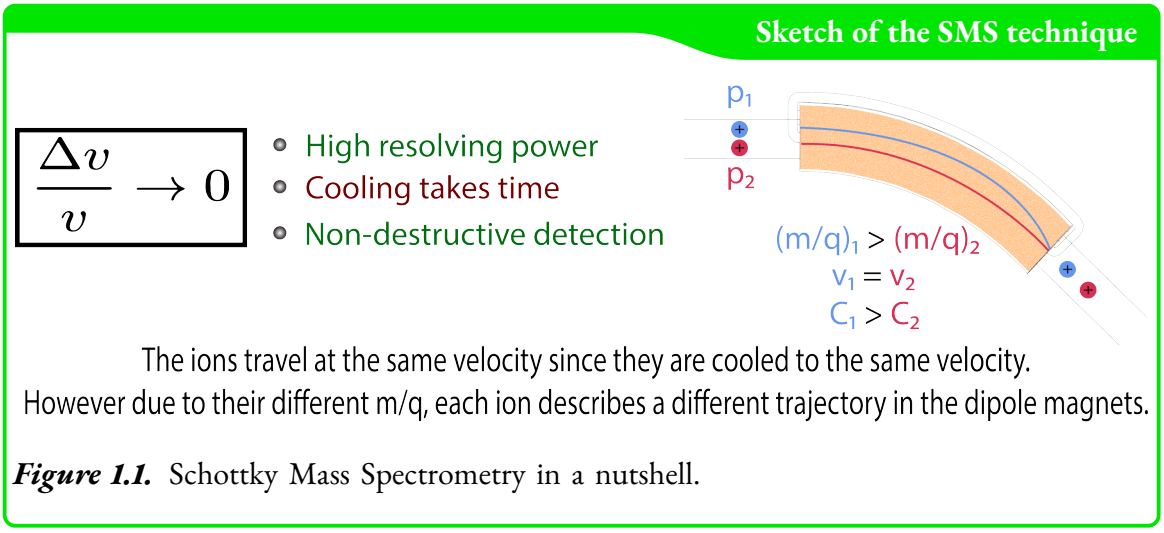

Figure 1.1. Schottky Mass Spectrometry in a nutshell.

compared to the slowest. This difference in path length compensates the velocity spread [30], in such a way that the particles are ISOCHRONOUS to the detectors. In this case, the term IMS is based on the operation mode of the storage ring, the isochronous. A sketch of this technique is shown in Fig. 1.2.

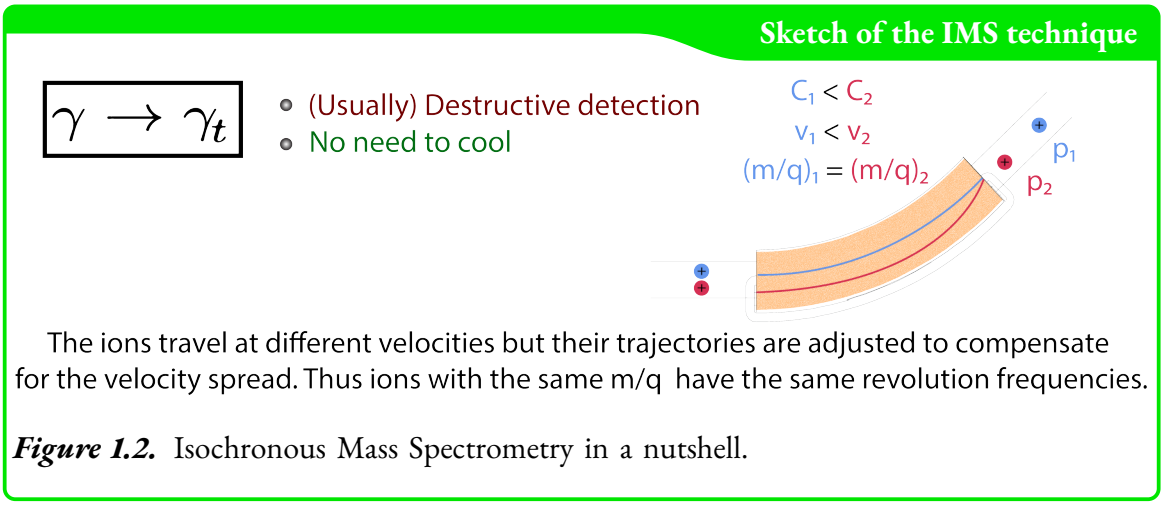

Figure 1.2. Isochronous Mass Spectrometry in a nutshell.

1.2.2 Cooling at storage rings

The main cooling techniques that we can find at storage rings are electron cooling [31] (§1.2.2.1) and stochastic cooling [32] (§1.2.2.2). Laser cooling [33] could also be utilized for reaching temperatures of a few Kelvin.

Beam cooling is a vital process in storage rings. It involves reducing the beam temperature, or equivalently decreasing its phase space volume, emittance, and momentum spread. Moreover, we can control the energy of the electrons (via the application of different voltages), and thus the energy of the ions. This is fundamental for determining the transition energy [30] of the storage ring. Due to the application of cooling forces, which involves interactions between different particles

such as electrons or photons, beam cooling techniques do not follow Liouville's Theorem.

According to Liouville's theorem, in systems governed by conservative forces, the area occupied by the beam in the longitudinal phase space is, like an incompressible fluid, conserved. For performing precision experiments we need to decrease it. Decreasing emittance involves reducing the mean transverse momentum while maintaining the mean longitudinal momentum, done through dissipative forces, i.e. cooling methods. Therefore, cooling is useful for compensating the heating effects in experiments with internal targets and reducing the momentum spread hence increasing the mass resolving power and precision.

1.2.2.1 Electron cooling (in the ESR)

Electron cooling is a technique where the ions adopt the velocity and divergence characteristics of the electron beam. It is based on aligning the parallel velocities ($v_{e\|}$ and $v_{ion\|}$) and the energy relation $E_e = \frac{m_e}{M_{ion}} \cdot E_{ion}$. For instance, 200 keV electrons can cool 400 MeV/u ions. With this method, momentum spreads of $\delta p/p = 10^{-7}$ can be achieved [34], for less than about 10^3 ions.

As a consequence of being able to control the energy of the revolving ions through the electron cooler, we can search for the energy at which $\gamma = \gamma_t$. More on this in §3.2.

1.2.2.2 Stochastic cooling (in the ESR)

Stochastic cooling is a method of "self-correction" of ion trajectories. It involves measuring the ion beam position at a fixed point using a pick-up probe and amplifying the induced signal. This amplified signal serves as a corrective input at another position via a "kicker". This method is used at storage rings for fast pre-cooling of hot fragment beams with energies of 400 MeV/nucleon. With this technique, relative momentum spreads of $\delta p/p \approx 10^{-3}$ can be achieved [35]. Usually, electron cooling follows stochastic cooling.

1.3 Radioactive decays

1.3.1 α decay

Alpha decay is a type of radioactive decay in which an atomic nucleus emits an alpha particle (consisting of two protons and two neutrons) and transforms into a new nucleus with a mass number reduced by four and an atomic number reduced by two. The alpha particle, $^4\mathrm{He}$, is extremely stable due to its strong binding. This strong binding energy is a key reason for α-decay existence. α-decay is governed by both strong and electromagnetic forces, resulting in half-lives that span from microseconds to millions of years.

1.3.2 β decay

β decay represents a fundamental process in particle and nuclear physics, involving the transformation of a neutron into a proton or vice versa, mediated by the weak nuclear force. This process is crucial for understanding nuclear synthesis in astrophysical contexts and the behavior of unstable nuclei. It connects two neighboring isobars. β decay comprises the following variants:

- $\boldsymbol{\beta^-}$ **:** $\boldsymbol{n \rightarrow p + e^- + \overline{\nu}}$ (THREE-BODY β^- DECAY)
  - A neutron (n) in the nucleus transforms into a proton (p), emitting an electron (e^-) and an antineutrino ($\overline{\nu}$)
  - The free neutron decay can occur [36], releasing 0.782 MeV of energy.
- $\boldsymbol{\beta^+}$ **:** $\boldsymbol{p \rightarrow n + e^+ + \nu}$ (THREE-BODY β^+ DECAY)
  - Involves the transformation of a proton into a neutron, emitting a positron (e^+) and a neutrino (ν).
  - Since the mass of the neutron is greater than the proton mass, this decay is only observed within the nucleus (not in "vacuum", as the (free) neutron decay).
- **EC:** $\boldsymbol{p + e^- \rightarrow n + \nu}$ (TWO-BODY β^+ DECAY)
  - A proton captures an inner-shell electron, transforming into a neutron and emitting a neutrino.
  - It competes with the (three-body) β^+ decay, and is energetically more favorable due to the high probability of inner-shell electrons being near the nucleus. Additionally, (three-body) β^+ decay requires an extra 0.511 MeV of energy to create the e^+.

There are other more exotic forms of β-decay such as the double-beta decay and the neutrinoless double-beta decay.

1.3.2.1 Double-beta decay

The double-beta decay, firstly described by M. Göppert-Mayer [37], occurs when single-beta decay is forbidden or highly suppressed. In this rare process, two neutrons in a nucleus simultaneously decay into two protons, emitting two electrons and, following the logic of single β-decay, two antineutrinos.

The hypothetical case where no antineutrinos are emitted is known as NEUTRINOLESS DOUBLE-BETA DECAY. This process, if observed, would have significant implications for our understanding of neutrino properties, including the possibility that neutrinos are their own antiparticles [38]. The nuclear matrix elements (NME) involved in this exotic decay [39] are correlated with the ones of the two-photon decay [40], hence increasing the interest and importance of two-photon NME measurements.

1.3.3 Electromagnetic decays

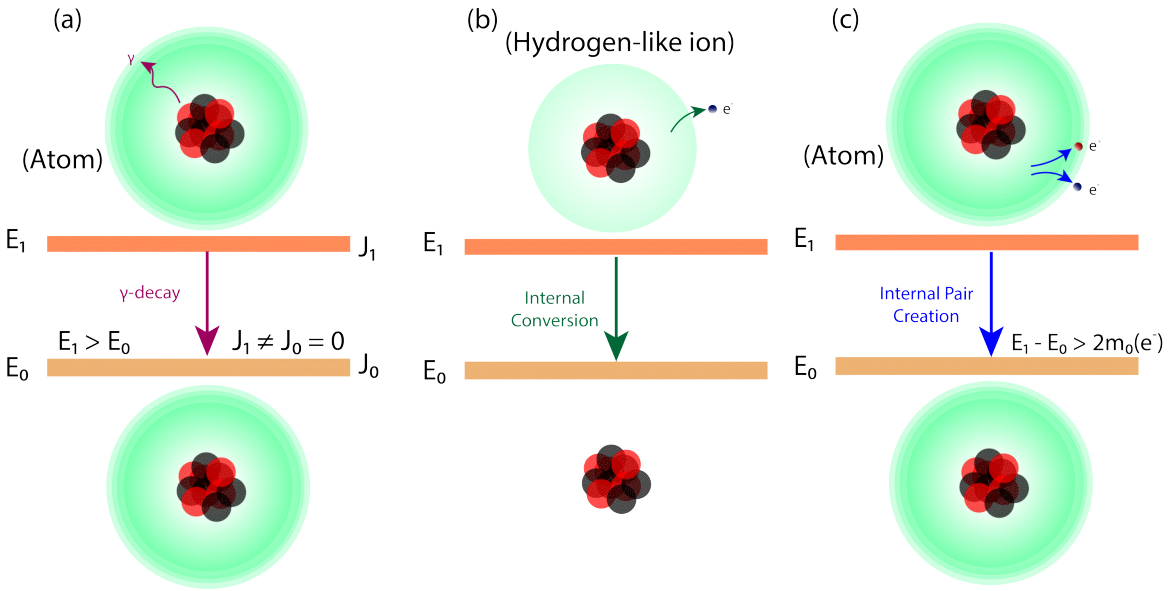

Figure 1.3. Electromagnetic nuclear deexcitations. (a) Gamma decay, (b) internal conversion in a hydrogen-like ion and (c) internal pair creation.

The first order electromagnetic decay pathways: pair creation (§1.3.3.3), internal-electron conversion (§1.3.3.2), and gamma decay (§1.3.3.1) play a pivotal role in nuclear physics by providing detailed insights into nuclear structure.

1.3.3.1 γ decay

Photon decay (γ decay) is one of the main electromagnetic processes, in which an excited nucleus releases excess energy by emitting a γ-ray. This emission typically follows α (§1.3.1) or β-decay (§1.3.2), facilitating the transition of the nucleus to a more energetically favorable state through the reconfiguration of nucleons within nuclear shells.

The rates of γ decay are primarily dictated by electromagnetic interactions. One of the most famous approaches to estimating single-particle transition rates, where nucleon-nucleon interactions are largely neglected, was developed by Weißkopf [41]. His estimates (represented in Fig. 1.4) provide a foundational benchmark for comparing experimental transition rates. According to Weißkopf [41], the transition rate is proportional to the $2L + 1$ power of the transition energy, where L denotes the multipolarity of the decay radiation. Notably, transitions of higher multipolarity exhibit reduced rates as can be seen in Fig. 1.4.

γ-spectroscopy [42] has emerged as an indispensable tool in nuclear physics, yielding precise insights into nuclear structure through the determination of spin, parity, and energy levels. The technique's prowess lies in its ability to directly measure the energy from the γ-ray spectrum, deduce spin via their angular distributions and correlations, and ascertain parity by analyzing

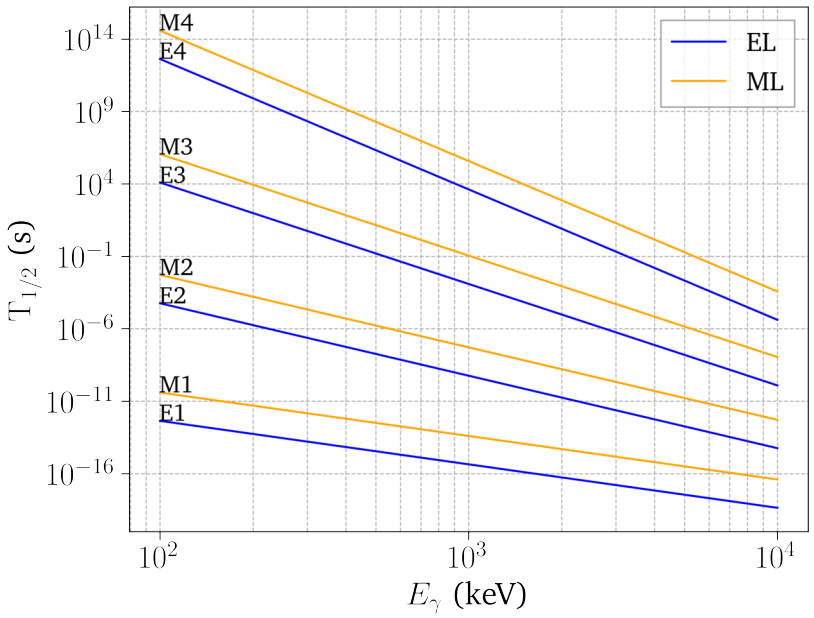

Figure 1.4. Weißkopf estimates of half-lives for various multipolarities (L) in magnetic (M) and electric (E) single-photon decay modes, shown in orange and blue, respectively. These are plotted as a function of the emitted photon energy (E_γ).

the polarization of γ-rays. γ-spectrometers typically consist of arrays composed of segmented high-purity germanium (HPGe) detectors, arranged in spherical configurations, often referred to as DETECTOR BALLS, to measure in all directions. These HPGe detectors are renowned for their exceptional resolution in measuring the energy of gamma rays. Currently, AGATA [43] (Advanced Gamma Tracking Array) is one of the most advanced [44, 45] HPGe balls. For a multitude of excited nuclear states, γ-ray emission constitutes the primary decay pathway to a lower energy state. As a consequence of its intrinsic spin of 1, for preserving the angular momentum in the transitions, $E0$ single-γ decay is not allowed. This point is more addressed in §1.3.4.

1.3.3.2 Internal-electron conversion

Internal-electron conversion (IC) is a process whereby an excited nucleus transfers energy to an orbital electron, ejecting it from the atom. The electron is ejected with a certain kinetic energy determined by the binding energies of the electrons in the specific atomic shell they are ejected from. This mechanism competes with γ decay, particularly in low-energy transitions and environments with high electron densities. Both transitions are grouped under the name of internal transition (IT), as they typically occur between internal levels within the nucleus. The ratio of the probability of emitting an electron versus a photon is termed electron conversion factor (α). It can

be related to the half-lives of each decay by:

$$\alpha = \frac{T^{\gamma}_{1/2}}{T^{IC}_{1/2}}, \tag{1.6}$$

where $T^{\gamma}_{1/2}$ is the partial half-life of the photon decay and $T^{IC}_{1/2}$ is the partial half-life of the internal-electron conversion (IC). Assuming that the neutral state's IT half-life ($T^{IT}_{1/2}$) is measured with high precision and the corresponding α factor value is reliable, we can leverage this information to establish a relationship between them and the pure (partial) γ-decay half-life:

$$T^{IT}_{1/2} = \frac{1}{\frac{1}{T^{\gamma}_{1/2}} + \frac{1}{T^{IC}_{1/2}}} = \frac{1}{\frac{1}{T^{\gamma}_{1/2}} + \frac{\alpha}{T^{\gamma}_{1/2}}}, \tag{1.7}$$

$$T^{\gamma}_{1/2} = T^{IT}_{1/2} \cdot (1 + \alpha). \tag{1.8}$$

Equivalently, considering that the majority of the α factors documented are derived from theoretical models, such as those found in BRICC [46], it follows that by measuring $T^{\gamma}_{1/2}$, we can indirectly determine α through the equation:

$$\alpha = \frac{T^{\gamma}_{1/2}}{T^{IT}_{1/2}} - 1. \tag{1.9}$$

For additional details on the methodology for experimentally estimating α factors, please refer to §4.6.2.

1.3.3.3 Internal pair creation

In internal pair creation, an excited nucleus decays by converting its excess energy into an electron-positron pair. This process becomes energetically feasible for transitions with energies exceeding twice the rest mass of an electron (1.022 MeV).

1.3.4 $E0$ transitions

$E0$ transitions are electric monopole transitions where there is no change in angular momentum ($\Delta J = 0$) and no emission of angular momentum by the nucleus, therefore single γ decay is prohibited. These transitions are often observed through internal conversion processes, providing unique insights into nuclear shape coexistence and isomeric states.

1.4 Isomers

By definition, an isomer or isomeric state is a metastable excited state of a nucleus. There are differing opinions regarding the exact definition of metastable; some consider a state to be metastable if

its half-life is at least in the order of microseconds, while others define it based on having a longer half-life compared to other excited states. They usually decay in stable nuclides via IT to the ground state (see §1.3.3.2).

In the context of this thesis, when referring to EXCITED STATES, we specifically mean states of the nucleus where protons and/or neutrons are excited to higher internal levels. Nuclear excitations are significantly more energetic compared to atomic excitations, typically ranging from a few electronvolts to several kiloelectronvolts for highly bound states, whereas nuclear excitations can reach several megaelectronvolts.

They can be utilized for energy storage [47] and subsequent (stimulated) release [48] (high-energy gamma sources), in medicine dominated primarily by ^{99m}Tc [49]. Additionally, they are the future for nuclear clocks, such as ^{229m}Th [50, 51] and ^{45m}Sc [52].

Metastable states are often described as energy traps [53]. In the same way that the ground state usually[1] represents the most stable configuration of the nucleus, typically corresponding to the state of minimal energy, there are other energy minima that the nucleus, as a whole, can occupy. The stability of these states varies depending on the depth of the energy trap; deeper traps correspond to more stable states.

What has greater mass: an isomer or its corresponding ground state?

An isomer has a greater mass because it represents a less tightly bound system than its corresponding ground state since the nucleons are in excited levels. In other words, the binding energy per nucleon is reduced compared to the one of the ground state.
Another way to look at it is by the energy equivalence theorem, the excitation energy adds up to the mass of the nucleus in the ground state. Consequently, an isomer will **always** exhibit a longer revolution time (lower revolution frequency) than its ground state in storage rings. Thus, in Schottky frequency spectrograms, the isomer will consistently appear to the left of the ground state.

There are primarily three classes of traps (isomers):

- **Spin traps:** those due to significant spin differences between states, leading to spin isomers.
- **Shape traps:** those due to disparities in nuclear deformation within the nucleus, leading to shape coexistence and shape isomers.
- **K traps:** those due to differences in the projection of spin along the axis of symmetry in a deformed nucleus, leading to K isomers.

There are various types of isomers [54, 55], however our focus will be on shape isomers, as they are usually present in low-lying 0^+ excited states [55] and this is the target states of our new

[1] Except for ^{180m}Ta which is stable when ^{180g}Ta is not.

developed methodology. To comprehend shape isomers, it is essential to understand the shape of the nucleus and its possible deformations.

1.4.1 Deformation

Far from closed shells, where the nuclei usually have spherical shapes (specially even-even nuclei), nuclei can exhibit stable deformations. In this subsection, I provide a simple review of the formalism used to describe nuclear deformations.

It is common to parametrize the surface of a deformed nucleus by expressing its radius R in terms of spherical harmonics [56]:

$$R(\theta, \phi; t) = R_0 \left(1 + \sum_{\lambda=0}^{\infty} \sum_{\mu=-\lambda}^{\lambda} \alpha_{\lambda\mu}(t)\, Y_\lambda^\mu(\theta, \phi)\right), \tag{1.10}$$

where R_0 denotes the radius of a spherical nucleus with equivalent volume. In the context of low-energy excitations, the summation over multipole orders λ is typically restricted to $\lambda \geq 2$. This is because the $\lambda = 0$ term, representing the breathing mode, involves changes in the nuclear radius (or volume), which are negligible due to the high incompressibility of nuclear matter. Additionally, $\lambda = 1$ corresponds to shifts in the center of mass of the nucleus, therefore they have no effect on the shape. Also, higher order excitations are only relevant in heavy nuclei ($A > 120$). Fig. 1.5 shows schematically how a spherical nucleus (orange) is deformed under the different excitations (blue). All the deformation figures have been realized with the PYTHON library NUDEFORM [57].

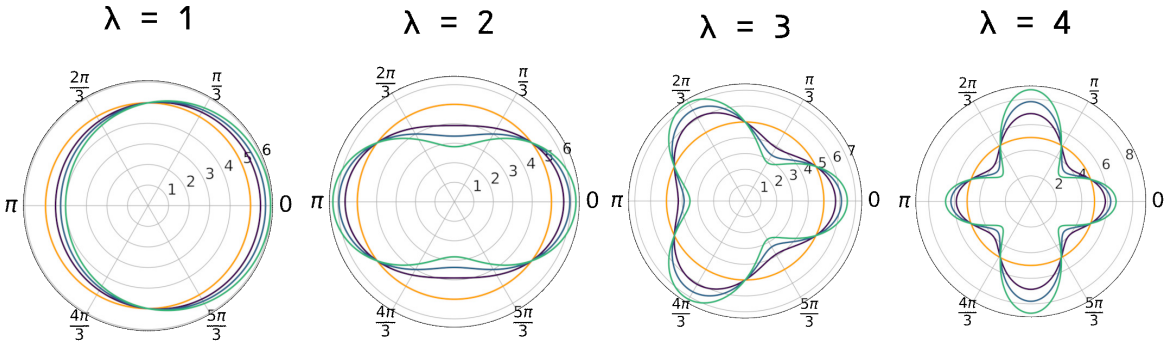

Figure 1.5. Deformation poles for three different β strengths, in comparison with a spherical shape in orange; $\lambda = 1$ (dipole excitations), $\lambda = 2$ (quadrupole excitations), $\lambda = 3$ (octupole excitations), and $\lambda = 4$ (hexadecupole excitations).

The most prevalent deformation in nuclei is quadrupolar ($\lambda = 2$), which creates an ellipsoid-like shape (rugby balls, berliners and everything in between as in Fig. 1.6). For such deformations, there are five deformation coefficients, $\alpha_{\lambda\mu}$. Among these, three coefficients represent the orientation of the body-fixed system in relation to the space-fixed system, corresponding to the three Euler angles.

In the body-fixed framework, the complexity of the five coefficients $\alpha_{\lambda\mu}$ reduces to just two real independent variables: a_{20} and $a_{22} = a_{2-2}$, with $a_{21} = a_{2-1} = 0$. These two variables, along with the three Euler angles, comprehensively describe the system. Usually, the parameters a_{20} and a_{22} are rewritten in terms of the Hill-Wheeler parameters β and γ, which offer a more intuitive understanding of the deformation characteristics.

$$a_{20} = \beta \cos(\gamma) \tag{1.11}$$

$$a_{22} = \frac{1}{\sqrt{2}} \beta \sin(\gamma) \tag{1.12}$$

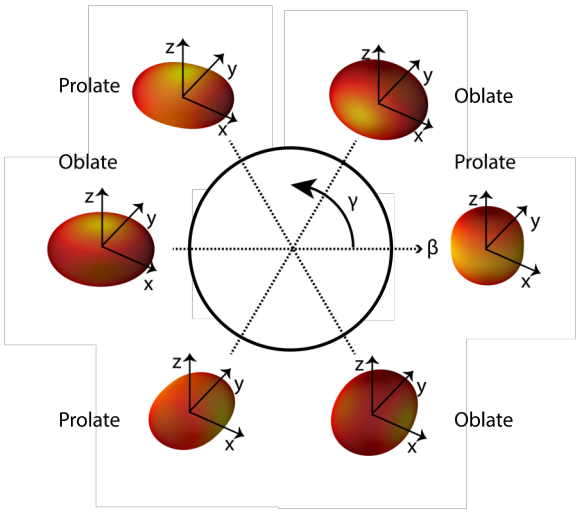

Figure 1.6. Representation of the shape of nuclei with 72 nucleons for a non-zero quadrupolar deformation strength ($\beta > 0$) as a function of the γ angle. The diagram is divided into 6 equal parts, following Lund's conventions.

The parameter β ($\beta \geq 0$) quantifies the degree of ellipsoidal deformation, whereas γ indicates its orientation. The range of γ extends from $0°$ to $360°$. However, according to the Lund convention, it is sufficient to consider the range from $0°$ to $60°$ for representing different nuclear shapes, as the remaining sectors (each of the six segments) simply replicate these shapes along different axes.

At $\gamma = 0°$, the nucleus presents a prolate shape (rugby-like shape) due to symmetry between two of the three axes. Conversely, at $\gamma = 60°$, the shape is oblate (berliner-like shape) with similar symmetry properties. For intermediate values of γ, the nucleus exhibits triaxial shapes, where no symmetry exists between any of the axes. All of this can be clearly seen in the different projections of Fig. 1.7.

The concept of a potential energy surface (PES) is crucial in understanding nuclear shape isomers. For a given nucleus, the PES often exhibits multiple minima at deformations distinct

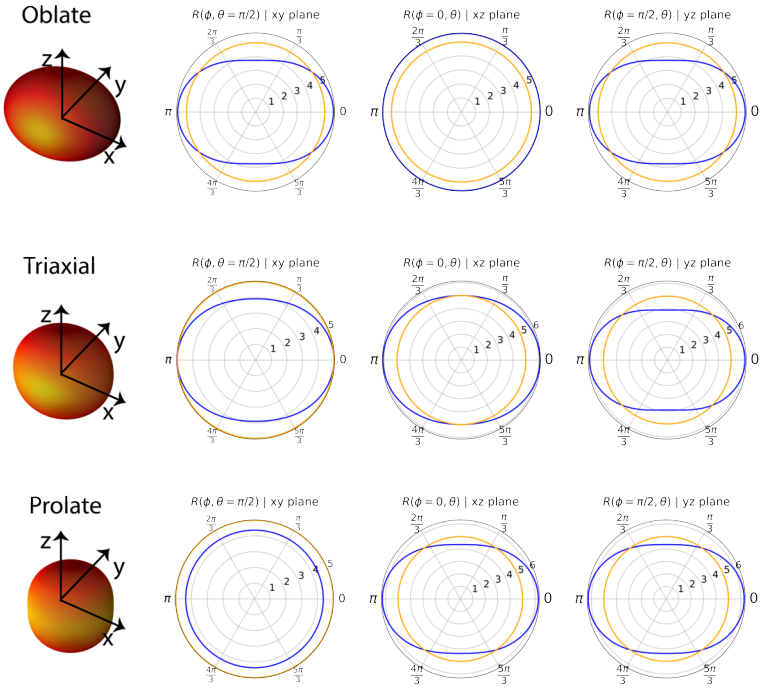

Figure 1.7. Quadrupolar deformation shapes and cross-sections along the principal axes, illustrating symmetries for a nucleus with mass number $A = 72$. For comparison, the illustration includes a spherical nucleus with 72 nucleons outlined in orange, alongside the contour of its quadrupolarly deformed shape in blue. The nuclear radius is expressed in Fermi units.

from the ground state. The ground state typically aligns with the lowest and deepest of these minima, while other minima are generally shallower. However, a sufficiently deep minimum can trap the nucleus, leading to the formation of a shape isomer. This phenomenon is observed in many 0^+ isomers. For instance, the self-conjugate nucleus ^{72}Kr has a well-documented 0^+ shape isomer [58] with a half-life of 26 ns, existing due to a hindered $E0$ transition.

Each nucleus possesses a unique PES map, indicating varying nuclear deformations based on the location of the minima. Accurately reproducing these minima, or energy traps, requires complex theoretical computations. These computations involve incorporating various nuclear interactions and are achieved through advanced simulation techniques. Notably, methodologies such as Hartree-Fock-Bogoliubov [59] (HFB) and the Symmetry-Conserving Configuration-Mixing method [60] (SCCM) are employed. These methods provide reliable simulations by considering collective wave functions and integrating multiple nuclear interactions. All of these leads to the phenomena of shape coexistence.

1.4.2 Shape coexistence

Shape coexistence [61] in nuclei refers to the occurrence of low-lying nuclear states exhibiting distinctly different intrinsic shapes, either among themselves or/and compared to the ground state. This phenomenon, widespread across the nuclear chart and believed to be present in nearly all nuclei, has been the focus of extensive experimental [62] and theoretical research [63] aimed at achieving a unified understanding of nuclear shape coexistence.

Spectroscopic evidence of nuclear deformation, and consequently of shape coexistence, can be obtained from measurements of $E2$ matrix elements via multistep Coulomb excitation (COULEX) [64] experiments, and the reduced quadrupole transition probabilities ($B(E2)$) obtained through lifetime measurements. The strengths of $E0$ transitions [65], in particular, are crucial indicators of shape coexistence. They are reflective of the degree of mixing between intrinsic configurations of different deformations. $E0$ transitions do not change the angular momentum of the nucleus but signify changes its nuclear shape or volume. These transitions are especially sensitive to the presence of different shapes at similar energy levels and provide critical insights into the interplay of nuclear configurations, thus offering a more focused perspective on the phenomenon of shape coexistence.

1.4.3 Role in nucleosynthesis

The process of forming atomic nuclei through various nuclear reactions is termed nucleosynthesis [6] (NS). This phenomenon begins with Big Bang NS, when protons, He and tiny amounts of Li (and possibly Be) were created. Subsequently, through various processes, this leads to the creation of the heaviest elements. These processes predominantly occur in stars, e.g. in supernovae [66], and other high-energy astrophysical environments, such as neutron star mergers [67]. The particular conditions of these environments, such as high neutron densities, drive phenomena like neutron capture (slow neutron capture and rapid neutron capture, s [68] and r process [69] respectively). The majority of the elements are produced via neutron induced reactions. Additionally, there are further processes, like the rp-process [70], contributing to the element abundances. In these extreme environments, atoms are often found in ionized states, as plasmas, and existing in excited states due to the high temperature and pressure conditions. This results in fully stripped excited states.

It has been observed that low-lying $0^+ \rightarrow 0^+$ transitions to the ground state can be significantly extended due to the prohibited electron conversion. This can lead to the creation, and modification, of branching points in nucleosynthesis pathways, which previously were not considered or underestimated. Isomers that play roles in nucleosynthesis are known as ASTROMERS [71, 72]. Their significance has led to their inclusion in nucleosynthesis simulation codes [73]. Examples of astromers include ^{24m}Al, ^{26m}Al, ^{93m}Mo [74], ^{99m}Tc, ^{148m}Pm, ^{176m}Lu, and ^{180m}Ta. These

isotopes have been demonstrated to significantly influence various nucleosynthesis processes [75, 76].

Chapter 2

The Nuclear Two-Photon Decay

The nuclear two-photon decay or double-gamma (2γ) involves the decay of an excited nucleus through the simultaneous emission of two photons via the virtual excitation of intermediate states. The partial half-life of this decay gives access to observables such as the (transitional) electromagnetic polarizability and susceptibility, which are important ingredients in constraining parameters of the nuclear equation of state [77], determining the neutron skin thickness [78], and constraining the nuclear matrix elements of the neutrinoless double-beta decay [40].

In §2.1, I present an insightful overview of the theory describing this decay. Section §2.2 contains a comprehensive bibliographic recompilation of past experiments exploring the nuclear two-photon decay. Lastly, §2.3 introduces a pioneering technique for investigating the two-photon decay in $0^+ \rightarrow 0^+$ transitions.

2.1 Theoretical framework

The (nuclear) two-photon[1] decay is a second-order quantum-mechanical process initially formulated for the case of atomic transitions by M. Göppert-Mayer [79, 80]. Later, it was applied to nuclear transitions by J. R. Oppenheimer and J. S. Schwinger [81], D. P. Grechukhin [82–85] and J. Eichler [86, 87], further refined by J. L. Friar and M. Rosen [88, 89] and generalized by J. Kramp *et al.* [90] by considering not only dipole transitions but also transitions with higher multipolarities.

For theoretically studying electromagnetic transitions in nuclei, we have to model the interaction between the nucleus and the electromagnetic (EM) field. This interaction can be described by the product between the vector potential created by free photons, represented by $\vec{A}$ or its operator form $A^{\mu}(x)$, and the nuclear current, $\vec{j}$ or $j_{\mu}(x)$ in operator notation, i.e. $\vec{A} \cdot \vec{j}$. At first-order

[1] Originally termed by M. Göpert-Mayer as zwei Lichtquanten or zwei Quantensprünge.

perturbation theory on $\vec{A} \cdot \vec{j}$, we obtain the (single) photon decay probability [91]. However, for describing the 2γ decay we need to extend our calculations to second-order perturbation theory. As we extend our calculations to higher orders of perturbation theory, the creation of numerous "virtual" particles and states becomes possible.

Virtual states are extremely short-lived states complying Heisenberg's uncertainty principle [92], $\Delta E \cdot \Delta t \geq \hbar$, with $\hbar$ being the reduced Planck's constant. This leads to states known as MULTI-PARTICLE or INTERMEDIATE states [93]. We can mathematically decouple the "NUCLEAR" intermediate states from "SUB-NUCLEAR" intermediate states, which involve the creation of mesons. For that, we introduce the (two-body) SEAGULL operator, denoted by $B_{\mu\nu}(x, y)$. This operator accounts for the possibility of (virtually) exciting and de-exciting high mass states that contain nucleon-antinucleon pairs. This "pair" contribution is described by an $\vec{A}^2$ term. In such a way, transitions via NUCLEAR intermediate states are captured by the first term in Eq. (2.1) treated in second-order perturbation theory. Meanwhile, transitions involving SUB-NUCLEAR states are described by the second term in Eq. (2.1) treated in first-order. The NUCLEAR intermediate states are often associated with giant dipole resonances (GDR) [89]. Interestingly, the lifetime of these resonances [94, 95] might be connected to the (partial) half-life of the nuclear two-photon decay [96].

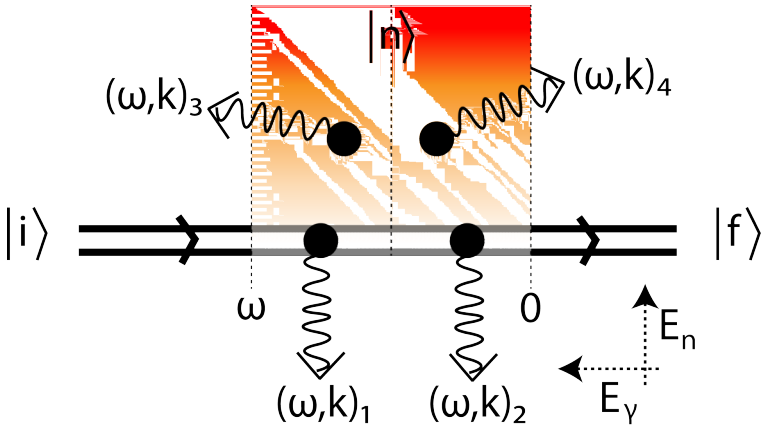

Figure 2.1. "Feynman" diagram extended by an energy dimension describing the nuclear two-photon decay.

Figure 2.1 shows a diagram trying to describe the different interaction possibilities previously described. In Fig. 2.1 the symbol $|i\rangle$ represents the initial state, while $|f\rangle$ denotes the final state after decay. Photons are characterized by their energy, ω_k[2], and momentum, k_k. A more intense color, within the intermediate state region, indicates higher energy and density of states. The sketch includes two pairs of two simultaneously emitted photons to explore the different possibilities. The diagram is created by expanding upon the traditional Feynman diagram by incorporating an extra

[2]Considering $\hbar = 1$, it follows that $E = \hbar\omega = \omega$. This allows us to refer to the radiation frequency directly as energy.

energy dimension to include the intermediate states $|n\rangle$. Given that the energy of the transition must be conserved, the sum of the photon energies must equal to it, i.e. $E_i - E_f = \omega = \omega_1 + \omega_2$. This principle is depicted in the diagram through a reflection symmetry at $\omega/2$, marked by a dashed line among the intermediate state region. Each dot signifies a point of interaction (a VERTEX). If a vertex is positioned at one extreme, symmetry implies the other is at the opposite end, indicating that one photon's energy would be zero, essentially describing a single-photon decay. Moving both vertices to $\omega/2$ can imply either a single vertex generating two photons or two vertices each emitting a photon. The former scenario is described by the SEAGULL operator, where sub-nuclear states are both created and annihilated in a single interaction, producing two photons. In this scenario, the condition $\omega_1 = \omega_2$ is not necessarily met, allowing again for a continuum of energy within ω. The later scenario is described by the first term in Eq. (2.1). Horizontally moving in the diagram explores the photon energies E_γ, while vertical movements access intermediate states of (higher) energy E_n.

Within this introduced theoretical framework, and taking into account "natural" Gaussian units[3], the interaction Hamiltonian is represented as follows [90]:

$$H_{\rm I} = \int j_\mu(x) A^\mu(x) d^3x + \frac{1}{2} \int B_{\mu\nu}(x,y) A^\mu(x) A^\nu(y) d^3x d^3y. \tag{2.1}$$

In the specific case of $0^+ \to 0^+$ transitions, accessible through our novel approach §2.3, we will encounter double transitions of identical multipolarity. This enables the investigation of the so-called diagonal transition polarizabilities, such as α_{E1E1} (equivalent to α_{2E1} or, in our notation, α_{E1}). Conversely, for other cases (defined as mixed transitions in Tab. 2.1), we will observe a mixture of multipolarities, allowing the study of the so-called off-diagonal transition polarizabilities, for example, α_{E3M1}. The different experimental cases are explored in §2.2.

Based on the interaction Hamiltonian contained in Eq. (2.1), Kramp *et al.* [90] derived the total 2γ decay probability for $0^+ \to 0^+$ ($E0$) transitions (see Eq. (A.42) in [90]):

$$W_{\gamma\gamma} = \frac{\omega_0^7}{105\pi} \left[\alpha_{E1}^2 + \chi_{M1}^2 + \omega_0^4 \frac{\alpha_{E2}^2}{4752} \right] = \frac{\omega_0^7}{105\pi} M_{\gamma\gamma}^2, \tag{2.2}$$

where ω_0 denotes the energy difference between the initial and final state, while α and χ denote the electric transition polarizability and the magnetic transition susceptibility, respectively. The sum of terms within the brackets is equivalent to the squared magnitude of the cumulative nuclear matrix element, denoted as $M_{\gamma\gamma}^2$. These observables describe the difference of the electric polarizabilities and magnetic susceptibilties between the two 0^+ states and are complementary to the standard

[3]This unit system, also known as "GOD-GIVEN", uses:

$$\hbar = c = 1 \quad ; \quad \epsilon_0 = \frac{1}{4\pi}.$$

The Gaussian system of units eliminates a factor of 4π from Coulomb's law by introducing factors of 4π into Maxwell's equations.

nuclear polarizabilities and susceptibilities, which describe the response of the nucleus to a perturbation by electromagnetic fields, and are related to changes of the nuclear charge distribution and currents inside the nucleus.

The electric transition probabilities are defined as [90]:

$$\alpha_{EL} = \frac{8\pi}{(2L+1)^2} \sum_n \frac{\left\langle 0_1^+ \middle\| i^L M(EL) \middle\| 1_n^{(-1)^L} \right\rangle \left\langle 1_n^{(-1)^L} \middle\| i^L M(EL) \middle\| 0_2^+ \right\rangle}{E\left(1_n^{(-1)^L}\right) - E\left(0_1^+\right) - \frac{1}{2}\left[E\left(0_2^+\right) - E\left(0_1^+\right)\right]}. \tag{2.3}$$

The transitional magnetic-dipole susceptibility consists of a paramagnetic and a diamagnetic term [88–90]:

$$\chi_{M1}^2 = \chi_p^2 + \chi_d^2, \tag{2.4}$$

$$\chi_p = -\frac{8\pi}{9} \sum_n \frac{\langle 0_1^+ \| M(M1) \| 1_n^+ \rangle \langle 1_n^+ \| M(M1) \| 0_2^+ \rangle}{E\left(1_n^+\right) - E\left(0_1^+\right) - \frac{1}{2}\left[E\left(0_2^+\right) - E\left(0_1^+\right)\right]}, \tag{2.5}$$

$$\chi_d = -\frac{e^2}{6m} \langle 0_1^+ \| r^2 \| 0_2^+ \rangle, \tag{2.6}$$

where the mass (m) in Eq. (2.6) corresponds to the mass of the nucleon, as it is defined by [88]. We define the nucleon mass as the average between the mass of proton, $m_p = 938.27208816(29)$ MeV [2], and neutron, $m_n = 939.56542052(54)$ MeV [2], $m = 938.91875434(31)$ MeV.

Equation (2.6) can be connected to the (dimensionless) monopole transition strength $\rho\,(E0)$ [65]:

$$\rho\,(E0) = \frac{\langle f \| M(E0) \| i \rangle}{eR^2}, \tag{2.7}$$

giving:

$$\chi_d = -\frac{e^2}{6m} \cdot R^2 \sqrt{\rho^2\,(E0)}, \tag{2.8}$$

where the nucleus radius can be approximated by $R \approx 1.2 \times \mathrm{A}^{1/3}$.

2.2 Experimental framework

All previous experiments conducted to date, of which 31 studies are available online and recompiled in Tab. 2.1, have employed γ-ray spectroscopy (§1.3.3.1) in order to investigate the two-photon decay. The main experimental challenge lies in distinguishing the relatively small signal of the two simultaneously emitted photons from other (direct or indirect) photon sources, such as single-photon decay (§1.3.3.1), internal pair creation (§1.3.3.3) or internal-conversion electrons (§1.3.3.2), due to the continuous energy spectrum associated with the two-photon emission. Therefore, ideally, the search for nuclear 2γ decays is conducted in even-even nuclei with a first excited 0^+ state, since the emission of a single γ-ray is forbidden.

In fact, among all previous studies (recompiled in Tab. 2.1), the only cases where the 2γ decay of a $0^+ \rightarrow 0^+$ transition was successfully observed using γ-ray spectroscopy are ^{16}O [97], ^{40}Ca [97], and ^{90}Zr [90]. In these cases, the excited 0^+ states are located at high excitation energies and the observed branching ratios ($\Gamma_{\gamma\gamma}/\Gamma_{\mathrm{tot}}$) for the 2γ decay are of the order of 10^{-4}. They were performed using the Heidelberg-Darmstadt CRYSTAL BALL [98–100] (similar to the one in Fig. 2.2).

Table 2.1. Previous experiments on the nuclear two-photon decay.

NUCLEUS	REFERENCE
^{16}O*	[90, 101–104]
^{40}Ca*	[97, 105–108]
^{90}Zr*	[97, 103, 105, 107, 109–116]
^{98}Mo*	[117]
^{12}Ca**	[102, 103, 118]
^{85}Rb**	[119]
^{109}Ag**	[120, 121]
^{114}In**	[122–124]
^{131}Xe**	[125, 126]
^{137}Ba**	[127–130]

* $0^+ \rightarrow 0^+$ transitions.

** Mixed transitions.

The most surprising result obtained in the successful measurements ([54, 97]) is that the angular correlation between the two photons was asymmetric about $90°$, implying that the contribution from two subsequent $M1$ ($2M1$) transitions and $2E1$ transitions are of a similar strength, while naively a dominance of the $2E1$ decay would be expected (see Weißkopf estimates in Fig. 1.4). This has been explained by a strong cancellation effect in the electric-dipole transition polarizability in these doubly-magic (^{16}O and ^{40}Ca) and semi-magic (^{90}Zr) nuclei. This cancellation effect is related to the different structure of the two 0^+ states, i.e. different contributions from $0p - 0h$ and $np - nh$ excitations across the closed shells [131].

2.3 Nuclear two-photon decay at storage rings

Low-lying 0^+ states in medium-mass even-even nuclei have typical lifetimes in the order of a few ten to hundred nanoseconds [132] because the $E0$ decay in these nuclei proceeds entirely via IC and therefore is a relatively slow process [65]. However, the 2γ decay width varies strongly with the

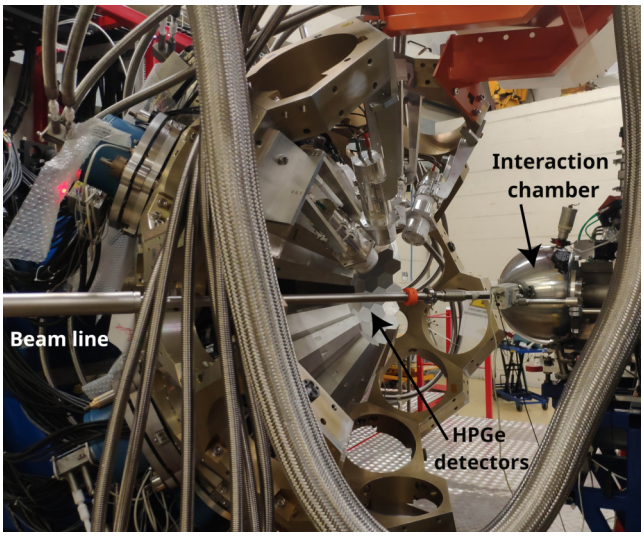

Figure 2.2. Example of CRYSTAL BALL: AGATA at the Laboratori Nazionali di Legnaro.

excitation energy, see (Eq. (2.2)), leading to extremely small branching ratios ($\Gamma_{\gamma\gamma}/\Gamma_{\text{tot}} \lesssim 10^{-6}$) for $\omega_0 < 1\,\text{MeV}$. Until now, direct searches for the 2γ emission from lower-energy 0^+ states were unsuccessful, reporting only upper limits [117]. A 2γ decay at energies below 1 MeV was exclusively observed from the $11/2^-$ isomer in ^{137}Ba using the fast-timing method [129, 130], reporting a branching ratio of $\Gamma_{\gamma\gamma}/\Gamma_{\text{tot}} \sim 2 \times 10^{-6}$ [129]. Here, the single-photon decay is strongly hindered due to its highly unfavorable multipolarity ($M4/E5$). Alternatively, if all bound electrons are removed the IC is disabled [133] and therefore 0^+ states can only decay by 2γ emission to the ground state or by particle emission (α- or β-decay) in unstable nuclides. This is sketched in Fig. 2.3. In this thesis we report the first direct measurement of the 2γ decay of the first

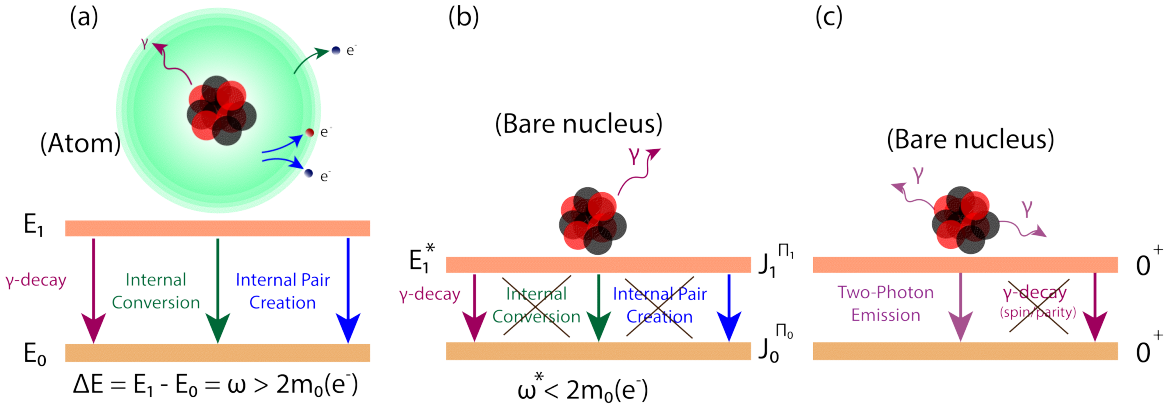

Figure 2.3. Nuclear electromagnetic decays of an atom (a), and the isolation in low-lying isomers (b) of the $0^+ \to 0^+$ 2γ decay (c) in bare nucleus (b,c).

excited 0^+ state in stored, fully-ionized $^{72}Ge^{32+}$ nuclei. This isomer, with an excitation energy of 691.43 (4) keV [134], possesses a half-life of 444.2 (8) ns [135] in neutral atoms. However, when it is fully ionised, the partial half-life for this isolated decay can be estimated to extend to

several hundred milliseconds, hence giving an expected branching ratio of $\Gamma_{\gamma\gamma}/\Gamma_{\text{tot}} \sim 2 \times 10^{-6}$. Figure 2.4 contains this estimation.

The solid line in Fig. 2.4 corresponds to the curve obtained by considering the ratio $W_{\gamma\gamma}$ and ω_0^7 constant, with the constant being the average value of the sum of squares of the previously determined [90, 97] $M_{\gamma\gamma}$ nuclear matrix elements in Eq. (2.2). The vertical red dotted line in Fig. 2.4 is placed at the excitation energy of the isomeric state of ^{72}Ge.

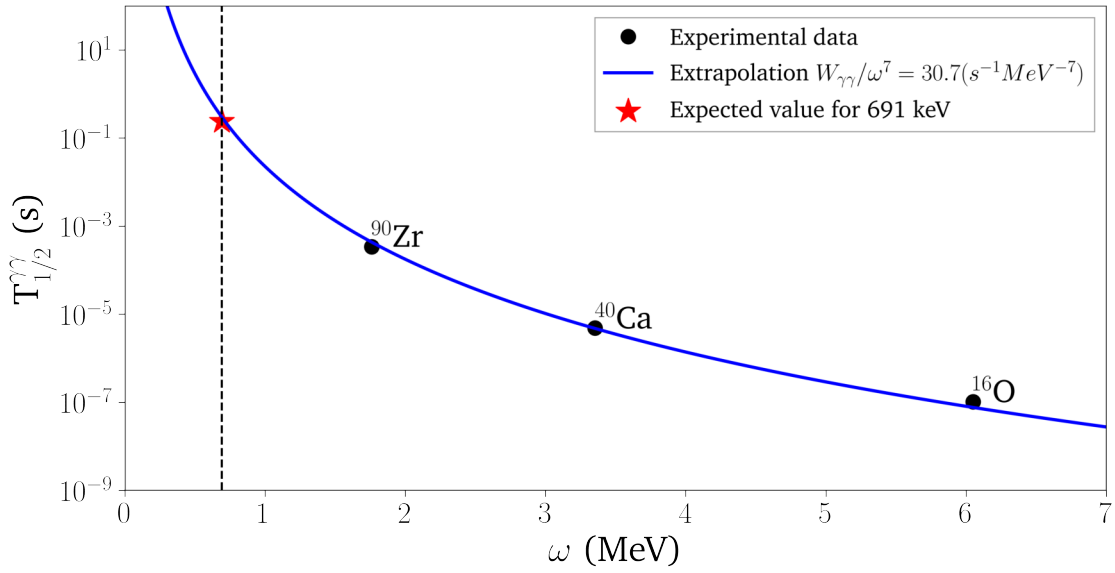

Figure 2.4. Measured nuclear two-photon decay (partial) half-lives, taken from [90, 97], as a function of their excitation energy. The (red) star indicates the predicted half-life for the first excited state of ^{72}Ge, derived from the extrapolation shown by the blue line, which has not been measured previously.

By combining the isochronous mode (§3.2) of a storage ring (§3.1.2) with non-destructive single-ion-sensitive resonant Schottky detectors (§3.1.3), the new experimental technique termed combined Schottky plus Isochronous Mass Spectrometry (S+IMS) (Chap. 3), we were able to produce, store and resolve the isomeric state (§1.4) of fully-stripped ions and measure the time evolution of the number of observed isomers with a resolution of the order of milliseconds (Chap. 4). The thereby developed method is a sensitive approach to search for unknown excited 0^+ states in exotic nuclei and for the measurement of their 2γ-decay half-lives. The foundations of this novel methodology are addressed in Chap. 3.

Chapter 3

Combined Schottky + Isochronous Mass Spectrometry (S+IMS)

Herein, I present the foundations of a novel methodology for investigating the nuclear two-photon decay at storage rings and other high-precision mass and half-life measurements by combining the isochronous mode of a storage ring with non-destructive resonant Schottky cavities hence S+IMS. Specially, we focus on the Experimental Storage Ring (ESR) at the heavy-ion research facility GSI. The techniques and approaches described herein are crucial for the advancement of storage ring mass spectrometry.

An overview of the experimental setup employed is presented in §3.1, which is subdivided into production (§3.1.1), storage (§3.1.2), and detection (§3.1.3). Section §3.2 discusses the isochronous mode of the ring, detailing how it can be quantified and monitored in real time (in-line) using the electron cooler, as discussed in §3.2.1, and through off-line analysis, as outlined in §3.2.2. In §3.3, we detail the steps followed during the data analysis, encompassing data classification (§3.3.1), Schottky-based ion identification (§3.3.2), mass determination (§3.3.3), and half-life determination (§3.3.4).

3.1 Experimental setup

The Gesellschaft für Schwerionenforschung [136] (GSI) facility is a forefront center for research in atomic and nuclear physics located in Darmstadt, Germany. It specializes in the production and acceleration of heavy ions for various scientific experiments, from fundamental physics research [137] to applications in material science [138] and medicine [139]. Here took place the realization of experiment E143 [140], where the isolated nuclear two-photon decay was measured for the first time. Therefore, the whole setup and its functions during the different stages: production (§3.1.1), storage (§3.1.2), and detection (§3.1.3), will be elucidated.

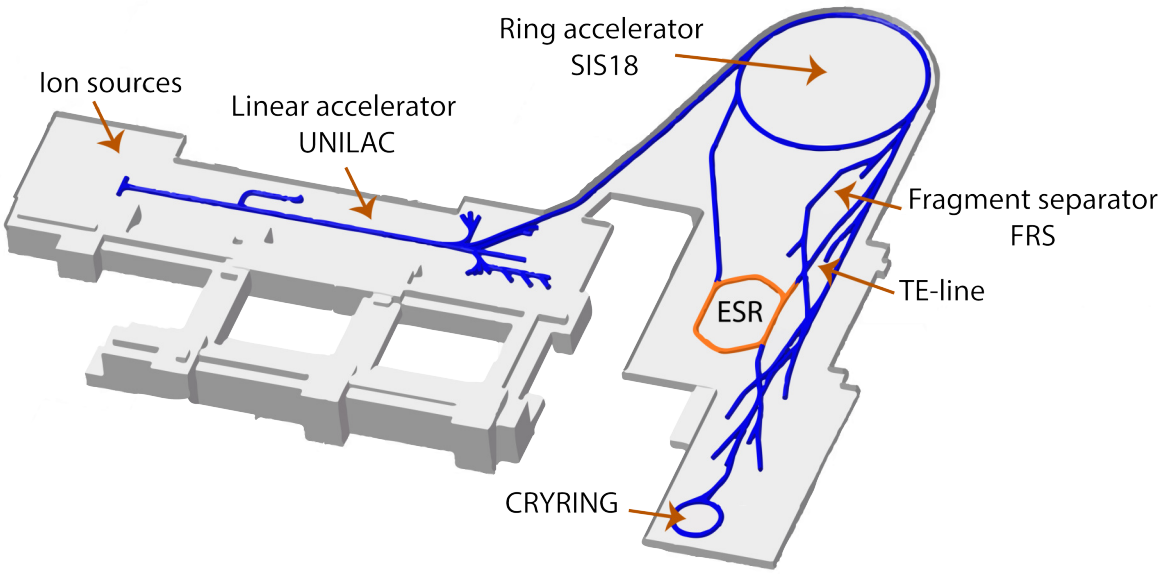

Figure 3.1. GSI accelerator facility. Details of the facility will be discussed in the text. Based on [141].

Figure 3.1 shows a scheme of the accelerator facility at GSI. This facility has the capability to produce and accelerate highly-charged ions from hydrogen up to uranium (see §3.1.1). The ion source is the starting point for the production of positively charged ions (§3.1.1.1). The produced lowly-charged ions (of a single species) are then accelerated in different stages by linear and circular accelerators (§3.1.1.2). When the ions have reached relativistic energies, they are impinged on solid Be targets of a determined thickness in order to produce the desired fragments via projectile fragmentation (§3.1.1.3). Depending on the needs, independent nuclei species can be separated (purified) by the FRagment Separator [142] (FRS) or all the fragments can be directly inserted into the experimental storage ring (ESR) through the TE-LINE. Once stored within the ESR (§3.1.2), we can perform a variety of experiments with the different elements and detectors (§3.1.3). If needed, the produced fragments can be decelerated and transferred to a lower-energy ring, the CRYRING [143, 144], or to the ion-trap facility HITRAP [145].

3.1.1 Production

3.1.1.1 Initial stages

The initial stage of ion production involves the creation of high-current ion beams. Two primary mechanisms facilitate ion generation: photoionization [146], where ions are produced through photon collisions, and impact ionization [147], resulting from electron collisions. Depending on the mechanism and materials involved, there are several types of ion sources [148]:

- **Filament driven ion sources:** These include the Multi Cusp Ion Source (MUCIS) and its advanced versions, as well as CHORDIS (Cold or Hot Reflex Discharge Ion Source),

which are essential for creating dense plasma environments to facilitate ion production. Notably, MUCIS has been extensively studied and applied in various applications, including cyclotrons, due to its ability to confine ions effectively within cusp geometries of magnetic fields, thus enhancing beam currents.

- **Vacuum arc driven ion sources:** Including the Metal Vapor Vacuum Arc Ion Source (MEVVA) and VARIS (Vacuum Arc Ions Source). They employ metal vapors to generate ion beams. These sources make use of a vacuum arc mechanism to ionize metal vapors, which is crucial for applications requiring heavy metal ions.

- **High duty factor sources:** Such as the PIG (Penning Ionization Gauge).

- **Electron cyclotron resonance (ECR) sources:** ECRIS (Electron Cyclotron Resonance Ion Source), uses microwave technology to ionize gases in a magnetic field. This was the one employed for producing initially the ions of ^{78}Kr.

3.1.1.2 Acceleration

The acceleration of ions is a critical step in preparing them for experiments. At GSI we have a combination of linear and circular accelerators. While linear accelerators are dominated by radiofrequency cavities, the circular ones primarily utilize magnets [149].

As the first acceleration stage, the GSI facility uses the UNILAC (UNIversal Linear ACcelerator), which is composed of three parts:

- **UNILAC Wideroe accelerator:** Operates at a frequency of 27 MHz, accelerating ions from zero to $2 \cdot 10^6$ km/h. For that it employs a voltage range of 20 kV to 130 kV. Within it, the ions reach speeds of $\beta \approx 0.2\,\%$.

- **Connection line to the Alvarez accelerator:** Composed of several single-cavity resonators and a gas-stripper for enhancing the acceleration efficiency, reaching $\beta \approx 6\,\%$.

- **UNILAC Alvarez accelerator:** Following the Wideroe accelerator, this accelerator operates at a higher frequency of 108 MHz. It uses a standing wave to accelerate ions to $\beta \approx 16\,\%$, or equivalently to energies of 11.4 MeV/u.

Once ions have received this initial acceleration, they are transferred to the synchrotron SIS-18 through a process involving a foil stripper and charge state separation.

The GSI synchrotron SIS-18, known as SchwerIonenSynchrotron, is a key component of the GSI facility, designed for the acceleration of a wide range of ions, from protons (4 GeV, $\beta \approx 98\%$) to highly-charged uranium ions (1 GeV/u, $\beta \approx 88\%$). This can be achieved due to its characteristics; it has a circumference of 216 m, a bending radius of 10 m and a maximum

magnetic field strength of 18 T, along with RF cavities working from 0.85 MHz to 6 MHz, and an ultra-high vacuum of 10^{-11} mbar.

3.1.1.3 Projectile fragmentation

At relativistic velocities, nuclear collisions are extremely violent, and a vast range of fragments can be created [150]. The reaction is not selective in terms of its products, but the forward momentum of each fragment allows for precise identification using time-of-flight and energy-loss techniques to determine their mass and charge. The efficiency of fragment production is constrained by the thickness of the target, which is chosen to minimize energy and angular straggling at maximum fragment production. Once created, the fragments can be filtered via the FRagment Separator or can be injected directly into the ESR through a direct beam line, the TE-LINE.

The FRagment Separator[1] [142] (FRS) is configured by a set of two dipoles, a degrader, and two more dipoles designed for implementing the $B\rho - \Delta E - B\rho$ separation technique. Time-of-flight (ToF) measurements are employed between the $\Delta E - B\rho$ section for particle identification, complemented by the use of time projection chamber (TPC) detectors for spatial positioning measurements, and plastic scintillators for ToF. This method enables the filtration of fragments, allowing for the selection of specific species, as demonstrated in [18].

The TE-LINE serves as the direct transfer line between the SIS-18 and the ESR, facilitating the transfer of all produced fragments into the ESR, which operates as a mass spectrometer. Utilizing slits, as described in §3.1.1.4, enables the exclusion of undesired ions (contaminants). Due to the high demand for FRS usage, experiments that can be executed through the TE-LINE receive priority in beam time scheduling, as was the case with the E143 experiment [140]. Additionally, the direct line enables faster extraction compared to the FRS, with a time of approximately 500 μs.

Via using LISE++ [151], we are able to simulate both the reaction leading to the creation of fragments and their subsequent transmission to the storage ring. It enables the prediction of fragment production rates, ion optical settings for optimal fragment selection, and the efficiency of transmission through simulated beam lines to the storage ring. Thus, the fragments predicted by LISE++ serve as a first (realistic) estimate for what we should encounter in the ring during identification (more in §3.3.2.1).

3.1.1.4 $B\rho$-CUT

By using the TE-LINE, the only way to filtrate the fragments is by utilizing mechanical slits. With them, we are able to select a specific $B\rho$ range (window). By placing these slits at different planes and positions, it is possible to manually exclude particles on certain orbits without affecting the

[1] Please note that the FRS was not used in this experiment; however, it is included here to provide a complete overview for the thesis.

selected $B\rho$ range, hence performing a $B\rho$-CUT. This approach somewhat reduces the number of contaminants and narrows the allowed momentum spread to a more uniform area, particularly regarding γ_t. The relative momentum spread before entering the ESR exceeds 1 %, but after the $B\rho$-cut, it can be reduced to approximately 0.01 %.

As a result of this selection process, the distribution of particles in terms of their $B\rho$ values becomes non-symmetric (as depicted in Fig. 3.2), being one of the reasons to the observed deformation in the peak shape. This produces the selection of more particles at either higher or lower $B\rho$ values compared to the mean

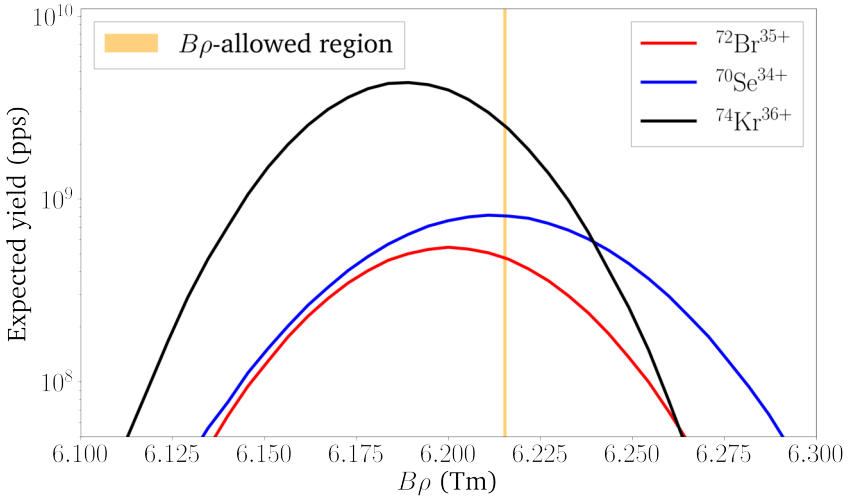

Figure 3.2. Illustration of the $B\rho$-CUT over some expected yields of fragments by LISE++.

3.1.2 Storage

The ions are transferred to and confined into the experimental storage ring [24]. Since recently GSI counts with another storage ring with smaller dimensions [143, 144], designed for lower energies. This experiment utilized only the ESR, in which we will focus on in greater detail. Storage rings share the same principles as circular accelerators but tailored for specific research applications, as was introduced already in §1.2.1. Like in circular accelerator, its capabilities are defined mostly by their geometry and dipole magnet strength, i.e. they are governed by Eq. (1.5).

As shown in Fig. 3.3, the ESR has a circumference of 108 meters (half of the SIS-18) and is composed of six 60° dipole magnets, with a maximum magnetic rigidity of up to 10 Tm. This allows the storage ring to operate over a broad energy range from 4 MeV/u to 420 MeV/u, therefore the revolution frequency of the ions revolving the storage ring ranges approximately between 0.6 MHz to 2 MHz. In addition, it maintains an ultra-high vacuum of 2×10^{-11} mbar to significantly reduce interactions with residual gases, and multiple mechanism for cooling (see §1.2.2). All of this enables high-precision studies on masses, half-lives and nuclear reactions for atomic, nuclear

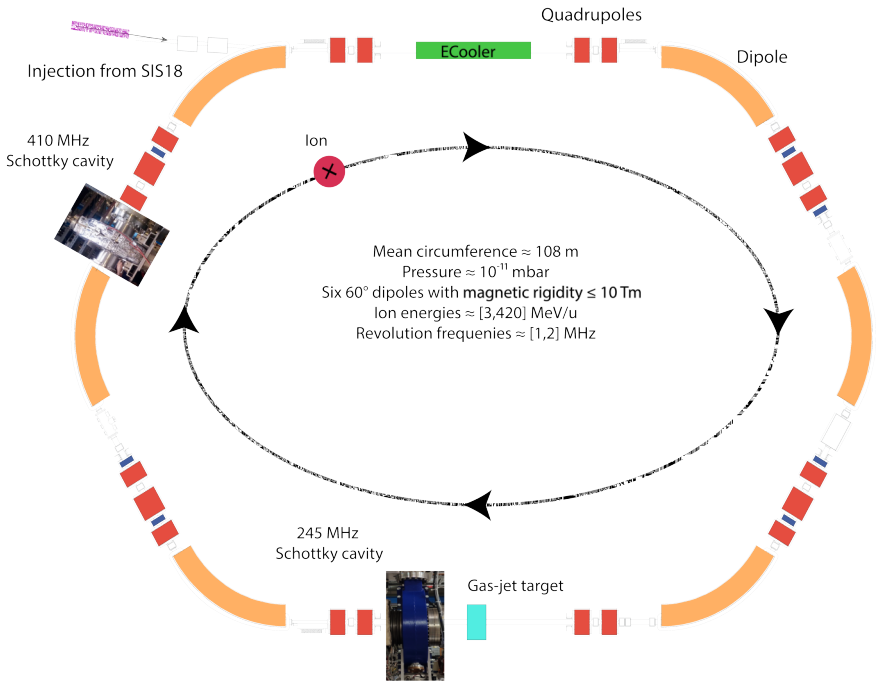

Figure 3.3. The experimental storage ring (ESR) and its main characteristics. For details see text.

and astrophysics motivations. In Fig. 3.3 are shown the locations of the detectors used during the E143, the 245 MHz [152] and 410 MHz [153] resonant Schottky cavities. More details are given in §3.1.3.

3.1.3 Detection

3.1.3.1 Schottky cavity resonators

Charged particles traversing a beam pipe drag an opposite equivalent charge on its inner surface. In the surfaces of isolated sections, such as detector plates, this surface charge oscillates and dissipates [154], measurable as an induced current $i(t)$[2]. A **similar** charge redistribution occurs on cavity walls, differing mainly in duration. This results in an oscillating electric dipole and an alternating magnetic field, with energy oscillations between both fields continuing after the particle passes through, as illustrated in Fig. 3.5. This oscillation is measured by extracting field energy with an electric pin or magnetic loop [152, 153, 155].

For multiple particles, the induced current $i(t)$ becomes a stochastic process due to the random phase offsets[3] between particles. The expected value of this process equates to the macroscopic direct current (DC) beam current I_B, formulated as $\langle E[i(t)]\rangle = Qef_rN = I_B$ [155], where

[2]It is important to note that the induced current itself is not directly measured. Instead, the voltage drop resulting from this current's interaction with the detector's impedance is recorded, which generally is frequency dependent.

[3]Not all the particles reach the detectors at the same time, they are randomly distributed.

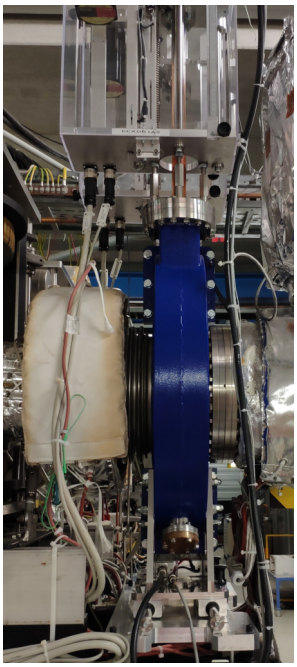

(a) The 245 MHz resonant Schottky cavity.

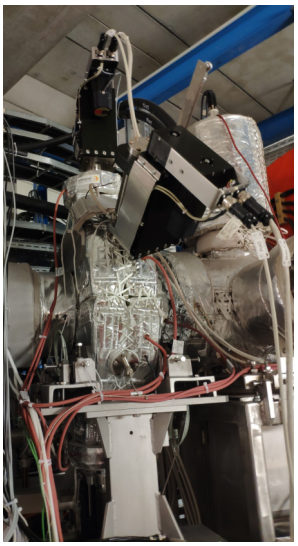

(b) The 410 MHz resonant Schottky cavity.

Figure 3.4. Pictures of the Schottky cavities present at the ESR.

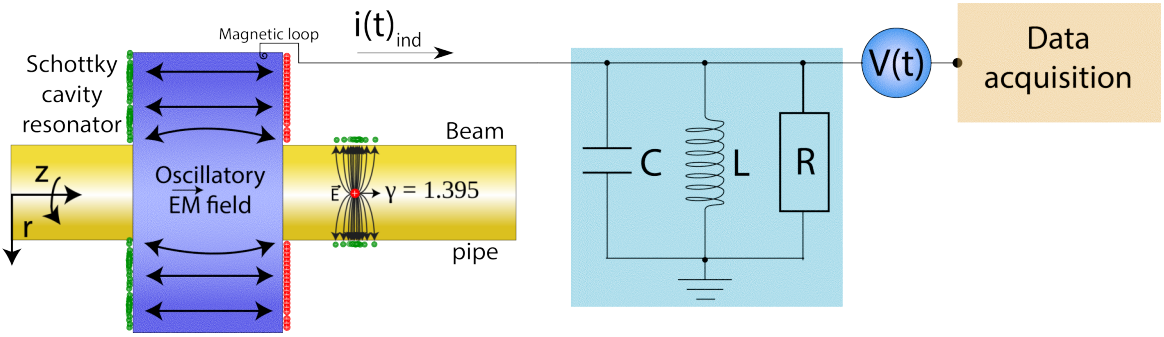

Figure 3.5. General sketch of a resonant Schottky cavity.

N represents the number of particles, e the elementary charge, Q the charge state, and f_r the revolution EIGENFREQUENCY. Spectral analysis reveals peaks at integer multiples, HARMONICS (h), of the EIGENFREQUENCY, known as SCHOTTKY BANDS. These bands present a decrease in peak amplitude and an increase in width with higher harmonics (as can be seen in Fig. B.1), suggesting a **constant** integral power across all bands [154]. The total noise power is given by [156]:

$$\langle I \rangle^2 = 2N \left(Q e f_r\right)^2 . \tag{3.1}$$

These non-destructive cavity detectors exhibit impedance spectra with pronounced peaks at their EIGENFREQUENCIES. This characteristic is exploited to enhance detection sensitivity and resolution at higher frequencies, albeit at the expense of operating within a narrow bandwidth. In contrast, parallel plate detectors tend to display a simpler impedance spectrum, potentially offering

a broader operational frequency range but with different sensitivity and resolution profiles [155]. For having the best of both worlds, at the ESR we have two Schottky cavities and a parallel plate Schottky. Among the Schottky cavities, one works at 245 MHz of resonant frequency and the other has an operational resonance frequency at 410 MHz. In comparison to the 410 MHz detector, the 245 MHz cavity has a smaller quality factor, which translates into a poorer signal-to-noise ratio (S/N). Although both detectors are single-ion sensitive, the difference in S/N means that the 245 MHz detector requires a longer detection time.

Can there be a resonant Schottky cavity (RSC) everywhere?

Apart from non-physical reasons, the answer is no. RSCs have a high quality factor, or in other words, a high impedance which is coupled to the rest of the circuits. Due to its high impedance, it can lead to destructive effects [153] on the beam for cases in which the intensity is high (in terms of number of particles) or really high velocities. Around 1 GeV/nucleon these effects could be observed.

3.1.3.2 Data acquisition

During the experiment, resonant Schottky cavities were employed for beam diagnostics and for measuring the revolution spectra. To this end, each Schottky was connected to a real-time spectrum analyzer (RSA) of TEKTRONIX®. These analyzers were centered in time around the injections and recorded 5 seconds of data before and after this time. In addition, the 245 MHz Schottky was connected to a continuous time and broadband recording device, the NTCAP [157, 158].

The RSAs are specially useful for the fast in-line monitoring of specific isotopes and their half-lives. However, for performing mass measurements and optimizing the setting we need a broader picture. This can be facilitated by the NTCAP system, which also enabled the concurrent recording of scalar signals, including kicker time, cooler voltage, cooler current, gas target pressure, SIS kicker signal, ESR DCCT current, gas target status, and the raw kicker signal. Moreover, the NTCAP provides a higher time resolution of 50 ns compared to the $\sim$ 20 μs offered by the RSAs. This allows more accurate determination of injection times, as is discussed in §3.3.1.3.

3.2 Isochronous mode

In this section, I address how the isochronous mode condition can be measured in-line (§3.2.1) and off-line (§3.2.2).

3.2.1 Electron cooler curve

As previously discussed in §1.2.1.2, the isochronous mode occurs when $\gamma \to \gamma_t$. This signifies that ions of the same species become isochronous with each other, reaching the detector at the same frequency (ISOCHRONOUSLY) regardless of their velocities. This peculiar feature can be found by performing an energy scan to identify an energy region where, despite increasing the ion's energy, their revolution frequency remains unchanged.

In storage rings, such an energy scan is feasible through electron cooling, as introduced in §1.2.2.1. Figure 3.6 illustrates this scanning process, measured in 2014[4] by Schottky cavity detectors, in both 2D (Fig. 3.6a) and 1D (Fig. 3.6b) spectra. In Fig. 3.6a each frequency shift[5] over time indicates a change in the electron cooler's voltage[6], hence in its energy, which progressively increases. This leads to a decrease in revolution frequency until reaching a specific region where further energy increments do not affect the frequency. This zone is identified as the ISOCHRONOUS WINDOW. "Surprisingly", beyond this point, as energy continues to rise, the frequency increases. This phenomenon occurs because, similar to earlier when energy augmentation led to increased velocity and consequently lower revolution frequency, post-transition, the increment in path length predominates over the velocity gain. Eventually, this results in orbits becoming unsustainable within the ring's acceptance, causing collisions with the ring walls hence losing the ions. Therefore, with this procedure we can obtain the ion-optical parameter γ_t.

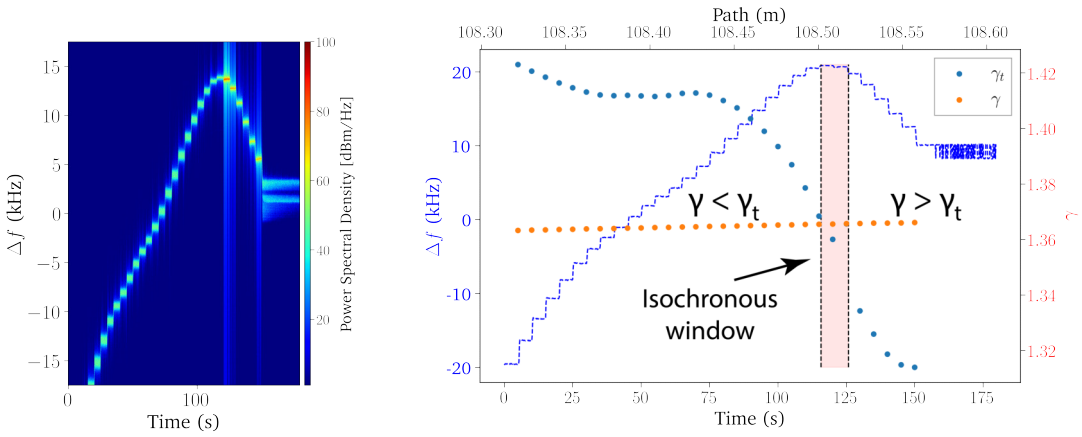

(a) Electron cooler curve spectrogram.

(b) Electron cooler curve spectrum.

Figure 3.6. Electron cooler curve. Every 5 seconds the primary beam's energy is increased by 50 eV through the electron cooler.

Despite being determined solely with one species (the primary beam), the parameter is in-

[4]Unfortunately, during experiment E143, no 2D spectrogram was recorded from the electron cooler curve. Since 2D spectrograms clearly demonstrate the followed procedure, I have analyzed older data for explanatory purposes.

[5]Every 5 seconds.

[6]Corresponding to 50 eV per step.

dependent of the ions, representing an intrinsic property of the ring. Consequently, this parameter remains constant provided the magnet configuration is not changed. The width of the ISOCHRONOUS WINDOW can be tuned using sextupole and octupole magnets. Ideally, within the ESR acceptance, the revolution frequency should be the same for all the allowed energies, resulting in peak spreads following a Dirac's delta. This scenario is theoretically possible as each ion would follow a unique path, hence eliminating the possibility of Coulomb or other interactions between the ions. Thus, IMS has the potential to achieve superior mass resolution compared to SMS. Nonetheless, the situation is not entirely straightforward; crossing the transition point [30] can induce resonances in the beam (as observed in Fig. 3.6a), complicating the analysis. This phenomenon needs more investigation.

Is Cooled Isochronous Mass Spectrometry (CIMS) feasible?

When we cool the ions by any means, all of them share the same velocity after a certain time. Due to this, as already described in §1.2.2, it can occur intra-beam scattering due to the Coulomb repulsion between ions of the same species. Therefore, this sets a limit on how reduced the momentum spread can be to where the Coulomb repulsion and the cooling force are in equilibrium. However, in IMS the ions do not share the same orbit, so in principle this limit is removed and, theoretically speaking, the IMS could have more potential for mass spectrometry. Now, if we try to cool the IMS, by definition we are forcing the ions to follow some specific orbit, hence destroying the working principles of IMS. A different (and worth testing) approach would be:

1. Inject the fragments into the ESR.
2. Cool them.
3. Turn off the cooling.
4. Adjust γ_t (if necessary).

   Incorporating cooling limits the half-life of the studied nuclides to $\gtrsim 1$ s.

3.2.2 Peak spread curve

Ultimately, the ISOCHRONICITY is also manifested in the measurable time (frequency) spread of peaks, denoted as σ_t. In such a way, through offline analysis is possible to deduce the transition energy parameter (γ_t) among other beam parameters, such as the relative momentum spread (σ_p/p)

and the systematic errors (σ_{sys}), as contained in the equation (refer to App. A for its derivation):

$$\sigma_T = \sqrt{\left(\left(1 - \left(\frac{L}{T \cdot c}\right)^2 - \frac{1}{\gamma_t^2}\right) \cdot \left(\frac{\sigma_p}{p}\right) \cdot T\right)^2 + \sigma_{sys}^2}, \tag{3.2}$$

where L represents the particle path length, and c is the speed of light in vacuum. By applying a fitting procedure, we can estimate the average values of these parameters.

The impact of varying the parameters in Eq. (3.2) offers valuable insights into the behavior and implications of the resulting curves. Examining the effects of adjusting one parameter while fixing the others constant reveals:

- Modifying the ring's transition energy shifts the isochronicity curve to different m/q regions. The effect would be similar to modifying the Lorentz factors (γ) of isotopes while keeping γ_t fixed, as the curve's minimum corresponds to a specific energy/revolution time in the ring. Adjusting the settings of the storage ring can result in unpredictable behavior of the beams stored in the ESR. Therefore, modifying the gamma values presents a more practical and manageable approach, since the ion-optical setting will remain fixed and well-characterized. Furthermore, when employing Schottky resonant cavities, there is no need to alter neither their resonant frequency once fixed in the frequency corresponding to γ_t. Although, adjustments to the resonant frequency can be made by slightly modifying the cavity dimensions.

- Altering the particles' relative momentum spread can enhance the overall mass resolving power by flattening the ISOCHRONICITY CURVE, albeit without improving the peak resolution within the isochronicity window, this is the minima will not be lower as can be seen in Fig. 3.7b.

- The maximum[7] achievable resolving power is constrained by unidentified sources of uncertainty. It comes from second order terms in Eq. (1.4) mainly related to the magnet settings.

3.3 Data manipulation

In this section, I outline the process for selecting high-resolution data from a total dataset of 46 TB (§3.3.1), and how it was processed for performing mass (§3.3.3) and half-life (§3.3.4) measurements.

[7] How far from 0 is the minimum peak width.

How does changing the Lorentz factor affect the isochronicity curve?

Since this term solely depends on the longitudinal velocity of the ions, producing ions with slightly higher (lower) velocities results in a shift of the entire frequency pattern towards lower (higher) frequencies. Consequently, its effect might be camouflaged as a (broader) standard deviation, especially when considering the overlay of different injections under the same magnetic settings. The velocity of the generated fragments is primarily influenced by the energy obtained by the primary beam during the acceleration stage, which can vary slightly from one injection to another. Hence, frequency correction (refer to §3.3.1.4) is essential for removing this additional uncertainty and improving the measurement accuracies.

3.3.1 Data classification

Here, I describe how the high-resolution data was recorded (§3.3.1.1), selected (§3.3.1.2) and pre-processed (see §3.3.1.3 and §3.3.1.4).

3.3.1.1 Recorded data

The process of converting ion-induced periodic signals into a measurable form involves transforming these signals into voltage drops across a circuit, captured within a finite temporal resolution. Therefore, since the moment we record the data we are losing information. Subsequent stages involve the refinement and simplification of this physical information through various amplification and mixing circuits, culminating in the digital storage of data in binary format. To facilitate data access and manipulation of Schottky-based data, the IQTOOLS [159] PYTHON library was developed.

3.3.1.2 Exploratory data analysis

The initial phase of data analysis focuses on differentiating between usable and non-usable data. With the help of the experimental electronic log, which can be found in [160], we can check when there was a stable[8] beam or not, and verify them through preliminary analysis. In this way, we can constrain significantly the data to analyze. Subsequently, we explore "macroscopic" features, such as the signal-to-noise ratio, total power across the bandwidth and count, location, and shape of peaks. Data injections sharing similar characteristics are then classified into the same subset. Within these data subsets, the injection times are identified, and optimal FFT parameters for our analysis needs are determined.

[8] Without any operational issues.

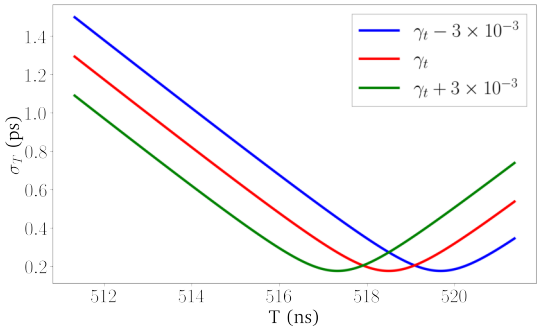

(a) Variations of the transition energy (γ_t).

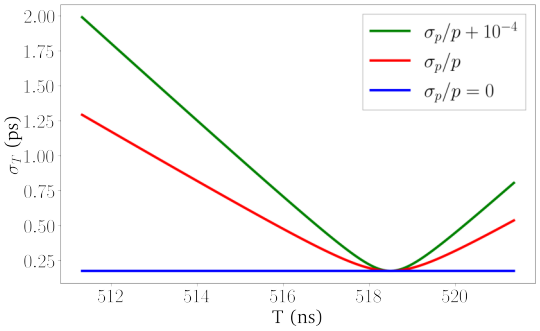

(b) Variations of the relative momentum spread (σ_p/p).

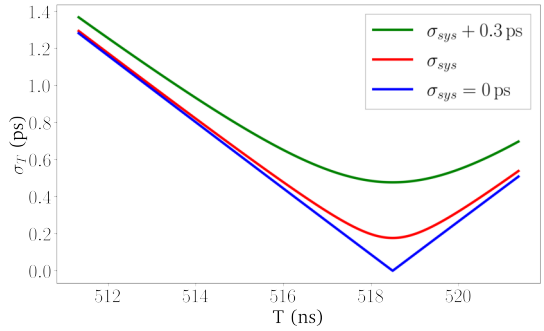

(c) Variations of the systematic uncertainties (σ_{sys}).

Figure 3.7. Change of behaviors of the isochronicity curve by considering each parameter in Eq. (3.2) independent.

3.3.1.3 Determination of the injection time

While injection times are clearly marked in RSA data, this is not the case for NTCAP data. Given the voluminous data, locating them is challenging. To accurately identify injection times in the continuous NTCAP data, I searched for features of injection, such as frequency shifts and power fluctuations over time, utilizing the latter for its robustness and superior time resolution, which utilizes the data's maximum temporal resolution ($\sim$ nanoseconds for the NTCAP data, see §3.1.3.2). For this purpose, I developed the software TDMCHOPS [161].

This technique has been named the V-METHOD, reflecting the shape of the moving average as depicted in Fig. 3.8b. It is based on the empirical observation that approximately 30 ms before a new injection, the preceding signal within the ESR almost completely disappears (see Fig. 3.8a), indicated by a sudden decrease in total recorded power, and therefore in the number of ions stored. To precisely identify the moment of injection, we apply a moving average over a span of 30 ms, where the minimum reveals the exact injection time, resulting in a distinctive V-SHAPE.

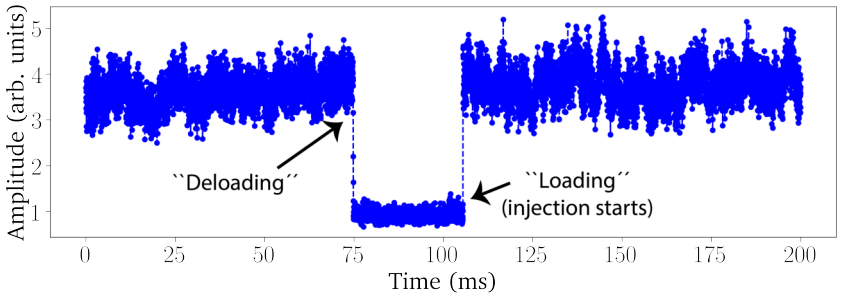

(a) Power fluctuations around injections.

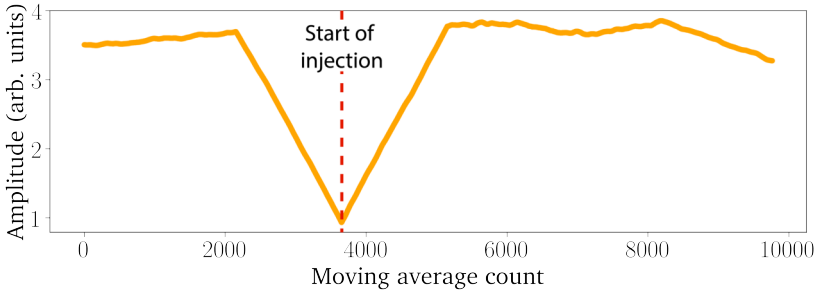

(b) Moving average of 30 ms.

Figure 3.8. Power fluctuations around injections serve as a reliable indicator for determining injection times with the highest precision given by the sampling time.

The underlying reasons for this intensity fluctuations are not fully understood and require of further investigations. It is believed that residual magnetic fields in the kicker magnet could lead to this characteristic phenomenon.

3.3.1.4 Frequency correction and add-up

After defining our data subsets, processing them through FFT, and finding the injection time, we aggregate all spectra together. This approach allows us to retain the entirety of the physical information while significantly reducing the data volume for subsequent analysis, from $\sim$ Terabytes to $\sim$ Gigabytes.

Firstly, we add all the spectra without taking any reference peak. This is termed BLIND SUM. Next, we select one of the peaks with the highest yield[9], and we use it as a reference peak to center individually each spectrogram to the same reference frequency. This step, although altering the frequency information, corrects for magnetic instabilities (via SOFTWARE COOLING) and for fluctuations in γ values across different injections as well as within single injections, hence enhancing data quality while maintaining all the information.

[9]Since it will be present (ideally) in all the injections, so the reference will not change.

3.3.2 Schottky-based ion identification

After pre-processing, we can proceed with the identification of **every** peak and the determination of its characteristic: location, spread and shape. For this, we rely on the developed python library RionID [162] (Ringed ion IDentification) and Gaussian fitting.

3.3.2.1 RionID

The RionID [162] software plays a key role in peak identification, based on overlaying simulated (ideal) ion revolution frequencies onto the experimental data. Deviations between the simulated and real data are observed, as expected due to the influence of the velocity spread term in Eq. (1.4). These deviations typically follow a parabolic behavior as have been empirically observed. Therefore, they can be corrected, extending the correctness of the simulation to the whole measured frequency range.

To emphasize that in Eq. (1.4) we are relating the "distances" of various parameters relative to a reference particle, we introduce the subscript $_i$ for each ion, and $_r$ for the reference ion, resulting in:

$$\frac{\Delta f_i}{f_r} = -\frac{1}{\gamma_t^2}\frac{\Delta\left(\frac{m}{q}\right)_i}{\left(\frac{m}{q}\right)_r} + \left(1 - \frac{\gamma_i^2}{\gamma_t^2}\right)\frac{(\Delta v)_i}{v_r}. \tag{3.3}$$

To simplify our simulation of expected revolution frequencies, we adopt a first-order **approximation** by neglecting the second term in Eq. (3.3). Therefore, the resulting formula for the simulated revolution frequency of an ion i is:

$$f_i^{\mathrm{s}} = f_r \cdot \left(1 - \frac{1}{\gamma_t^2}\frac{\Delta\left(\frac{m}{q}\right)_i}{\left(\frac{m}{q}\right)_r}\right), \tag{3.4}$$

where we assume the same γ_t for every ion.

As expected, empirically we observe that the simulated f_i^{s} do not match the experimentally measured frequencies for many ions (specially the ones outside the isochronous window). Investigating the difference between experimental and simulated (superscripts $^{\mathrm{e}}$ and $^{\mathrm{s}}$, respectively) revolution frequencies f_i^{e} - f_i^{s} reveals a parabolic dependence with frequency (as can be seen in Fig. 3.9), expressed as:

$$f_i^{\mathrm{e}} - f_i^{\mathrm{s}} = a + b \cdot f_i^{\mathrm{s}} + c \cdot \left(f_i^{\mathrm{s}}\right)^2. \tag{3.5}$$

This implies:

$$f_r \cdot \left(1 - \frac{\gamma_i^2}{\gamma_t^2}\right)\frac{(\Delta v)_i}{v_r} = a + b \cdot f_i^{\mathrm{s}} + c \cdot \left(f_i^{\mathrm{s}}\right)^2, \tag{3.6}$$

because, by definition (combining Eq. (1.4) and Eq. (3.4)):

$$f_i^{\mathrm{e}} = f_i^{\mathrm{s}} + f_r \cdot \left(1 - \frac{\gamma_i^2}{\gamma_t^2}\right)\frac{(\Delta v)_i}{v_r}. \tag{3.7}$$

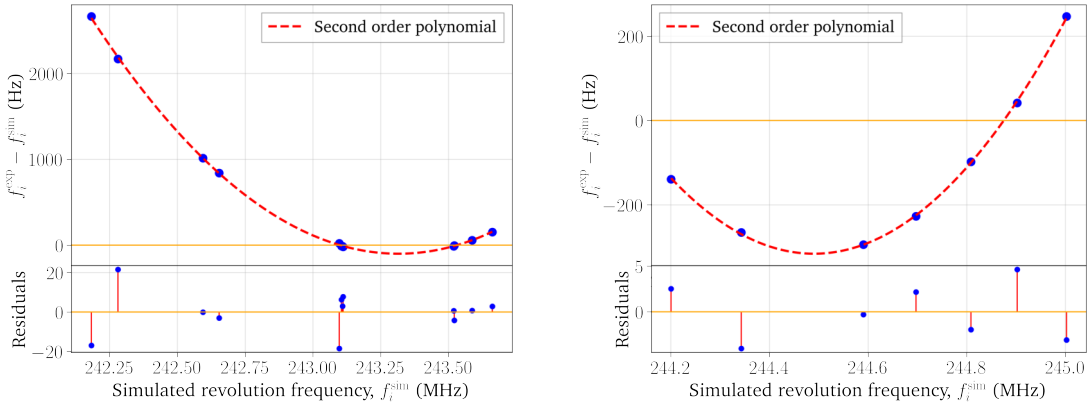

(a) Data of May 2021 from E143.

(b) Data of June 2021 from E143.

Figure 3.9. Comparison between simulated and measured frequencies, alongside the fit and its residuals for two different data subsets.

Hence, the velocity information is encapsulated within the polynomial fitting.

Identifying particles within the ISOCHRONOUS WINDOW becomes straightforward since the approximation Eq. (3.4) is valid enough, although we can already notice a small parabolic deviation. By fitting this deviation with Eq. (3.5), we can obtain the polynomial coefficients and correct the deviation. After making these corrections, there is nearly a direct match between the simulated and observed peaks within the whole spectrum, as illustrated in Fig. 3.9. However, the potential for erroneous identifications exists due to the overlap of harmonics and the large amount of possible fragments. This is explored in §3.3.2.2.

3.3.2.2 Harmonic overlapping

Non-destructive Schottky cavity detectors enhance beam monitoring and facilitate precise mass and half-life measurements, as highlighted in §3.1.3.1. Pursuing higher mass (frequency) resolution requires higher resonant frequencies, or equivalently, higher harmonics. However since the Schottky bandwidth increases linearly with the harmonic number, we encounter the issue of HARMONIC OVERLAP. This phenomenon causes different ion species at distinct harmonics to coincide at the same revolution frequency, potentially leading to signal contamination. Therefore, we need to develop different identification strategies to identify and solve this contamination. The most recent Schottky cavities [152, 153] typically operate within the $(120, 130)$ and $(208, 215)$ harmonic ranges, where between $(8, 16)$ harmonic superpositions may occur within the same measured frequency spectrum, as demonstrated in Fig. 3.10. A mathematical investigation into harmonic overlap is addressed in App. B.

To unambiguously identify each species, several strategies can be utilized:

› Verify the presence of the same peak across different harmonics, since each species has a

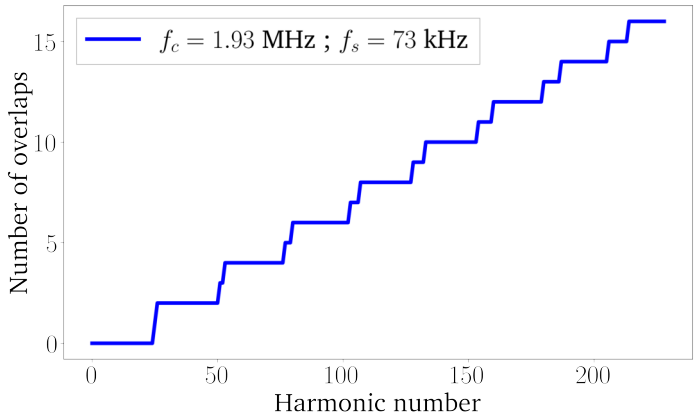

Figure 3.10. Number of overlaps as a function of the harmonic number, assuming an infinite number of Schottky bands. f_c and f_s denote the average EIGENFREQUENCY and BANDWIDTH, as measured in a data subset of experiment E143, respectively.

unique EIGENFREQUENCY.

- Examine the shape and spread of neighboring peaks for consistency, since they should be similar to other ions in the same mass-to-charge region.

- Perform a mass measurement to check for significant deviations from the expected values, indicating potential misidentification.

These procedures help to confirm the identification of each peak and whether it has contamination. The subsequent challenge is determining how to effectively use data that may be contaminated. A potential solution to the contamination lies in peak deconvolution, aiming to isolate the true peak from overlapping signals. This approach, however, demands precise knowledge of the peak shape at the given revolution frequency, which is complex to model. More information can be found in App. C.

Once we have identified our ions, we determine the mean and standard deviations of the peak distributions by means of Gaussian fitting, and we feed this values to the mass (§3.3.3) and half-life (§3.3.4) determination routines.

3.3.3 Mass determination

The detailed mathematical foundations of the commonly employed method for mass measurements at storage rings can be found in the precursor [163], other theses [164–166], and papers [167]. In this subsection, I will resume the concepts and how they were implemented in the PYTHON library RIONMASS [168] for performing mass measurements of summed-up isochronous spectra.

Firstly, we import the experimental data: measured revolution frequency, harmonic number,

ion species, peak width and their corresponding errors, and the Atomic Mass Evaluation [169] (AME) data for these ions (if known) and their electron binding energies [170]. For the AME data, we use the PYTHON package BARION [171] which already implements a connection to the NUBASE [172] database and downloads the file, reads it and subtract information. For the electron binding energies, we scrap the data from [170]. Once we have all the information, we pass to perform the calculations.

First, we perform a P^{th} order polynomial fit of the m/q as a function of the revolution frequency (or time) of the reference ions. Consequently, we perform what is known as self-calibration. For every ion that we consider as a reference, we perform a LEAST-SQUARES fit of the (AME) mass-to-charge ratios as a function of the revolution frequency (time) with a P^{th} order polynomial iteratively trying to minimize our objective function, which is in this case a reduced chi-square (χ^2):

$$\left(\frac{m}{q}\right)_i = \sum_{p=0}^{P} a_p f_i^p, \tag{3.8}$$

$$\left(\frac{m}{q}\right)_r = \left(\frac{m}{q}\right)_{\text{AME2020}}, \tag{3.9}$$

$$d\left(\frac{m}{q}\right)_i = \frac{d\left(\sum_{p=0}^{P} a_p f_i^p\right)}{df_i}\sigma_{f_i} = \sum_{p=1}^{P} p a_p f_i^{p-1}\sigma_{f_i}, \tag{3.10}$$

$$\Delta\left(\frac{m}{q}\right)_r = \Delta\left(\frac{m}{q}\right)_{\text{AME2020}}, \tag{3.11}$$

$$\left(\frac{m}{q}\right)_i - \sum_{p=0}^{P} a_p f_i^p = l_i \pm \Delta_i, \tag{3.12}$$

$$\chi^2 = min\left(\sum_{i=1}^{N} \frac{\left(\left(\frac{m}{q}\right)_i - \sum_{p=0}^{P} a_p f_i^p\right)^2}{\left(\Delta\left(\frac{m}{q}\right)_{i,\text{AME2020}}\right)^2 + \left(\sum_{p=1}^{P} p a_p f_i^{p-1}\sigma_{f_i}\right)^2}\right). \tag{3.13}$$

This procedure is repeated for each reference ion (N in total) by turning them "off" as references, thus deriving their mass-to-charge ratio (m/q) from the fitting process while treating the m/q ratios of all other reference ions as known, based on the AME values. As a result, we acquire global fitting parameters a_p that minimize Eq. (3.13). For any ions whose values are not previously known, their m/q ratios can be determined using Eq. (3.8).

For high-precision mass measurements, we have to exclude reference ions with poor signal-to-noise ratio (S/N) and significant mass uncertainties (usually over 20 keV). This can be solved by establishing a criteria based on the amplitude under the peaks. Moreover, it is essential to eliminate from our routine the peaks containing unresolved isomers, unresolved different ion species, contaminating signals from other harmonics, or noise. All of these contaminants are typically identifiable on the isochronicity curve §3.2.2 or, ultimately, at the mass measurement

procedure.

3.3.3.1 Excitation energy determination

Mass measurements in storage rings are typically conducted using polynomial fitting, as described in §3.3.3. This method uses the information of all ions within the ring by using Eq. (1.4). But, is it necessary or even optimal to use all of this information?

I propose a simplified and intuitive approach applicable to the measurement of excitation energies. Assuming almost identical velocity distribution[10] between isomer and ground state, and that both are within the ISOCHRONOUS WINDOW, the second term of Eq. (1.4) is negligible. Moreover, taking into consideration that $\Delta m = w$ between the isomer and ground state, the expression is simplified to:

$$\omega = \frac{\Delta f}{f_{gs}} m_{gs} \gamma_t^2. \tag{3.14}$$

The relative frequency distance (Δf) is calculated by determining the centroids and standard deviations of both distributions by, generally, Gaussian fitting. Finally, γ_t can be determined from the isochronicity curve. Like this, we are using the information of all the ions but without introducing their mass errors into our measurements, which can constrain the precision on the isomer mass determined.

3.3.4 Half-life determination

In this thesis, a **new approach** to determine the half-life of exotic[11] short-lived species has been developed. Unlike previous experiments, which continuously monitor beam loss post-injection [133, 173, 174] or counting frequency shifts [175, 176], our approach adds-up time-resolved spectra (as discussed in §3.3.1.4) from multiple injections and does not directly count decaying particles; instead, we observe the signal's disappearance induced by these particles at specific frequency channels. This method differs fundamentally from that of "traditional" particle detectors, like double-sided silicon strip detectors, which **physically intercept** reaction products.

Each injection may carry one or a few ions of interest, and the aggregate spectrum exhibits the characteristic decay curve, synchronized by the common injection time. It is important to stress that with RSCs we are single-ion sensitive when we have a few ions Fig. 3.11. Therefore, this motivates us to do measurements with as few ions as possible and as many times (injections) as possible in order to exploit the single-ion sensitivity, which implies the adding-up technique.

In such a way, when peaks are completely resolved, the measurement is straightforward: we have to select the frequency channels that contain the ion species and monitor their temporal

[10] Intuitively, considering the production mechanism, we can assume that both ground and isomeric states are produced with the same energy, but due to the isomer being excited, having less velocity.

[11] With low yield.

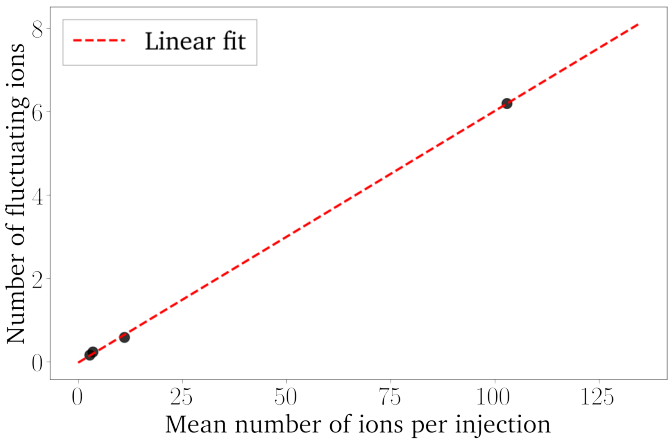

Figure 3.11. Linear relation between the mean number of ions and strength of the fluctuations in number of ions.

evolution. For contaminated peaks, measurements can be conducted using the method outlined in App. C. The integrated noise power of every peak in the summed spectrum is then directly proportional to the corresponding number of stored particles (as given by Eq. (3.1)). The validity of this analysis approach has been thoroughly tested by dedicated MONTE CARLO simulations [177] and cross-checked by extracting individual decay times, the details of which will be published elsewhere.

Chapter 4

The Experiment E143

In this chapter, the results from experiment E143 [140] are presented. Firstly, the beam time experience is detailed in §4.1. Following this introduction, the chapter presents the results. It covers the identification process (§4.2), the analysis of isochronicity curves (§4.3), and their implications for mass resolving power (§4.4), demonstrating the highest resolving power ever achieved in IMS and ranking among the highest at storage rings. The subsequent section, §4.5, highlights some of the most precise mass measurements achieved in storage rings, highlighting the improvement on the mass uncertainty of ^{69}As and a 3σ mass deviation on ^{72}As, in agreement with a recent study. Finally, the chapter presents the half-life measurements, including the first measurement of the nuclear two-photon decay half-life in ^{72}Ge (§4.6.1) and measurements of pure single-photon decays (§4.6.2).

4.1 Beam time story

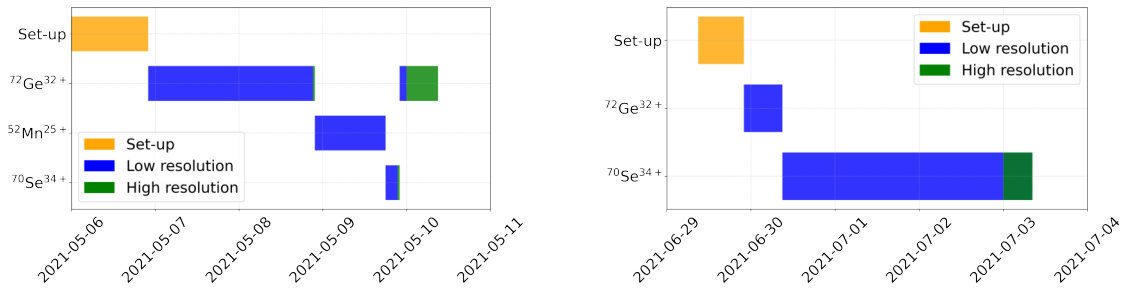

(a) First part of the beam time schedule of the experiment E143.

(b) Second part of the beam time schedule of the experiment E143.

Figure 4.1. Beam time schedule for experiment E143 conducted in May and June/July 2021.

Figure 4.1 shows a schematic overview of the beam time schedules that took place in May 2021

(Fig. 4.1a) and between June-July 2021 (Fig. 4.1b). In both, the experimental set-up is depicted in orange. It encompasses (among others) various stages including energy calibration post-stripper, determination of the γ_t ion-optical parameter with the electron cooler and set-up of the data acquisition system. In blue are highlighted the low-resolution settings where we had broader peak widths, hindering the resolution of low-lying states. In green are outlined the high-resolution settings from where we can find the data of the results for ^{72}Ge and for ^{70}Se obtained within this thesis.

The transitions from low-resolution to high-resolution settings were achieved by changing the energy of the ions and by trying different scraper positions. By changing the energy we can move the isochronous condition to other mass-to-charge ratio while by searching for different scrapper positions we can reduce the momentum spread.

As we can see in Fig. 4.1a and in Fig. 4.1b, most of the beam time was spent into the set-up (taking also into account the low-resolution settings). This was due to the novelties of the methodology:

- First time observed overlapping harmonics in IMS.
- Shortest half-live measured with S+IMS.
- First time achieving such high resolution in IMS.

During the first beam time (see Fig. 4.1a), after achieving a high-resolution setting for $^{72}\mathrm{Ge}^{32+}$ it was decided to shift the focus on searching of a new low-lying 0^+ state in $^{70}\mathrm{Se}^{34+}$. This was the second motivation of the experiment proposal [140]. As an intermediate step, we tried to calibrate the setting on $^{52}\mathrm{Mn}^{25+}$ in order to try to resolve its $377.749(5)$ keV [134] isomeric state. However, the setting was not on $^{52}\mathrm{Mn}^{25+}$, it was misidentified. Nevertheless, the mass resolving power was good enough and the focus was shifted to $^{70}\mathrm{Se}^{34+}$. For that, while having γ_t fixed, the energy of the ions was changed systematically since we did not have the necessary analysis tool to determine the exact energy inside the ring. At the end a high-resolution setting was achieved, but not isochronous for the targeted ion, as can be seen in the results Fig. 4.7. After several hours of measurement on $^{70}\mathrm{Se}^{34+}$, there was no direct evidence of an isomer detected. Consequently, it was decided to shift back to the $^{72}\mathrm{Ge}^{32+}$ setting, where we could recover a very similar high-resolution setting as previously, albeit with extended operation time (approximately 8 hours) to increase the statistics.

Due to the challenges faced during the **first** implementation of S+IMS (see Chap. 3) at the ESR, and because the full requested beam time was not allocated [140], the second part of the proposal did not record enough events. Recognizing the difficulties and the high discovery potential by the GSI management, a follow-up beam time was conducted in June-July 2021 focusing on $^{70}\mathrm{Se}^{34+}$. In this case, initially the set-up was aligned to $^{72}\mathrm{Ge}^{32+}$ to compare with the setting used in the

May run. However, the mass resolving power achieved was not even enough to resolve nuclides within 4 MeV. Nonetheless, we still could compare the main features such as the center frequency. This led us to use a higher harmonic (h) since the revolution frequencies were smaller than in the May beam time. Consequently, the focus was switched to $^{70}Se^{34+}$. In that mass-to-charge region both $^{72}Br^{35+}$ and its 100 keV isomer were present. The objective was to reach a setting where this isomer could be distinctly resolved in addition to be expectant to find a peak around $^{70}Se^{34+}$, indicating a **new** low-lying 0^+ state.

4.2 Ion identification

One of the key characteristics of Schottky-induced signals in storage rings is their intrinsic periodicity. This periodicity allows for the identification of each observed peak. Our detectors do not work in the frequency range where the revolution frequency of the ions (EIGENFREQUENCY) is observed, but rather they work at a higher frequency where multiples of it, denoted by h, are observed (refer to §3.1.3 for more information). Due to this, in the broadband measurements, we encounter harmonic overlap, a phenomenon detailed in App. B and §3.3.2.2. Consequently, the periodicity observed in our data does not imply that all peaks correspond to unique ions; some are repeated, like the ones shown in Fig. 4.3. This repetition is leveraged to unambiguously identify each peak. Figure 4.3 displays the broadband spectrum captured by the NTCAP, connected to the 245 MHz cavity, during the first high-resolution setting of $^{72}Ge^{32+}$ (see §4.1). Upon examining Fig. 4.3, one of the initial observations is the presence of a consistent three-peak structure that always repeats separated by the same spacing. By analyzing the distance between these peaks, we can determine their EIGENFREQUENCIES and the respective harmonic (h). The three ions identified, $^{72}Ge^{32+}$, $^{74}As^{33+}$, and $^{76}Se^{34+}$, coincide with the highest yields expected from LISE++ (refer to Fig. 4.2), as illustrated in Fig. 4.2a.

This (pre)identification can be realized without any prior knowledge of the ring settings, making it the initial step. After this preliminary identification, the identified peaks are input into our identification software, RIONID. As outlined in §4.2, RIONID is based on the principle that in storage rings, the ions' revolution frequency directly correlates with their mass-to-charge ratio, as per Eq. (3.3). Utilizing the frequency data from our pre-identified ions and using the tabulated masses [169] of the expected yields (as predicted by LISE++), we can simulate the expected revolution frequencies of these anticipated fragments and overlay them on the experimental data as seen in Fig. 4.3. As mentioned in §3.3.2, discrepancies between the simulated and experimental data were observed but can be adjusted using a second-order polynomial correction as demonstrated in §3.3.2, particularly in Fig. 3.9a and Fig. 3.9b.

Working within a narrow frequency band (20 kHz), as with the RSAs data (refer to §3.1.3.2), makes identification challenging without additional information because these repeating structures,

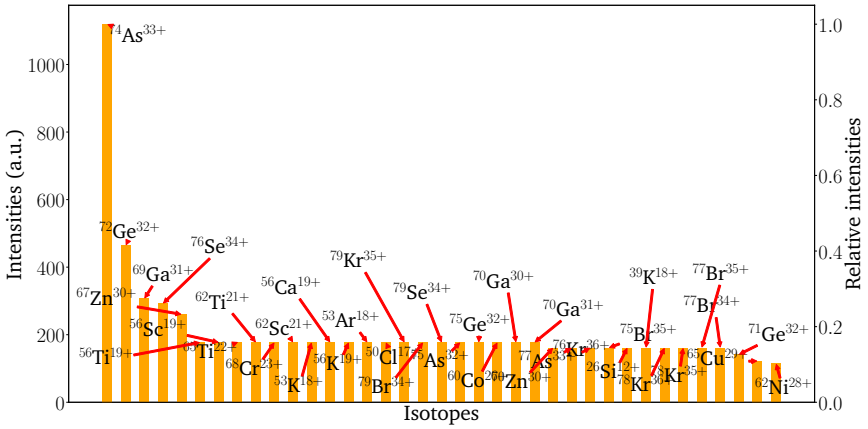

(a) Most expected fragments for the ^{72}Ge setting from LISE++ calculations.

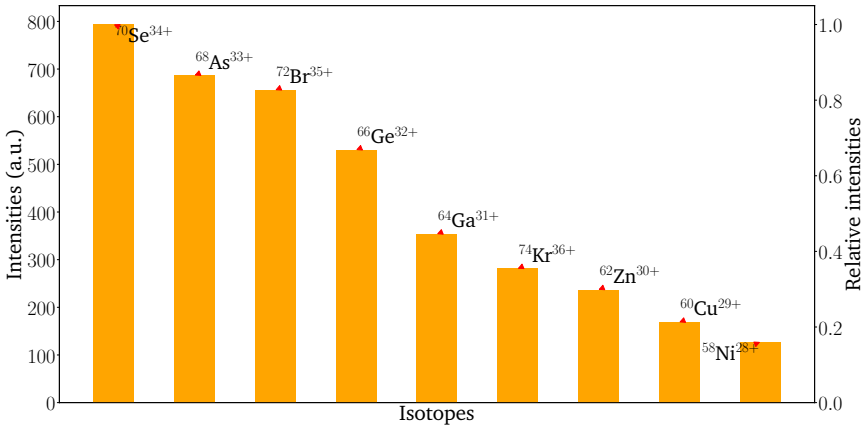

(b) Most expected fragments for the ^{70}Se setting from LISE++ calculations.

Figure 4.2. Comparison of the most expected (over 100 arb. units of intensity) fragments from LISE++ for each setting.

as discussed above, are not observable in such a restricted bandwidth. Figure 4.4 presents the first high-resolution data set for $^{72}Ge^{32+}$ in both Schottkies[1].

The data, centered around the frequency of $^{72}Ge^{32+}$, demonstrate a clear distinction in comparison: peaks are more spread out at 410 MHz compared to 245 MHz, as expected, since the 410 MHz Schottky operates at a higher harmonics. Consequently, some peaks that are detected at the edges of the measured frequency range in the 245 MHz detector do not appear in the 410 MHz detector, because they fall outside its range. Figure 4.4 also highlights the issue of HARMONIC OVERLAP, as discussed in §3.3.2.2. Specifically, a peak distribution visible on the right side of the center peak at 410 MHz, but not at 245 MHz, is observed. This additional peak arises from an ion with a significantly different mass-to-charge ratio, located far from the ISOCHRONICITY WINDOW,

[1]Note that there is no evidence of the $^{72m}Ge^{32+}$ isomer. This absence is because the isomer has completely decayed by this time (after 1.75 s from injection).

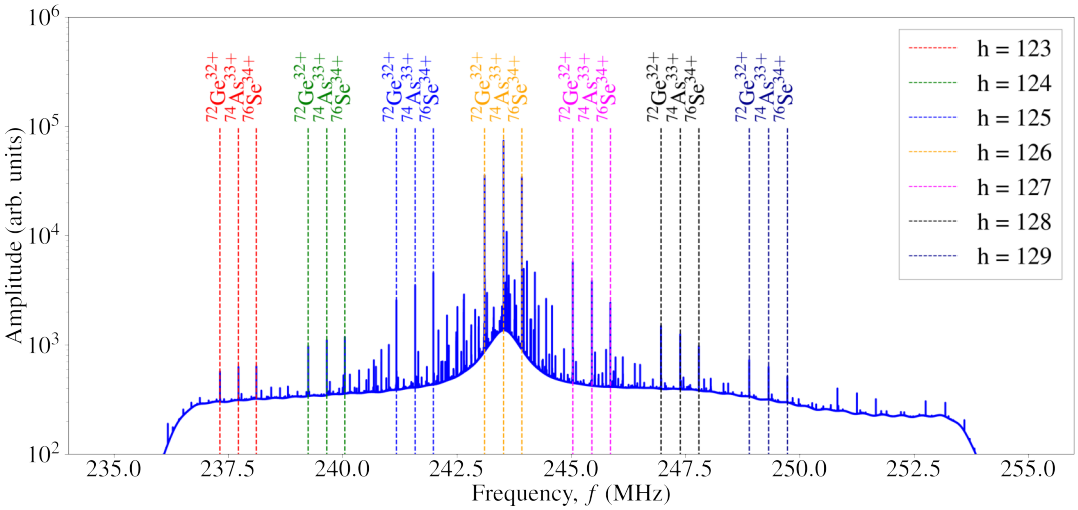

Figure 4.3. Spectrum displaying revolution frequency versus amplitude from the first high-resolution setting on ^{72}Ge^{32+}. The amplification curve of the 245 MHz detector is clearly visible. A three-peak structure has been identified and superimposed on the experimental distribution.

as indicated by its **broad** and **asymmetric** shape. It was identified as coming from ^{53}Cr^{24+}, but from a lower harmonic (the 125$^{\text{th}}$ instead of the 126$^{\text{th}}$).

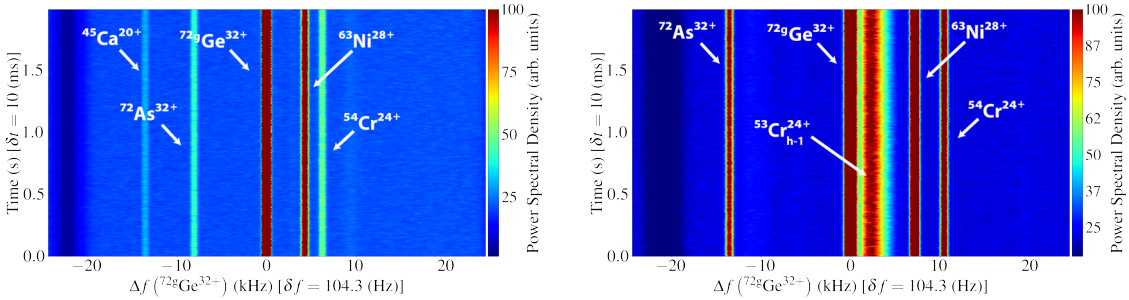

(a) Spectrogram (time versus frequency) from the 245 MHz Schottky cavity detector. The ions identified belong to the harmonic $h = 126$.

(b) Spectrogram (time versus frequency) from the 410 MHz Schottky cavity detector. The ions identified belong to the harmonic $h = 211$.

Figure 4.4. Comparison of the spectrograms from the 245 MHz (left) and 410 MHz (right) detectors for the first high-resolution setting on ^{72}Ge^{32+}.

Following the described methodology across all different settings, I compiled all the identified ions within experiment E143, excluding isomers, in Tab. 4.1 and Tab. 4.2. The isomers identified in each setting are presented in Tab. D.8 and Tab. D.9. In the following section (§4.3), I show the peak characteristics of each identified ion with the isochronicity curves of each setting.

Table 4.1. Ions identified in the high-resolution settings for $^{72}Ge^{32+}$, excluding isomers. The ions are arranged in increasing order of m/q, reading from top to bottom and left to right within the table.

$^{71}Ga^{31+}$	$^{48}Sc^{21+}$	$^{64}Ni^{28+}$	$^{73}Ge^{32+}$	$^{57}Mn^{25+}$	$^{41}Ar^{18+}$	$^{66}Cu^{29+}$
$^{75}Se^{33+}$	$^{75}As^{33+}$	$^{50}Ti^{22+}$	$^{59}Fe^{26+}$	$^{68}Zn^{30+}$	$^{77}Br^{34+}$	$^{77}Se^{34+}$
$^{43}K^{19+}$	$^{52}V^{23+}$	$^{61}Co^{27+}$	$^{70}Ga^{31+}$	$^{70}Ge^{31+}$	$^{72}As^{32+}$	$^{72}Ge^{32+}$
$^{63}Ni^{28+}$	$^{54}Cr^{24+}$	$^{74}As^{33+}$	$^{74}Se^{33+}$	$^{65}Zn^{29+}$	$^{65}Cu^{29+}$	$^{56}Mn^{25+}$
$^{47}Sc^{21+}$	$^{38}Cl^{17+}$	$^{76}Se^{34+}$	$^{67}Ga^{30+}$	$^{67}Zn^{30+}$	$^{58}Fe^{26+}$	$^{49}Ti^{22+}$
$^{69}Ga^{31+}$	$^{40}Ar^{18+}$	$^{60}Co^{27+}$	$^{71}Ge^{32+}$	$^{51}V^{23+}$	$^{62}Ni^{28+}$	$^{73}As^{33+}$
$^{42}K^{19+}$	$^{53}Cr^{24+}$	$^{64}Cu^{29+}$	$^{33}P^{15+}$	$^{44}Ca^{20+}$	$^{66}Zn^{30+}$	$^{55}Mn^{25+}$
$^{68}Ga^{31+}$	$^{57}Fe^{26+}$	$^{46}Sc^{21+}$	$^{59}Co^{27+}$	$^{48}Ti^{22+}$	$^{61}Cu^{28+}$	$^{61}Ni^{28+}$
$^{37}Cl^{17+}$	$^{50}V^{23+}$	$^{63}Cu^{29+}$	$^{39}Ar^{18+}$	$^{52}Cr^{24+}$	$^{54}Mn^{25+}$	$^{41}K^{19+}$
$^{56}Fe^{26+}$	$^{43}Ca^{20+}$	$^{30}Si^{14+}$	$^{45}Sc^{21+}$	$^{47}Ti^{22+}$	$^{32}P^{15+}$	$^{34}S^{16+}$
$^{76}Kr^{36+}$						

4.3 Isochronicity curves

In this section, for each identified ion in the high-resolution settings (refer to §4.2), we determine its spectral characteristics, including the frequency centroid and standard deviation, using Gaussian fitting. After filtering out the identified ion with lower signal-to-noise ratio, due to having low statistics or/and being located outside the resonance region of the detector, we plot the variation of the peak's spread as a function of revolution time. Following this, we perform a fit in accordance with Eq. (3.2). The reduced χ^2 was ~ 1 for each fit, ensuring the reliability of the results of the fit. Through this analysis, we gain insights into the isochronicity condition and the settings of the ring, as previously described in §3.2.2. The results of each of the isochronicity curves displayed in Fig. 4.5, Fig. 4.6, Fig. 4.7 and Fig. 4.8 are compiled in Tab. 4.3.

When comparing both settings for $^{72}Ge^{32+}$, it can be observed that the minimum spread achievable (σ_{sys}) is quite similar across both settings, indicating that the maximum mass resolving power (refer to §4.4) was similar. Also, both γ_t are nearly the same, indicating that each setting was optimized for nearly the same m/q. The significant distinction, however, lies in the rate of isochronicity loss, enveloped in σ_p/p, which is higher in the first setting ($0.283(3)$ %) compared to the second one ($0.149(1)$ %). This difference is attributed to the use of a closer scraper setting in the second setting, as mentioned in §4.1 and described in §3.2.2. By narrowing the allowed momentum space, we reduce the variations in the γ_t as a function of the orbits and diminish yield asymmetries, as shown in Fig. 3.2. Consequently, we ensure that across the ring's entire acceptance, the peaks appear more symmetric and are less pronounced. However, this comes with a trade-off:

Table 4.2. Ions identified in the high-resolution settings for $^{70}Se^{34+}$, excluding isomers. The ions are arranged in increasing order of m/q, reading from top to bottom and left to right within the table.

$^{45}Sc^{21+}$	$^{47}Ti^{22+}$	$^{32}P^{15+}$	$^{49}V^{23+}$	$^{34}S^{16+}$	$^{51}Cr^{24+}$	$^{53}Mn^{25+}$
$^{36}Cl^{17+}$	$^{55}Fe^{26+}$	$^{38}Ar^{18+}$	$^{57}Co^{27+}$	$^{59}Ni^{28+}$	$^{40}K^{19+}$	$^{61}Cu^{29+}$
$^{42}Ca^{20+}$	$^{63}Zn^{30+}$	$^{65}Ga^{31+}$	$^{67}Ge^{32+}$	$^{69}As^{33+}$	$^{46}Ti^{22+}$	$^{71}Se^{34+}$
$^{48}V^{23+}$	$^{73}Br^{35+}$	$^{75}Kr^{36+}$	$^{50}Cr^{24+}$	$^{77}Rb^{37+}$	$^{52}Mn^{25+}$	$^{27}Al^{13+}$
$^{54}Fe^{26+}$	$^{56}Co^{27+}$	$^{29}Si^{14+}$	$^{58}Ni^{28+}$	$^{60}Cu^{29+}$	$^{62}Zn^{30+}$	$^{64}Ga^{31+}$
$^{33}S^{16+}$	$^{66}Ge^{32+}$	$^{68}As^{33+}$	$^{70}Se^{34+}$	$^{72}Br^{35+}$	$^{74}Kr^{36+}$	$^{39}K^{19+}$
$^{43}Sc^{21+}$	$^{45}Ti^{22+}$	$^{47}V^{23+}$	$^{49}Cr^{24+}$	$^{53}Fe^{26+}$	$^{55}Co^{27+}$	$^{57}Ni^{28+}$
$^{59}Cu^{29+}$	$^{61}Zn^{30+}$	$^{63}Ga^{31+}$				

lower statistics since we are intercepting the beam; we are removing ions.

In comparing the settings across the experiment, the transition energy factor, γ_t, is generally kept constant, since at the ESR is preferred to fix ion-optical parameters and tune the γ of the ions to match γ_t. This is not true in the first setting for $^{70}Se^{34+}$, where a significant deviation in γ_t is observed, however the γ were not adjusted accordingly[2]. In addition, the σ_p/p (%) values are almost the same as in the first setting of $^{72}Ge^{32+}$. This similarity is because the measurements for $^{70}Se^{34+}$ were taken right after those for $^{72}Ge^{32+}$, as mentioned in §4.1, without adjusting the scraper positions. Consequently, the isochronous condition was not set on $^{70}Se^{34+}$ but in a different m/q region, as shown in Fig. 4.7. Furthermore, the parameters for the second setting align well with those of the high-resolution settings for $^{72}Ge^{32+}$. In contrast, the first setting for $^{70}Se^{34+}$ presents the lowest mass resolving power of all settings evaluated, reflected in the highest $\sigma_{\text{sys}} = 0.33(2)$ (ps) value.

Table 4.3. Parameters obtained from fitting the isochronicity curve for each setting.

SETTING	γ_t	σ_p/p (%)	σ_{sys} (ps)
$^{72}Ge^{32+}$ (1)	1.3959(1)	0.283(3)	0.12(2)
$^{72}Ge^{32+}$ (2)	1.3956(1)	0.149(1)	0.143(7)
$^{70}Se^{34+}$ (1)	1.3784(1)	0.283(4)	0.33(2)
$^{70}Se^{34+}$ (2)	1.3950(3)	0.109(8)	0.161(6)

The experimental values used in the previous figures are compiled in App. D, in Tab. D.1,

[2]This was because the behavior of the S+IMS was not fully understood at the time. Now, it should be straightforward.

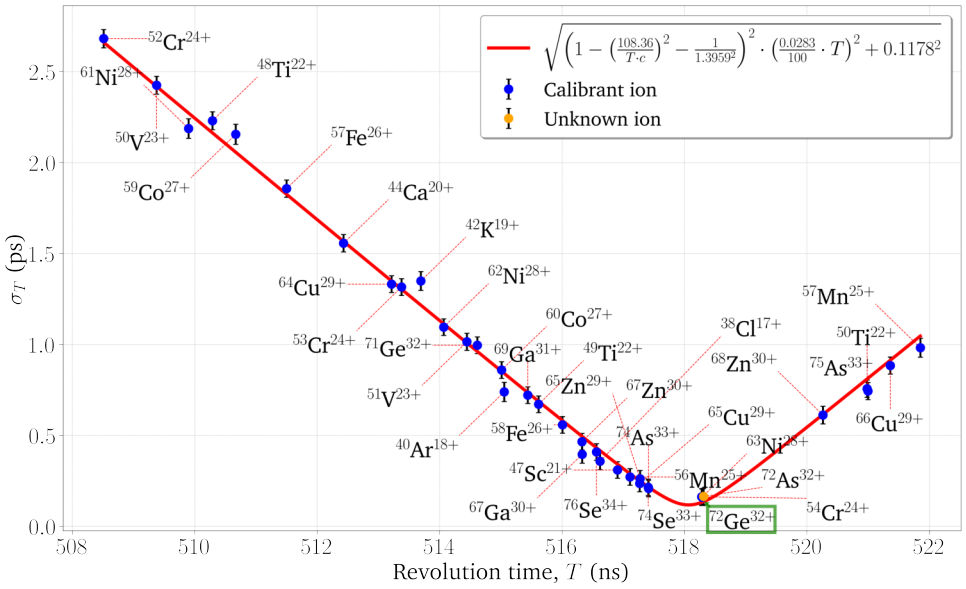

Figure 4.5. Isochronicity curve of the first high-resolution setting achieved on $^{72}Ge^{32+}$, which is highlighted within the green box. See discussion in §4.3.

Tab. D.2, Tab. D.3, Tab. D.4, Tab. D.5, Tab. D.6, Tab. D.7.

These isochronicity curves serve as a fundamental understanding of the S+IMS. Moreover, they can be connected to the mass resolving power that is achieved. This is further discussed in §4.4.

4.4 Mass resolving power

From the isochronicity curves discussed in §4.3, we can convert the frequency (time) spreads (σ_f or σ_T) into spreads in mass, and subsequently into mass resolving power (R) and the minimum resolvable peak width at full width at half maximum (FWHM). According to Eq. (1.4), for isochronous ions $\gamma \to \gamma_t$, simplifying Eq. (1.4) into:

$$\frac{\Delta f}{f} = -\frac{1}{\gamma_t^2}\frac{\Delta(m/q)}{m/q}. \tag{4.1}$$

Therefore, defining the resolving power at FWHM as:

$$R = \frac{m}{\Delta m} = \frac{1}{\gamma_t^2}\frac{f}{2\sqrt{2\ln(2)}\sigma_f}, \tag{4.2}$$

where f is the revolution frequency and σ_f the standard deviation of the peak in frequency. For the ground state of $^{72}Ge^{32+}$ in the second setting, we predict:

$$R = \frac{1}{(1.396)^2}\frac{243105253.5}{2\sqrt{2\ln(2)}58.2} \approx 9.1\times10^5. \tag{4.3}$$

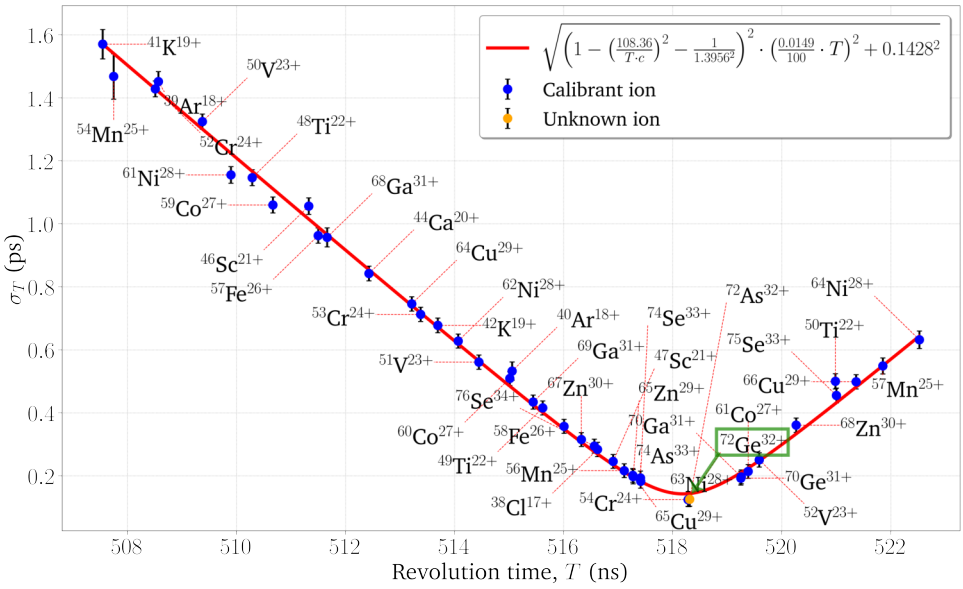

Figure 4.6. Isochronicity curve of the second high-resolution setting achieved on $^{72}Ge^{32+}$, which is highlighted within the green box. See discussion in §4.3.

This represents the **highest mass resolving power** reported so far in IMS. It enables us to differentiate an isomeric state in $^{72}Ge^{32+}$ with a mass difference (or excitation energy) at FWHM of:

$$\Delta m = m(^{72}Ge^{32+})/R \approx \mathbf{74\,keV}. \tag{4.4}$$

However, $^{72}Ge^{32+}$ lacks an isomer with this specific excitation energy, preventing us from validating this remarkable prediction experimentally. Nonetheless, the high-resolution settings for $^{70}Se^{34+}$ do include $^{72}Br^{35+}$.

^{72}Br has an isomer with energy $100.76(15)$ keV [134] and a half-life of $10.6(3)$ s [134] in its neutral state. Therefore, in terms of half-life we should observe it. Performing the same calculation as for $^{72}Ge^{32+}$, for $^{72}Br^{35+}$ within the second high-resolution setting of $^{70}Se^{34+}$, we deduce a resolving power of $R \approx 6.3 \cdot 10^5$, allowing us to, in principle, resolve a $\Delta m \approx 106$ keV isomeric state (assuming it is produced and stored within the ring). This prediction was confirmed by a clear separation of the isomeric and ground state, visible in Fig. 4.10 and Fig. 4.11. This demonstrates that we can use the isochronicity curve to measure and monitor the ion-optical parameters, while tuning the ring settings with the goal of improving our resolving power.

When we move out of the ISOCHRONOUS WINDOW, the relation described in Eq. (4.1) is no longer true; the second term in Eq. (1.4) starts to influence, leading to broader peaks. Consequently, this leads to a decrease in resolving power. The rate of deterioration is related to the σ_p/p ratio, as already described in §4.3.

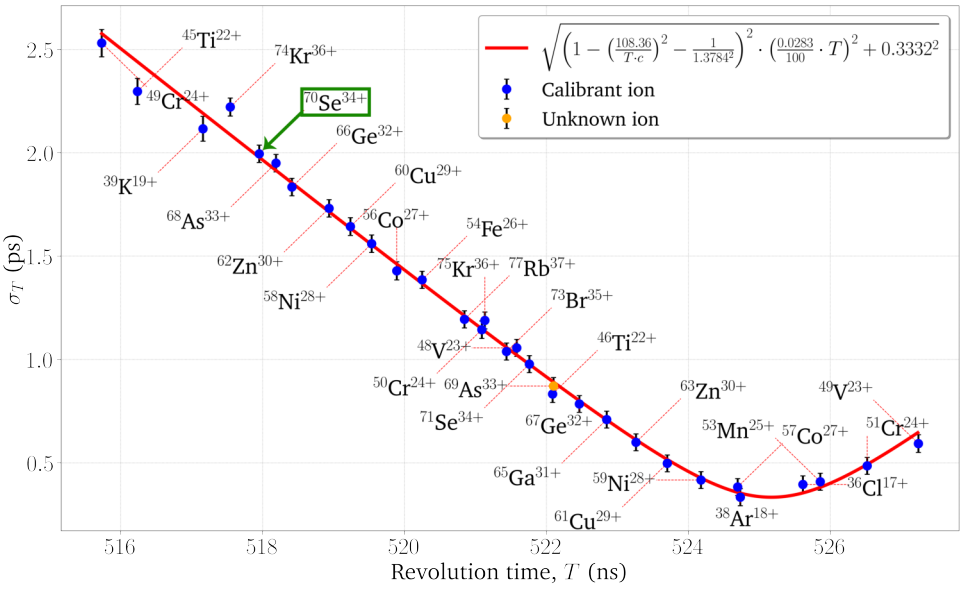

Figure 4.7. Isochronicity curve of the first high-resolution setting on $^{70}Se^{34+}$, which is highlighted within the green box. See discussion in §4.3.

4.5 Mass measurements

Mass measurements were conducted using the polynomial fitting method detailed in §3.3.3, applied to the ions depicted in the isochronicity curves from §4.3. This section presents the calculated masses.

Figure 4.12 and Fig. 4.13 show the difference between the measured masses and the tabulated values. Given that all the ions are close to the valley of stability, their masses have already been measured with high-precision elsewhere. Consequently, they can be used as references. The methodology used for mass determination, as outlined in §3.3.3, involves a fitting procedure considering all ions. However, ions located further from the isochronicity point are measured with less precision and contribute the most to the overall uncertainty affecting all measured ions. To achieve a reduced χ^2 value of 1, an additional systematic uncertainty of approximately 9 keV must be accounted for.

All the measured masses agree well within uncertainties with the AME data [169], except one, $^{72}As^{32+}$, which deviates by more than 3σ in both $^{72}Ge^{32+}$ settings (see the orange boxes in Fig. 4.12 and Fig. 4.13). A recent study (after AME2020), reports a similar downward shift in mass for ^{72}As, with a measured deviation of $12.4(40)$ keV [178] at JYFLTRAP, which aligns with our findings within 1.8σ. The results, including the newly measured values (highlighted in a green row), are tabulated in Tab. D.14 and Tab. D.17.

For the first setting on $^{70}Se^{34+}$, we again notice a measurement that significantly differs from

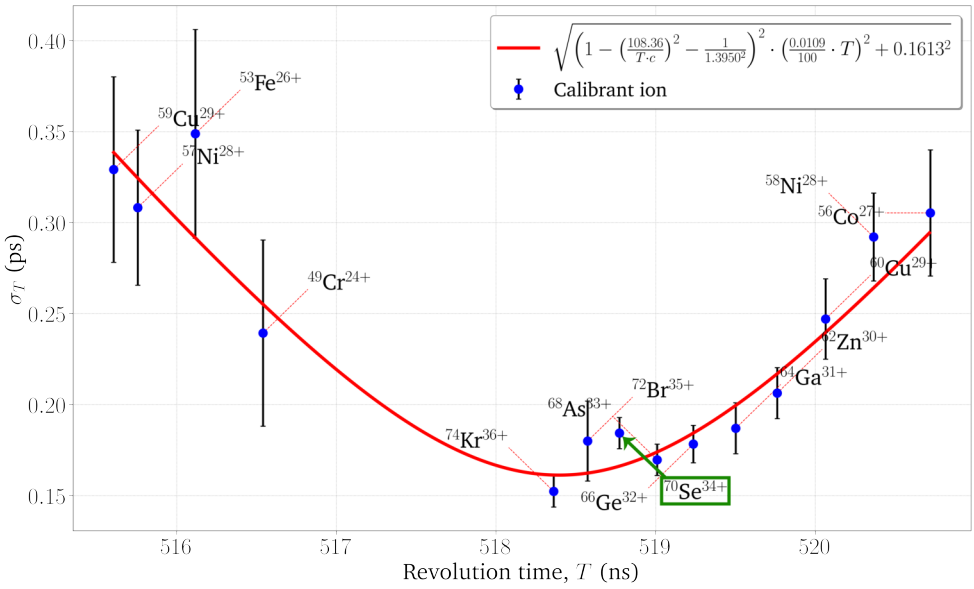

Figure 4.8. Isochronicity curve of the high-resolution setting on ^{70}Se^{34+}, which is highlighted within the green box. See discussion in §4.3.

the AME values, highlighted in the light-orange row of Tab. D.12 and in the orange box of Fig. 4.14. Specifically, ^{69}As^{33+} is listed in AME2020 [169] with an uncertainty of 30 keV. Recently, this isotope's mass was directly measured for the first time at the FRS@GSI using MR-TOF-MS, achieving a lower uncertainty of 22 keV [179]. Their value falls within 1.3σ of ours, yet our measurement presents $\sim$ 9 keV of uncertainty, which is more than a half lower. The details of this measurement are tabulated in Tab. D.12.

Finally, in the second setting on ^{70}Se^{34+}, due to low statistics we do not have as many ions stored than in the previous settings, and we do not observe any interesting results. Its results are tabulated in Tab. D.6.

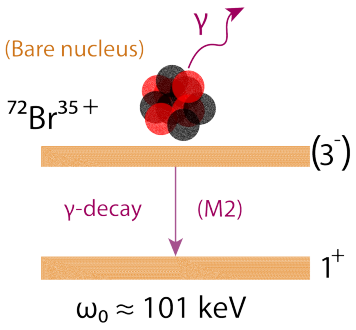

Figure 4.9. A sketch of the ^{72m}Br^{35+}, along with some of its nuclear properties (in the absence of electrons).

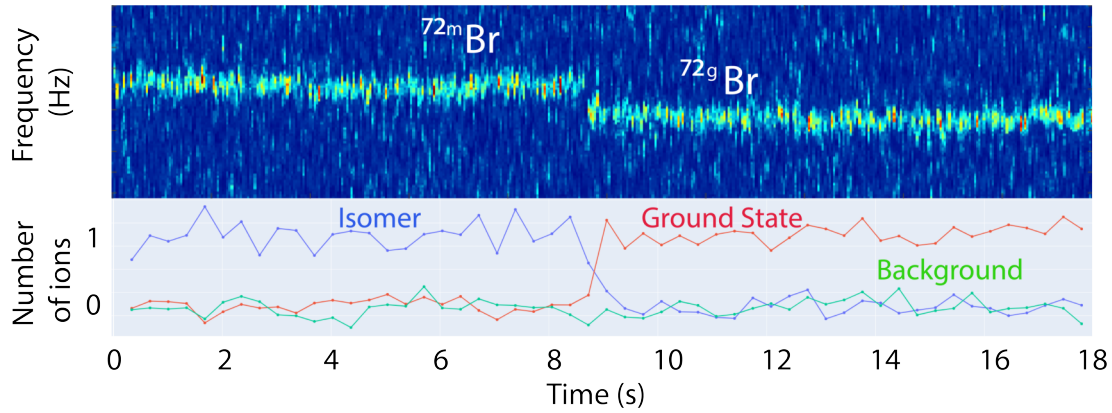

Figure 4.10. (Top) Decay of a single particle of $^{72m}Br^{35+}$ in the isomeric state to a single particle of $^{72g}Br^{35+}$ in the ground state. The excitation of the isomer is 101 keV. (Bottom) The areas of the corresponding single particles and background. (Left) Projection on the frequency axis containing the equivalence between frequency and energy.

4.5.1 Determination of the excitation energy of $^{72m}Ge^{32+}$

Part of the text, figures and tables within this subsection have already been submitted for publication to Physical Review Letters in D. Freire-Fernandez et al., Measurement of the Isolated Nuclear Two-Photon Decay in ^{72}Ge (2024) [180].

The measured frequencies and precisely known mass of $^{72}Ge^{32+}$ [169], allowed us to independently determine the excitation energy of the isomeric state via Eq. (3.14), using the method described in §3.3.3.1. Data from both RSAs and for both settings (1,2) were analyzed separately. The results are listed in Tab. 4.4. All obtained ω_0 values are in good agreement with the tabulated excitation energy [134].

Table 4.4. Measured frequency difference Δf between the isomeric and ground state and the deduced excitation energy ω_0 of the isomer for the two different data subsets (i) in each Schottky detector. The last column corresponds to the weighted average of the values obtained with each detector.

DETECTOR	i	Δf (Hz)	ω_0 (keV)	$\overline{\omega_0}$ (keV)
SD_{410}	1	2162 (8)	694.4 (31)	692.8 (19)
	2	2157 (4)	691.8 (24)	
SD_{245}	1	1301 (7)	699.7 (43)	695.0 (32)
	2	1290 (4)	692.8 (29)	

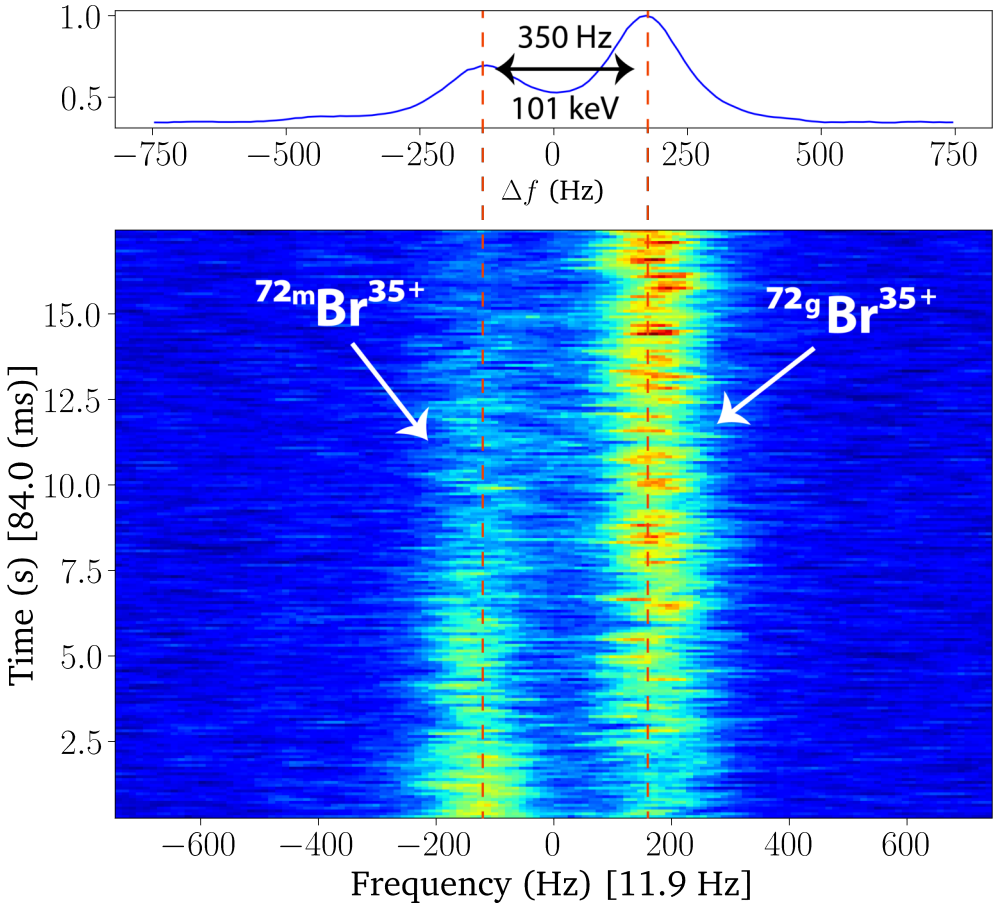

Figure 4.11. Sum of 11 spectrograms (injections), from the 410 MHz detector, containing both the ground and isomeric states of $^{72}Br^{35+}$. (Top) Projection of the spectrogram on the frequency axis, highlighting the resolution of the peaks. Between brackets can be found the time (y-axis) and frequency (x-axis) resolutions.

4.6 Half-life measurements

4.6.1 Nuclear two-photon decay in ^{72}Ge

Part of the text, figures and tables within this subsection have already been submitted for publication to Physical Review Letters in D. Freire-Fernandez et al., Measurement of the Isolated Nuclear Two-Photon Decay in ^{72}Ge (2024) [180].

As previously discussed in §2.3, ^{72}Ge is one of the few nuclides known with a ground and first (low-lying) excited states having $J^\pi = 0^+$. Consequently, single-photon decay (§1.3.3.1) and IPC (§1.3.3.3) are not allowed. In its atomic form (in the presence of electrons), the isomer decays to the ground state via IC (§1.3.3.2) with a half-life of 444.2 (8) ns [135]. However, when all electrons are removed, this decay mode is also forbidden, allowing for the observation of the rare nuclear two-photon decay (see Chap. 2). The properties of this nuclide and its decay process are represented in Tab. 4.5 and sketched in Fig. 4.16, respectively.

The trace of the isomer $^{72m}Ge^{32+}$ in Fig. 4.17 corresponds to an injection with initially three

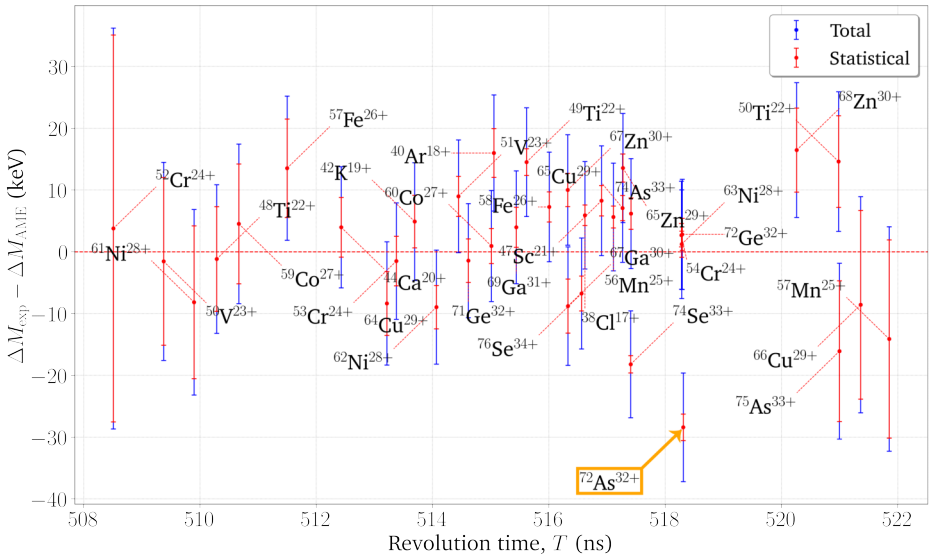

Figure 4.12. Deviation of the mass measurements from the values tabulated in AME2020 [169], using the first high-resolution setting achieved on $^{72}Ge^{32+}$. Inside the orange box is illustrated the improved mass. The improved mass measurement is depicted within the orange box. See discussion in §4.5.

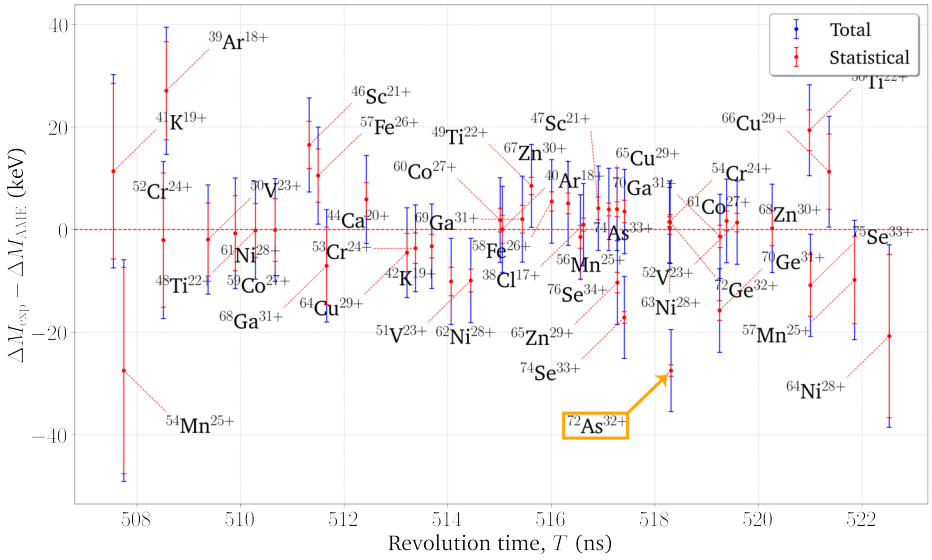

Figure 4.13. Deviation of the mass measurements from the values tabulated in AME2020 [169], using the second high-resolution setting achieved on $^{72}Ge^{32+}$. The improved mass measurement is depicted within the orange box. See discussion in §4.5.

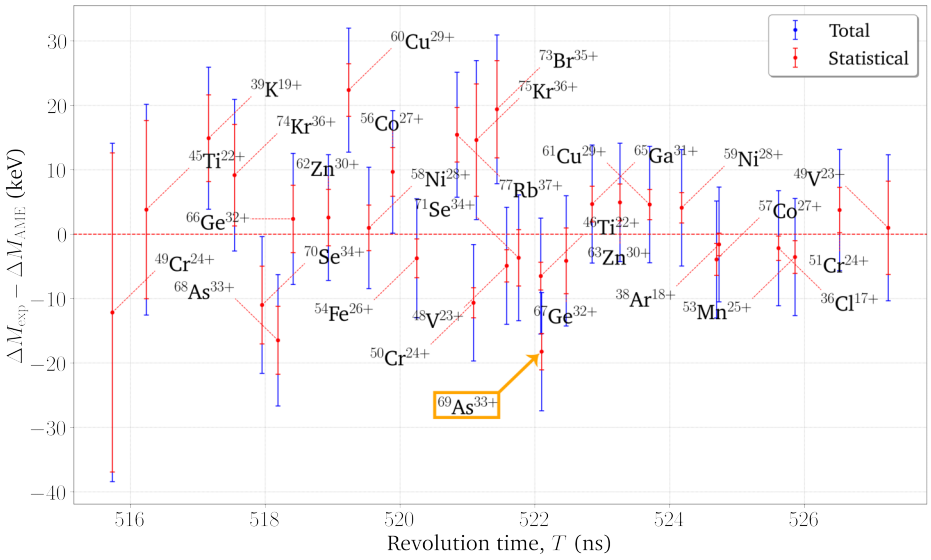

Figure 4.14. Deviation of the mass measurements from the values tabulated in AME2020 [169], using the first high-resolution setting on ^{70}Se^{34+}. The improved mass measurement is depicted within the orange box. See discussion in §4.5.

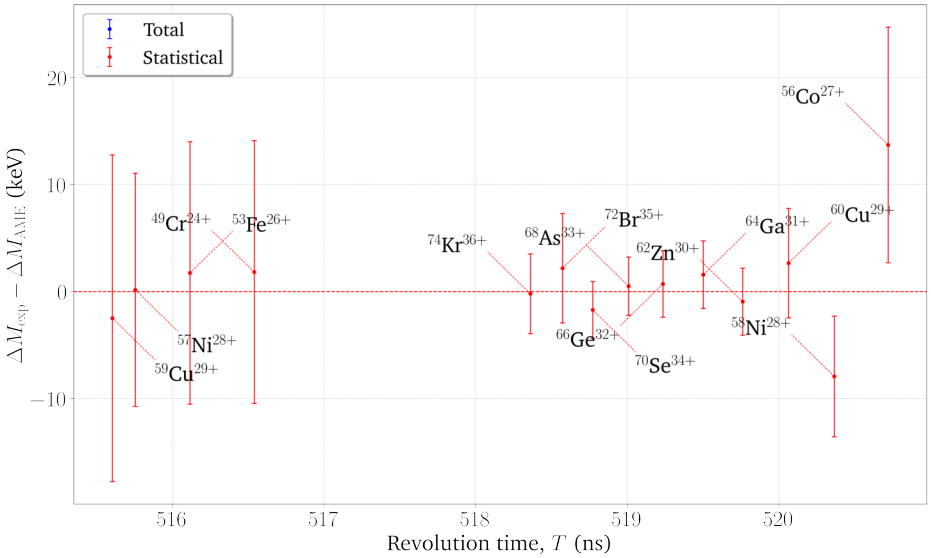

Figure 4.15. Deviation of the mass measurements from the values tabulated in AME2020 [169], using high-resolution setting on ^{70}Se^{34+}.

Table 4.5. Nuclear properties of the ground (^{g}) and first excited (^{m}) state of ^{72}Ge.

NUCLIDE	ENERGY (keV)	J^{π}	$T_{1/2}$ (ns)	DECAY MODE
^{72g}Ge	0	0^{+}	Stable	None
^{72m}Ge	691.43(4) [134]	0^{+}	444.2(8) [135]	$E0$

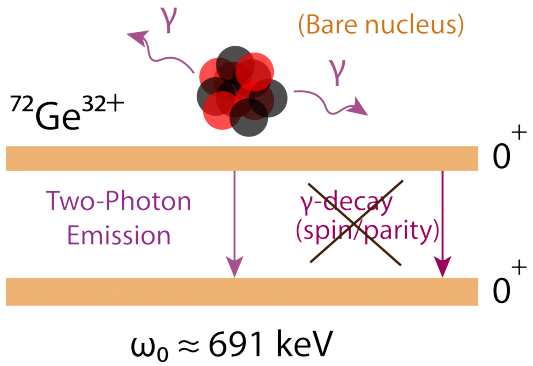

Figure 4.16. Sketch of the nuclear two-photon decay of $^{72}Ge^{32+}$ in the absence of electrons.

$^{72m}Ge^{32+}$ particles. Injections containing up to three $^{72m}Ge^{32+}$ particles were observed in the first subset of data (comprising 103 injections). In contrast, in the second subset this number is reduced approximately by half, while we recorded 17 times longer, therefore reaching higher statistics. More details were given in §4.1.

To determine the half-life of $^{72m}Ge^{32+}$ (fully-stripped[3]), all spectra measured by both RSAs were adjusted in frequency (see §3.3.1.4) by setting the center of the ^{72g}Ge peaks to 0 Hz. Afterwards, the spectra were summed up separately for each RSA and data subset. The resultant combined spectra of the 410 MHz detector during setting 1 and 2 are shown in Fig. 4.18 and Fig. 4.19, respectively. Once summed all the spectrograms, we monitor the frequency region corresponding to the isomeric state over time, as previously discussed in §3.3.4.

The decrease in intensity of the $^{72m}Ge^{32+}$ trace with time is visually evident in Fig. 4.17, Fig. 4.18 and Fig. 4.19. The peak areas for each time bin, within the red region depicted in Fig. 4.19, were extracted and fitted with an exponential function. The fitted functions and experimental data are represented in Fig. 4.21. The poorer signal-to-noise ratio of the 245 MHz detector compared to the 410 MHz detector, as discussed in §3.1.3.1, translates into an enlargement of scatter earlier in time due to background fluctuations. This can be slightly noticed in Fig. 4.21. The intensities of the stable species remained constant in the 300 ms time interval in which the isomer half-lives have been determined. This suggests minimal ion losses from other processes, such as collisions with residual gas, throughout the measurement period, as illustrated in Fig. 4.20.

[3]Note that this is equivalent to determining the (partial) half-life of the nuclear two-photon decay, as we are studying fully-stripped ions, as depicted in Fig. 4.16.

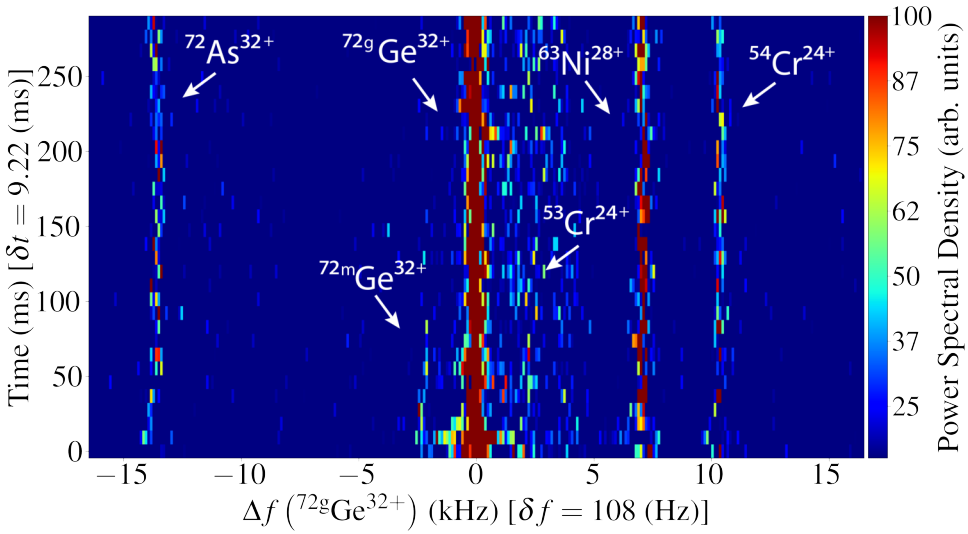

Figure 4.17. Time after injection ($\delta t = 9.22$ ms per time bin) versus revolution frequency ($\delta f = 108$ Hz per frequency bin) spectrogram of a single injection from setting 1 centered on $^{72g}Ge^{32+}$ from 0 to 300 ms. The power spectral density of each ion species is proportional to their ion number (Eq. (3.1)).

The lifetimes measured in the laboratory frame and the corresponding half-lives in the rest frame are listed in §4.6.1. All values agree within the uncertainties. The average measured half-life for the 2γ decay in the rest frame is $\overline{T}_{1/2}^{\text{rest}} = 23.9\,(6)$ ms determined by using the Lorentz factors of the isomeric states for each setting, $\gamma_1 = 1.3957\,(1)$ and $\gamma_2 = 1.3954\,(1)$.

Table 4.6. Measured lifetimes in the laboratory frame and half-lives in the rest frame for the different data subsets (i) in each Schottky detector. The last column corresponds to the weighted average of the values obtained with each detector. Figure 4.21 shows the experimental data from which the decay constants have been obtained.

DETECTOR	i	τ^{lab} (ms)	$T_{1/2}^{\text{rest}}$ (ms)	$\overline{T}_{1/2}^{\text{rest}}$ (ms)
SD_{410}	1	51.0 (35)	25.4 (17)	23.9 (6)
	2	47.7 (13)	23.7 (6)	
SD_{245}	1	48.1 (41)	23.9 (20)	22.7 (11)
	2	44.5 (28)	22.1 (14)	

From the parameters of the exponential fits, we can compute the initial number of isomers ($N\,(t = 0)$ s). Together with the number of ions in the (stable) ground state we obtain an isomeric ratio of $3.4\,(2)$ %.

In Fig. 4.22 the newly obtained partial half-life for the 2γ decay in ^{72}Ge is plotted together with the previous results on other nuclei for $0^+ \rightarrow 0^+$ 2γ transitions. For the case of the first excited

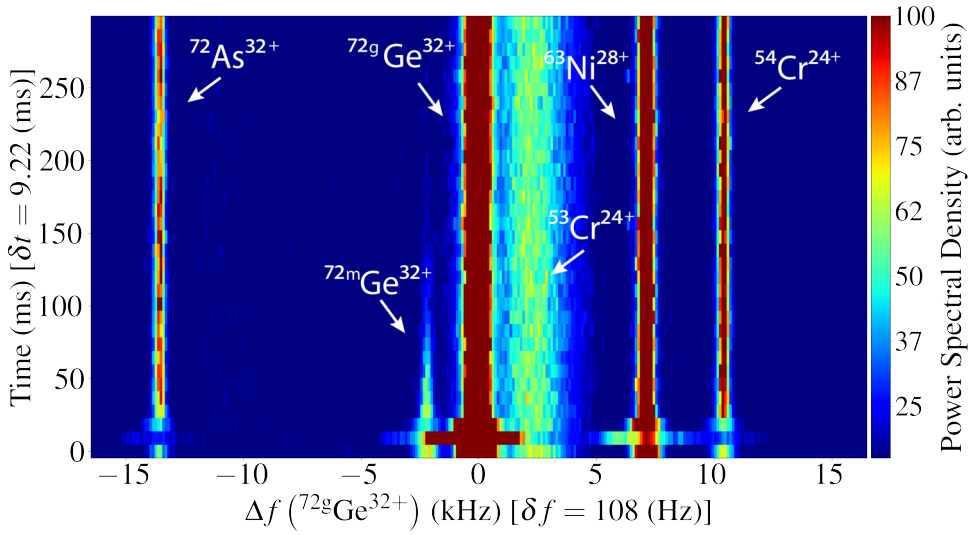

Figure 4.18. Frequency spectrogram of the sum of 102 single injections such as the one in Fig. 4.17.

state in ^{72}Ge, the measured partial half-life is approximately ten times shorter than suggested by the extrapolations via Eq. (2.2) (as shown in Fig. 4.22). This implies that the sum of all contributions in Eq. (2.2) ($M_{\gamma\gamma} = 70(2) \times 10^{-3}$ fm^3) is larger than the ones obtained in previous experiments. However, without measuring the angular correlation of the γ-rays, as could be done in Refs. [90, 97], it is not possible to determine α^2_{E1} and χ^2_{M1} individually. We therefore have to rely on shell-model calculations to estimate the $M1$ contribution.

Table 4.7. χ_d magnitudes of nuclei with low-lying $0^+_2 \rightarrow 0^+_1$ transitions.

NUCLIDE	$\lvert\chi_d\rvert \times 10^{-3}$ (fm^3)	$10^3 \times \rho^2(E0)$	R (fm)
^{16}O	0.91(5)	151(18) [65]	3.024(1)*
^{40}Ca	0.69(2)	25.9(16) [65]	4.104(1)*
^{72}Ge	0.58(1)	8.3(4) [65]	4.992(1)*
^{72}Kr	1.65(7)	67(6) [65]	4.992(1)*
^{90}Zr	0.44(1)	3.52(23) [65]	5.378(1)*
^{98}Mo	1.28(4)	26.8(17) [65]	5.533(1)*
^{98}Zr	0.82(5)	11.1(13) [65]	5.533(1)*

* R has been truncated at the third decimal. This does not influence the uncertainty $\Delta\chi_d$.

Shell-model calculations using the $jj44$ model space and the JUN45 Hamiltonian [181], and an effective $M1$ operator [181], were performed by B. Alex Brown (FRIB) to determine the paramagnetic contribution of the magnetic susceptibility χ_{M1}. In neighboring ^{74}Ge, the

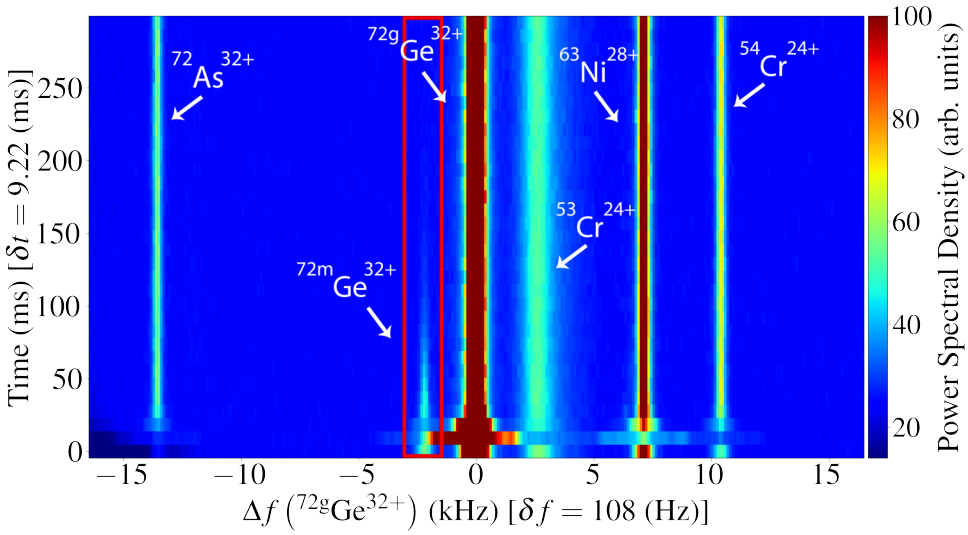

Figure 4.19. Frequency spectrogram of the sum of 2459 injections of the second-achieved high-resolution setting measured with the 410 MHz Schottky cavity. The region used for analyzing the half-life of $^{72m}Ge^{32+}$ is highlighted in red.

measured $M1$ strength distribution up to 5 MeV is in good agreement with these calculations [182]. Adding up the contributions from all theoretically expected 1^+ states up to an excitation energy of 7.5 MeV results in a contribution from the magnetic-dipole transition susceptibility of $|\,\chi_p\,| \approx 3.2 \times 10^{-3}\,\mathrm{fm}^3$. There is a strong cancellation in the terms in Eq. (2.5) as a function of E_i; if one adds just the magnitudes, the result is about four times larger. The $jj44$ model space does not include $M1$ strength coming from the $0f_{7/2}$ to $0f_{5/2}$ contribution.

The diamagnetic contribution can be estimated from the known $E0$ matrix element [65] via Eq. (2.8) as $|\,\chi_d\,| \approx 0.58 \times 10^{-3}\,\mathrm{fm}^3$. This calculation has been performed for other nuclear two-photon decay $E0$ transitions, as can be seen in Tab. 4.7. Since there is usually ambiguity in determining the sign of $\rho\,(E0)$, it is customary to use its square value, and it is what can be found tabulated times 10^3 since it is small. Therefore, the total transitional magnetic-dipole susceptibility (Eq. (2.4)) is:

$$|\,\chi_{M1}\,| \approx 3.3 \times 10^{-3}\,\mathrm{fm}^3, \tag{4.5}$$

which is small compared to the measured value of $M_{\gamma\gamma}$ and not too different to the values obtained by Kramp *et al.* [90] in doubly-magic nuclei.

The electric transition polarizabilities for $0_2^+ \rightarrow 0_1^+$ transitions are given by Eq. (2.3). For the case of low-lying 0^+ states, the electric-quadrupole transition polarizability α_{E2} may also become important, due to the extra energy term inside brackets in Eq. (2.2). By using the reduced $E2$ matrix elements from both 0^+ states to the two lowest-lying 2^+ states of ^{72}Ge [183], which usually

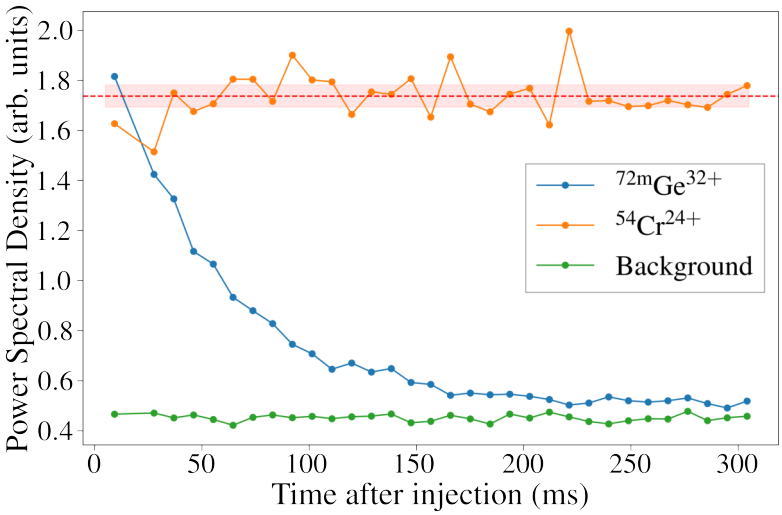

Figure 4.20. Signal of the isomer with respect to the signal of a stable ion species with similar intensity, $^{54}\mathrm{Cr}^{24+}$ in this case.

exhaust more than 90 % of the $E2$ strength, α_{E2} can be estimated to be:

$$\alpha_{E2} \approx \frac{8\pi}{25}\left[\frac{\langle 0_1^+\|M(E2)\|2_1^+\rangle\langle 2_1^+\|M(EL)\|0_2^+\rangle}{\omega_{2_1^+}-\frac{\omega_{0_2^+}}{2}} + \frac{\langle 0_1^+\|M(E2)\|2_2^+\rangle\langle 2_2^+\|M(EL)\|0_2^+\rangle}{\omega_{2_2^+}-\frac{\omega_{0_2^+}}{2}}\right]. \tag{4.6}$$

We used the following experimental parameters in order to quantify its total magnitude:

- $\langle 0_1^+\|M(E2)\|2_1^+\rangle = 0.457(4)$ e·b [184],
- $\langle 2_1^+\|M(EL)\|0_2^+\rangle = 0.35^{(+1)}_{(-2)}$ e·b [184],
- $\langle 0_1^+\|M(E2)\|2_2^+\rangle = 0.030(1)$ e·b [184],
- $\langle 2_2^+\|M(EL)\|0_2^+\rangle = 0.0144(6)$ e·b [184],
- $\omega_{0_2^+} = 691.43(4)$ keV [185],
- $\omega_{2_1^+} = 834.011(19)$ keV [185],
- $\omega_{2_2^+} = 1463.99(3)$ keV [185].

By introducing the previous empirical values into Eq. (2.3), we obtain[4]:

$$\alpha_{E2} \approx \left(3.293\times10^{-4} + 3.8835\times10^{-7}\right)\ \mathrm{keV}^{-1}e^2\mathrm{b}^2 \approx 4748.7\ \mathrm{fm}^5. \tag{4.7}$$

[4] In "GOD-GIVEN" units as introduced in §2.1: $\alpha = e^2$, with $\alpha^{-1} = 137.035999206(11)$ [186] and $1\ \mathrm{MeV}^{-1} = 197.3269804$ fm. This last conversion is used in most of the following relations.

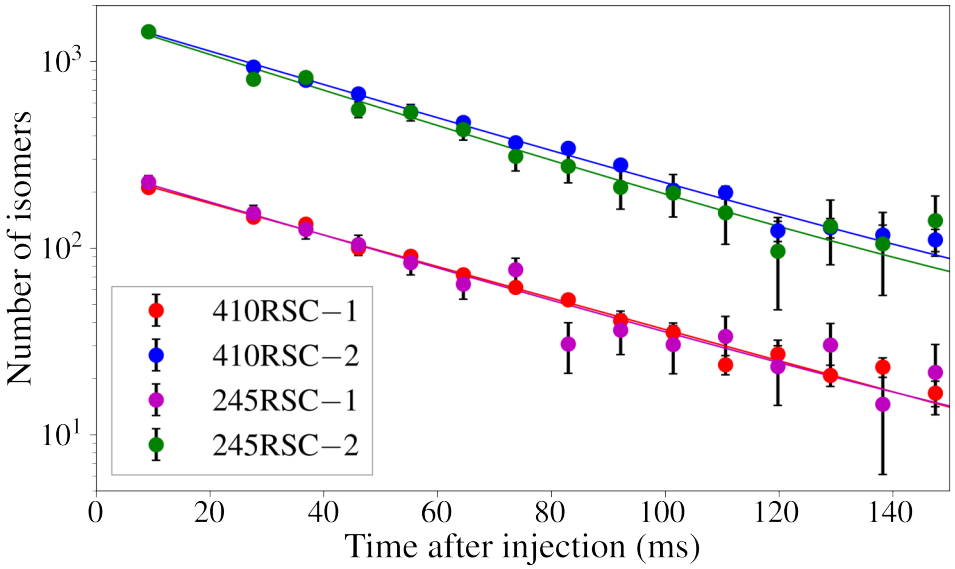

Figure 4.21. Measured nuclear two-photon decay curves during the present work, for each setting with each detector. The lifetimes obtained through the different fits are compiled in §4.6.1.

Therefore, the nuclear matrix element associated with $2E2$ transitions amounts to:

$$M_{E2} = \sqrt{\omega_0^4 \frac{\alpha_{E2}^2}{4752}} \approx 0.8 \times 10^{-3}\,\mathrm{fm}^3. \tag{4.8}$$

Obtaining a theoretical estimate for the electric-dipole transition polarizability via shell-model calculations requires including contributions from orbital transitions related to the giant dipole resonance region that lies outside the $jj44$ model space. Other theoretical approaches, such as the quasi-particle random-phase approximation, are also not applicable here since the two 0^+ states in ^{72}Ge are strongly mixed [184]. More complete set of calculations for the double-gamma matrix elements remains to be carried out. However, in view of the theoretically expected small contribution from the magnetic-dipole susceptibility and from the electric-quadrupole polarizability, it can be concluded that the electric-dipole transition polarizability is largely dominating the observed increase in transition strength. By combining the theoretical and experimental values obtained we can estimate it to be:

$$M_{\gamma\gamma}^2 = M_{E1}^2 + M_{M1}^2 + M_{E2}^2, \tag{4.9}$$

$$M_{E1} = \sqrt{M_{\gamma\gamma}^2 - M_{M1}^2 - M_{E2}^2} \approx 70 \times 10^{-3}\,\mathrm{fm}^3. \tag{4.10}$$

This finding is consistent with the presumed cancellation effect of the electric-dipole transition polarizability in the case of the doubly-magic nuclei, which should not be as pronounced in the mid-shell nucleus ^{72}Ge.

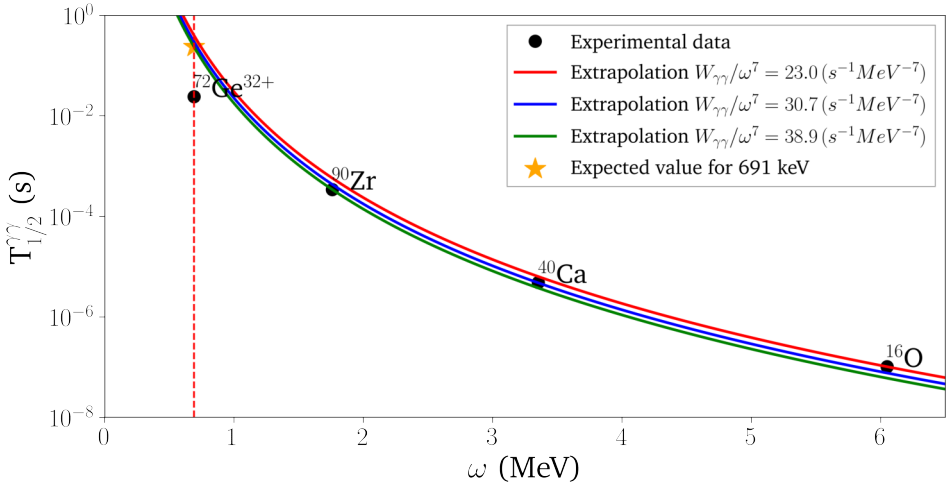

Figure 4.22. Measured nuclear two-photon decay half-lives, taken from [90, 97] and the present work, as a function of their excitation energy. The solid lines correspond to the curves obtained by considering the ratio of $W_{\gamma\gamma}$ and ω_0^7 constant, with the constant being the average (blue line), smallest (red line), and largest (green line), value of the sum of squares of the nuclear polarizabilities in Eq. (2.2). The vertical red dotted line is placed at the excitation energy of the isomeric state of ^{72}Ge.

4.6.2 Pure photon transitions in bare isomers

Isomers can experience a half-life extension in their bare state since internal-electron conversion is prohibited [133], hence allowing to observe the pure (single) photon decay. Especially for low-lying isomers with excitation energies < 1.022 MeV, this effect could enhance the precision of mass and half-life measurements, or the ability to measure them at all, considering that some half-lives can be extended by more than 200 times their half-life in neutral atoms. Furthermore, measuring the pure single-photon decay half-life ($T^{\gamma}_{1/2}$) allows for the alternative determination of the electron conversion factor α if we know their atomic half-life (refer to §1.3.3.2, specifically to Eq. (1.9)).

Through comparison of experimental α values with the corresponding theoretical values, multipolarities of nuclear transitions can be determined. Deviation of an experimental α value from the theoretical value could be expected in cases where a nuclear transition under consideration is more hindered than expected. Nowadays, most of the α factors tabulated are given by computations using BRICC [46].

In this subsection, I apply the novel method for determining the half-life of unresolved isomers described in App. C on ^{77m}Se^{34+} and ^{71m}Ge^{32+}, two isomers with very different m/q values and thus, very different peak shapes as can be seen in Fig. 4.24 and Fig. 4.25, respectively. The results presented (see Tab. 4.8) are **preliminary**, and further analysis is required. Nonetheless, they provide sufficient evidence to demonstrate the potential of the method.

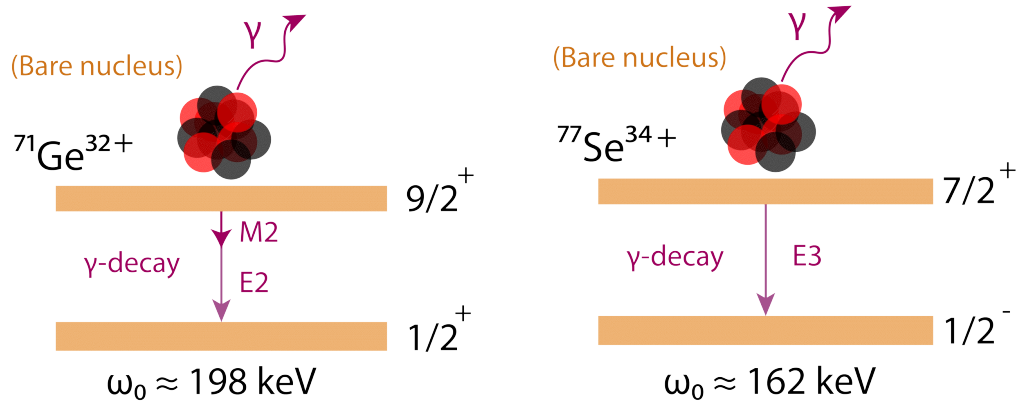

(a) Pure photon decay in ^{71m}Ge when electrons are absent.

(b) Pure photon decay in ^{77m}Se when electrons are absent.

Figure 4.23. Sketches of the observed pure photon decays in ^{71m}Ge and ^{77m}Se.

4.6.2.1 Bare ^{77m}Se

^{77}Se has an isomer at 161.9223(10) keV [134] and with a half-life of 17.36(5) s [134] in its neutral state. This isomer decays to the ground state via an IT, involving a competition between an $E3$ photon decay [134] and IC, with a theoretical electron conversion factor of (α) of 0.881(13) [46]. When all its electrons are removed (resulting in a bare nucleus, as depicted in Fig. 4.23b), its lifetime is (shortly) extended by a factor of $\alpha + 1 = 1.881(13)$. Furthermore, we must consider the relativistic nature of the stored ions, which experience an additional (time) extension factor of $\gamma \sim 1.395$, as discussed previously. Therefore, for (pure) gamma decay, the expected partial half-life would be 32.7(2) seconds in the rest frame.

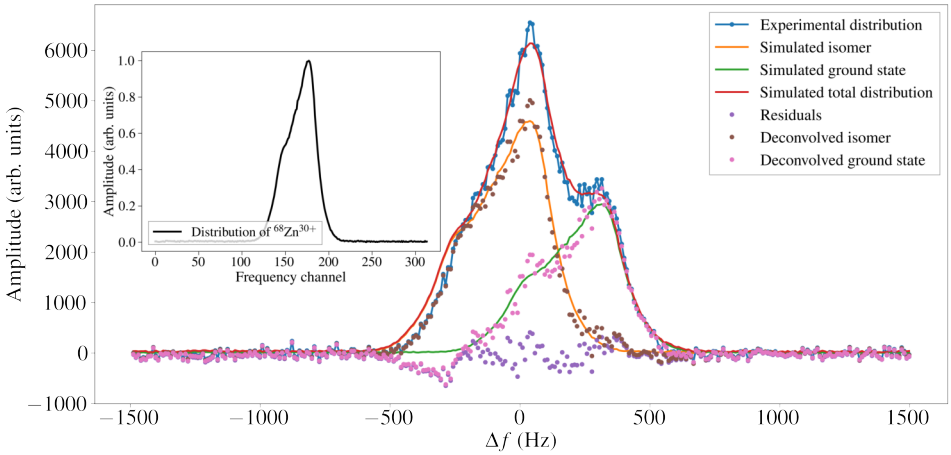

Figure 4.24. Simulated initial distributions of the isomeric and ground states of $^{77}Se^{34+}$, copying the shape observed in the inset, superimposed on the experimental data.

To implement the method outlined in App. C, we require a reference distribution, ideally from a neighboring non-contaminated nuclide, like $^{68}Zn^{30+}$. The normalized reference distribution is shown in the inset of Fig. 4.24. Additionally, Fig. 4.24 displays the overlay of the isomeric and ground state distributions, mirroring the reference's shape, and adjusted in position and scale to accurately replicate the total unresolved peak. These constitute the initial conditions for the minimization process described in App. C.

The **preliminarily**[5] obtained decay constant is $\tau^{\gamma}_{\text{lab}} \sim 56(10)$ s. After adjusting for the Lorentz factor $\gamma \sim 1.395$ and incorporating the α factor of $0.881(13)$ from [46], we calculate a rest-frame half-life, $T^{\text{rest}}_{1/2} \sim 15(3)$ s, which is within $< 1\sigma$ of the measured value. Similarly, assuming that the **preliminarily** measured $\tau^{\gamma}_{\text{lab}}$ is correct, we can deduce the α factor using Eq. (1.9), which results in $\alpha \sim 0.6(3)$. This straightforward case, where no decay mode mixing is observed, serves as a test reference, confirming the method's potential.

4.6.2.2 Bare ^{71m}Ge

^{71}Ge presents an isomer at $198.371(12)$ keV [134] and a half-life of $20.22(12)$ ms [134] in its neutral state, which decays to an intermediate state at $174.954(6)$ keV via an IT, involving a competition between an $M2$ photon decay and IC, with an electron conversion factor of $\alpha = 207.5(3)$ [134]. Subsequently, it decays to its ground state through an $E2$ transition with a half-life of $81(3)$ ns and with $\alpha = 0.0915(13)$ [134]. Given that our detectors lack the time resolution to discern transitions occurring on the scale of nanoseconds, the observed scenario is equivalent to the transition depicted in Fig. 4.23a, namely, a direct transition from the $198.371(12)$ keV state to the ground state.

We follow the same methodology as outlined in §4.6.2.1, but given the different mass-to-charge (m/q) region we are examining, the peak's distributions are very different. Therefore, a distinct reference than before, reflecting the deformation in this area is necessary. In this m/q region, the nearest non-contaminated nuclide is $^{61}Ni^{28+}$. As previously for ^{77m}Se, Fig. 4.25 presents the initial conditions for our minimization process. The **preliminarily**[6] obtained decay constant is $\tau^{\gamma}_{\text{lab}} \sim 14(1)$ s. After converting to half-life using the Lorentz factor $\gamma = 1.395$ and the α value $207.5(30)$ [46], we arrive at $T^{\text{rest}}_{1/2} \sim 33(2)$ ms. This value significantly diverges from the anticipated value of $20.22(12)$ ms. As in the previous case, by assuming that the **preliminarily** measured $\tau^{\gamma}_{\text{lab}}$ is correct, we can deduce the α factor using Eq. (1.9), which results in a **preliminary** $\alpha \sim 337(24)$. This discrepancy could be due to unconsidered multipole mixing, indicating that the transition is not purely $M2$ but may also contain elements of an $E3$ transition. Additionally,

[5] Please note that these results are currently being evaluated, and further analysis, especially regarding the uncertainties, is necessary.

[6] Please note that these results are currently being evaluated, and further analysis, especially regarding the uncertainties, is necessary.

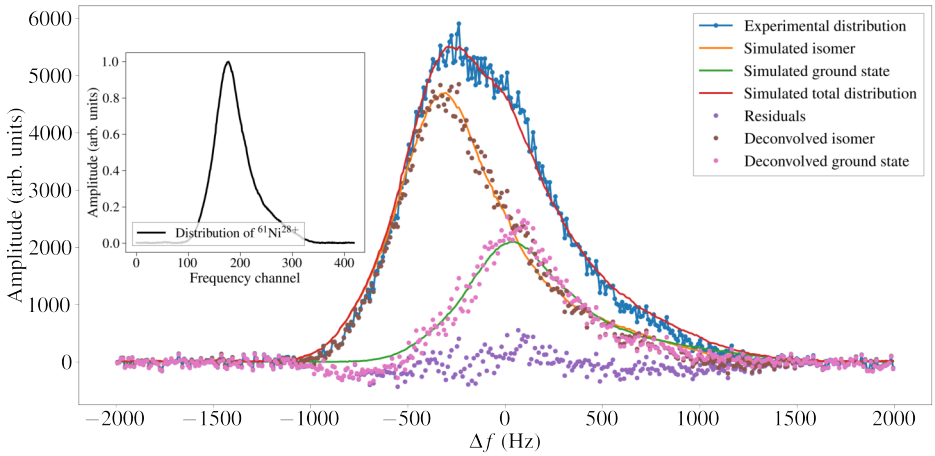

Figure 4.25. Simulated initial distributions of the isomeric and ground states of $^{71}Ge^{32+}$, copying the shape observed in the inset, superimposed on the experimental data.

it could be that some assumptions outlined in App. C are not fully satisfied for reasons that have yet to be identified. **Further analysis is required** to clarify these issues.

Table 4.8. The experimentally determined α factors (α_{exp}) for ^{77m}Se and ^{71m}Ge, compared with their theoretical values (α_{theo}).

ISOMER	ω (keV)	J^π	DECAY MODE	α_{theo}	α_{exp}
^{77m}Se	161.9223(10)	$7/2^+$	E3	0.881(13)	0.6(3)
^{71m}Ge	198.371(12)	$9/2^+$	M2	207.5(30)	337(24)

Chapter 5

Conclusions and Outlook

5.1 Conclusions

Parts of the text in this section have already been submitted for publication to Physical Review Letters in D. Freire-Fernandez et al., Measurement of the Isolated Nuclear Two-Photon Decay in ^{72}Ge (2024) [180].

SUMMARIZING, I reported the results of the combined **SCHOTTKY + ISOCHRONOUS MASS SPECTROMETRY (S+IMS)** applied to the direct determination of the excitation energy and partial half-life of an isomer in the millisecond regime with high precision. This represents a dramatic extension of the storage-ring based non-destructive lifetime spectroscopy to shorter-lived species as compared to previous experiments with electron-cooled stored beams [187]. A **mass resolving power** of $\mathbf{9.1 \times 10^5}$ (refer to §4.4) has been achieved, which allows us to fully resolve $\sim$ **100 keV** excited states, as was the case of ^{72m}**Br** (showed in §4.4). For the $\mathbf{2\gamma}$ **decay** of the 0^+ isomer in $^{\mathbf{72}}$**Ge**, a **partial half-life** of $\overline{T}^{\mathbf{rest}}_{\mathbf{1/2}} = \mathbf{23.9\ (6)}$ **ms** (§4.6.1) and an excitation energy of $\boldsymbol{\omega} = \mathbf{692.8\ (19)}$ **keV** (§4.5.1) have been determined. The obtained partial half-life is a **factor $\sim$ 10 shorter than expected** from the extrapolation of previous results based on doubly-magic ^{16}O, ^{40}Ca and semi-magic ^{90}Zr, indicating that the cancellation effect, which arises from the non-positive products among nuclear matrix elements (in Eq. (2.3) and Eq. (2.5)) observed in those nuclides, does not seem to occur.

Additionally, we presented the (**preliminary**) **most precise** mass measurements obtained at storage rings (refer to §4.5). Highlights include **consistently** achieving an **uncertainty** of approximately **10 keV**, the potential **improvement** of the mass uncertainty of $^{\mathbf{69}}$**As** by a third of the AME2020 value, and the observation of a **deviation** of about **30 keV** from the AME2020 value for $^{\mathbf{72}}$**As**. These **preliminary** results will be further discussed and published separately.

I also provided a mathematical (refer to App. B) and illustrative (refer to §4.2) example of **harmonic overlapping** within the recorded Schottky data. In order to address the potential **contamination** caused by overlapping signals, I have developed a **new** off-line analysis technique.

This method is designed for analyzing **unresolved** ions, enabling their precise mass and half-life measurements. In unresolved isomers, additionally, we could determine the isomeric ratio. Furthermore, the observation of **pure single-photon decay** in bare ions allows us to determine **electron conversion factors** experimentally. This would allow the comparison between experimental and, the usually tabulated, theoretical electron conversion factors. Hence, this method could act as a validation tool for theoretical calculations, where observed deviations might lead to **new assignments** of the specific transition **multipolarities**. These results are also still **preliminary** and under discussion.

Due to the excellent results given by our technique, S+IMS could be applied to a multitude of experiments at storage rings. Some have been outlined in the list provided in §5.2.

5.2 Potential experiments

In this section, I present a list of nuclides that could be investigated using our combined SCHOTTKY PLUS ISOCHRONOUS MASS SPECTROMETRY (Chap. 3). This section first examines potential candidates for nuclear two-photon decay (§5.2.1), followed by exploring the potential of our technique for searching undiscovered low-lying $E0$ (and $M0$) transitions (§5.2.2).

5.2.1 Further nuclear two-photon decay candidates

- ^{98}Mo is a stable nuclide with a ground state of $J^\pi = 0^+$ [188]. It is characterized by having a first excited state 0^+ at $734.75(4)$ keV and $T_{1/2} = 21.8(9)$ ns [188] making it an excellent candidate for measuring the (non-competitive[1]) nuclear two-photon decay. A measurement campaign in this nuclide is scheduled for May 2024, within the experiment E018 [189] at GSI.

- ^{98}Zr, with a ground state of $J^\pi = 0^+$ and a half-life of $30.7(4)$ s decaying primarily via β^- [188], contains a first excited state 0^+ at $854.06(6)$ keV and with $T_{1/2} = 64(7)$ ns [188]. These features qualify this nuclide as a promising candidate for measuring the (isolated) nuclear two-photon decay. In May 2024, experiment E018 [189] will be conducted, aiming to measure the nuclear two-photon decay in this nuclide.

- Nowadays, with the aid of high-resolution gamma spectrometers like AGATA [43], it may be possible to measure the (competitive) nuclear two-photon decay in ^{72}Ge, since its branching ratio is higher than expected: $T_{1/2}/T_{1/2}^{\gamma\gamma} \approx 2 \times 10^{-5}$ [180]. A successful measurement would offer additional insights into the magnitudes and signs of the nuclear

[1] Unlike gamma spectroscopy, which measures these tiny decay branches in competition with other decay processes (competitive), our technique (refer to §2.3) relies on prohibiting the other decay channels. In such cases, we exclusively observe the nuclear two-photon decay, making it non-competitive or isolated.

matrix elements in Eq. (2.2), allowing for a direct comparison between theoretical predictions and experimental data. Initial efforts in this direction have recently taken place at HIγS [190] and the University of Cologne.

- ^{72}Kr features both ground and first excited states with a $J^\pi = 0^+$ [191]. The excited state, situated at $671(1)$ keV and having a half-life of $26.3(21)$ ns [191], makes it an ideal candidate for the measurement of its (non-competitive) nuclear two-photon decay and exploring its shape-coexistence [192].

- ^{182}Hg features a 0^+ ground state and, potentially, a first excited state 0^+ at ~ 328 keV [193]. From the relation contained in Eq. (2.2) and illustrated in Fig. 2.4, we would expect an extremely hindered 2γ decay branch, making it unreachable by any other technique, but the one described in this thesis. This makes ^{182}Hg a perfect candidate for exploring the nuclear two-photon decay [193].

- ^{186}Pb stands out as potentially the only nuclide with its two first excited states and the ground state all being 0^+ [194]. Therefore, when fully stripped, our technique could uniquely enable the simultaneous measurement of two nuclear two-photon decays!

- ^{190}Pb presents a first excited state at $658(4)$ keV and a ground state, both 0^+ [195]. A $0^+ \rightarrow 0^+$ transition with a half-life of ≤ 0.22 ns has been observed in its neutral state [195]. Thus, in the absence of electrons, our approach could potentially enable observation of the nuclear two-photon decay.

- ^{192}Pb, possessing a first excited state at $768.84(23)$ keV [196] with $J^\pi = 0^+$, as its ground state, is another potential candidate for measuring the nuclear 2γ decay with bare ions stored in rings.

- ^{194}Pb is a special nucleus. It features a first excited 0^+ state at $930.70(21)$ keV, with the ground state also being a 0^+ state. This makes it a promising candidate for observing the nuclear two-photon decay. What elevates even more its uniqueness, is the potential to observe the bound-state electron-positron pair creation [197]. The underlying concept is that, although the excited state is below the pair-creation threshold, capturing an electron into the vacant atomic K-shell introduces an additional (atomic binding) energy of 101.3 keV to the reaction. Therefore, if the electron from the created pair is captured (bound), it would effectively increase the total energy available to $\approx 930.7 + 101.3 > 1022$ keV, thus enabling bound-state electron-positron pair creation.

5.2.2 Search for undiscovered low-lying $E0$ (and $M0$) transitions

This technique presents potential for discovering $E0$ (and $M0$) transitions that have eluded detection through conventional electron spectroscopy. By utilizing bare ions, some states can be prevented from decaying via their typical pathways, as introduced in §2.3 and proved in §4.6.1. Under these circumstances, the excited state is "trapped" for an extended duration, thereby facilitating its measurement. This approach could be applied to nuclei theoretically or empirically predicted to possess a first excited low-lying $J = 0$ state alongside a $J = 0$ ground state. An example of such an application was the search of such a state in ^{70}Se, where despite our efforts, no indications of such a state were observed.

5.3 Future facilities

Many of the nuclides listed in §5.2 for possible experiments are challenging to produce in sufficient quantities for measurement at existing facilities (refer to §1.2.0.2). However, by the end of this decade, two main heavy-ion research facilities are expected to come online: the FACILITY FOR ANTIPROTON AND ION RESEARCH (FAIR) (refer to [198]), and the HIGH INTENSITY HEAVY ION ACCELERATOR FACILITY (HIAF) [199]. These facilities are designed to achieve higher beam energies and intensities, among others, facilitating the production of (exotic) (heavy) neutron and proton-rich nuclides. Moreover, they are expected to be equipped with multiple storage rings specifically designed for operating the isochronous mode, unlike the present ones, and integrated with various Schottky detectors. These features make the novel methodology described in Chap. 3 particularly promising to be further developed and applied.

A. Derivation of the Peak Spreads in Storage Rings

The ratio of the velocity of relativistic ions to the speed of light in vacuum is defined as:

$$\beta = \frac{v}{c}, \tag{A.1}$$

where v is the velocity of the ions, and c is the speed of light.

The Lorentz factor, γ, is given by:

$$\gamma = \frac{1}{\sqrt{1-\beta^2}}. \tag{A.2}$$

The total energy of relativistic particles, U, is given as:

$$U = \gamma m c^2, \tag{A.3}$$

where m is the rest mass of the particle.

The momentum, p, of the particle is expressed as:

$$p = \beta\gamma m c = \beta\frac{U}{c}. \tag{A.4}$$

The kinetic energy, T, is calculated from:

$$T = (\gamma - 1)mc^2. \tag{A.5}$$

An alternative expression for the total energy in terms of rest mass and relativistic momentum is:

$$U = \sqrt{p^2 + m^2}. \tag{A.6}$$

Differentiating $U^2 = p^2c^2 + m^2c^4$ with respect to p gives:

$$2U\,dU = 2pc^2\,dp, \tag{A.7}$$

leading to the relation between differential changes in total energy and momentum as:

$$\frac{dU}{U} = \left(\frac{p}{U}\right)^2 \frac{dp}{p} = \beta^2\frac{dp}{p}. \tag{A.8}$$

The relation between a differential change in β and γ is:

$$d\gamma = -\frac{1}{2}\left(1-\beta^2\right)^{-\frac{3}{2}}(-2\beta)d\beta = \beta\gamma^3 d\beta, \tag{A.9}$$

therefore,

$$\frac{d\beta}{\beta} = \frac{d\gamma}{\gamma}\left(\frac{1}{\beta\gamma}\right)^2, \tag{A.10}$$

and, since $\frac{d\gamma}{\gamma} = \frac{dU}{U} = \beta^2\frac{dp}{p}$, we have:

$$\frac{d\beta}{\beta} = \frac{d\gamma}{\gamma}\left(\frac{1}{\beta\gamma}\right)^2 \implies \frac{d\beta}{\beta} = \frac{1}{\gamma^2}\frac{dp}{p}, \tag{A.11}$$

or equivalently:

$$\frac{\sigma_v}{v} = \frac{1}{\gamma^2}\frac{\sigma_p}{p}. \tag{A.12}$$

The differential time spread can be expressed in relation to the differential momentum as:

$$\frac{\sigma_T}{T} = \frac{\sigma_f}{f} = \left(1-\frac{\gamma^2}{\gamma_t^2}\right)\frac{\sigma_v}{v} = \left(\frac{1}{\gamma^2}-\frac{1}{\gamma_t^2}\right)\gamma^2\frac{\sigma_v}{v}, \tag{A.13}$$

which, using the equation referenced, relates to the momentum spread as:

$$\frac{\sigma_T}{T} = \left(\frac{1}{\gamma^2}-\frac{1}{\gamma_t^2}\right)\frac{\sigma_p}{p}. \tag{A.14}$$

Therefore, the time spread of the peaks that appears in the isochronicity curve is given by:

$$\sigma_T = \sqrt{\left(\left(1-\left(\frac{L}{T\cdot c}\right)^2-\frac{1}{\gamma_t^2}\right)\cdot\left(\frac{\sigma_p}{p}\right)\cdot T\right)^2+\sigma_{sys}^2}. \tag{A.15}$$

Here, σ_T represents the time spread, σ_p is the momentum spread, and other symbols have their previously defined meanings. Also we have substituted the velocity termn v inside the γ factor as $v = L/T$ where L is the average path taken by the particles in every turn. σ_T is the measured time spread which depends on the dynamic term plus the systematics.

$$\sigma_T^{\text{exp}} = \sqrt{\sigma_{\text{set}}^2+\sigma_{\text{sys}}^2}. \tag{A.16}$$

Experimentally, we can relate the frequency spread (σ_f) to the spread in time (σ_T) by:

$$\sigma_T = T\cdot\frac{\sigma_f}{f}. \tag{A.17}$$

By differentiating Eq. (A.17) we obtain the experimental uncertainty in the time spread related to the measured quantities:

$$\begin{aligned}\Delta\sigma_T &= \left|\frac{\partial\sigma_T}{\partial\sigma_f}\right|\Delta\sigma_f + \left|\frac{\partial\sigma_T}{\partial T}\right|\Delta T + \left|\frac{\partial\sigma_T}{\partial f}\right|\Delta f \\ &= \frac{T}{f}\Delta\sigma_f + \frac{\sigma_f}{f}\Delta T + \frac{\sigma_f T}{f^2}\Delta f \\ &= \frac{1}{f^2}\Delta\sigma_f + 2\frac{\sigma_f}{f^3}\Delta f.\end{aligned} \tag{A.18}$$

While, since $T = \frac{1}{f}$, its uncertainty ΔT is given by:

$$\Delta T = \left| \frac{\partial T}{\partial f} \right| \Delta f = \frac{1}{f^2} \Delta f. \tag{A.19}$$

Finally, taking into account the harmonics yields:

$$\Delta \sigma_T = \frac{h}{f^3} \left(\Delta \sigma_f f + 2 \sigma_f \Delta f \right), \tag{A.20}$$

$$\Delta T = \frac{h}{f^2} \Delta f. \tag{A.21}$$

B. Harmonic Overlap

To find a mathematical expression relating the frequency center f_c, the frequency span f_s, the harmonic number h, and the number of overlaps for a given harmonic n, we can analyze and simulate the scenario geometrically with rectangles.

Let's evaluate the different possibilities:

- if $i < h$:

$$i > \frac{h \cdot \left(f_c - \frac{f_s}{2}\right)}{f_c + \frac{f_s}{2}}, \tag{B.1}$$

- if $i > h$:

$$i < \frac{h \cdot \left(f_c + \frac{f_s}{2}\right)}{f_c - \frac{f_s}{2}}. \tag{B.2}$$

Therefore, the total number of overlaps for a given harmonic h is the sum of the count of integers i that satisfy these conditions (excluding $i = h$).

Thus, we can make a Python script for this purpose:

```python
def count_overlaps(f_c, f_s, h):
    lower_limit = h * (f_c - f_s / 2) / (f_c + f_s / 2)
    upper_limit = h * (f_c + f_s / 2) / (f_c - f_s / 2)

    lower_overlap_count = sum(1 for i in range(1, h) if i > lower_limit)
    upper_overlap_count = sum(1 for i in range(h + 1, int(upper_limit) + 1))

    return lower_overlap_count + upper_overlap_count
```

As a visual example with experimental data, let's consider:

- $f_c = 1.929406\,\text{MHz}$,
- $f_s = 73406\,\text{Hz}$.

Experimentally, f_c is the EIGENFREQUENCY center of the distribution of identified peaks (within the same harmonic) and f_s the span of it. For this set of values, we can run our Python script to find out how many overlaps we will expect in the range of frequencies measured by our detectors, let's say the 125^{th} and 210^{th}, in addition to the 5^{th} for showing that usually at lower harmonics we will not find any superposition:

```
N_overlaps = [count_overlaps(f_c, f_s, h = h) for h in [5, 125, 210]]
print(f'N_overlaps = {N_overlaps}')
# Output: N_overlaps = [0, 8, 15]
```

Visually we can extend this relation to any harmonic, supposing we have an infinite number, in Fig. 3.10 can be seen the evolution of the number of overlaps for the different harmonics.

Finally, in order to have visually a better feeling of what is happening, I have recreated the case by assuming rectangles of center f_c and span f_s for different harmonic ranges, see Fig. B.1. There, every time there is a superposition between 2 harmonics, the area under the overlap is fill with a light green color. If there is more than one superposition the are gets darker and darker. Therefore, when working at high harmonics we have to be extra careful in the identification. Even if we are, we may be unlucky at getting contaminated the only peak clearly visible in the data with the contributions from other harmonics that cannot be properly identified. In such a case, the only solution would be to remove the contaminants by the use of scrappers during the experimental beam time. Although, the contaminating signals can also be due to the noise. This signals usually repeat at a high frequency, meaning that it would be present at other frequency ranges and therefore, you can deconvolve the signal.

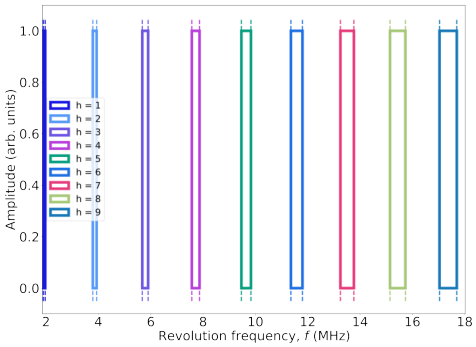

(a) Harmonic overlap between the first and ninth harmonic.

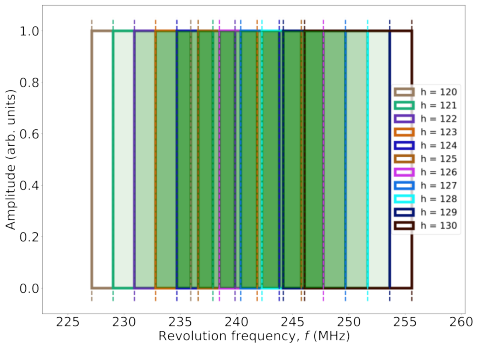

(b) Harmonic overlap between the 120^{th} and 130^{th} harmonic.

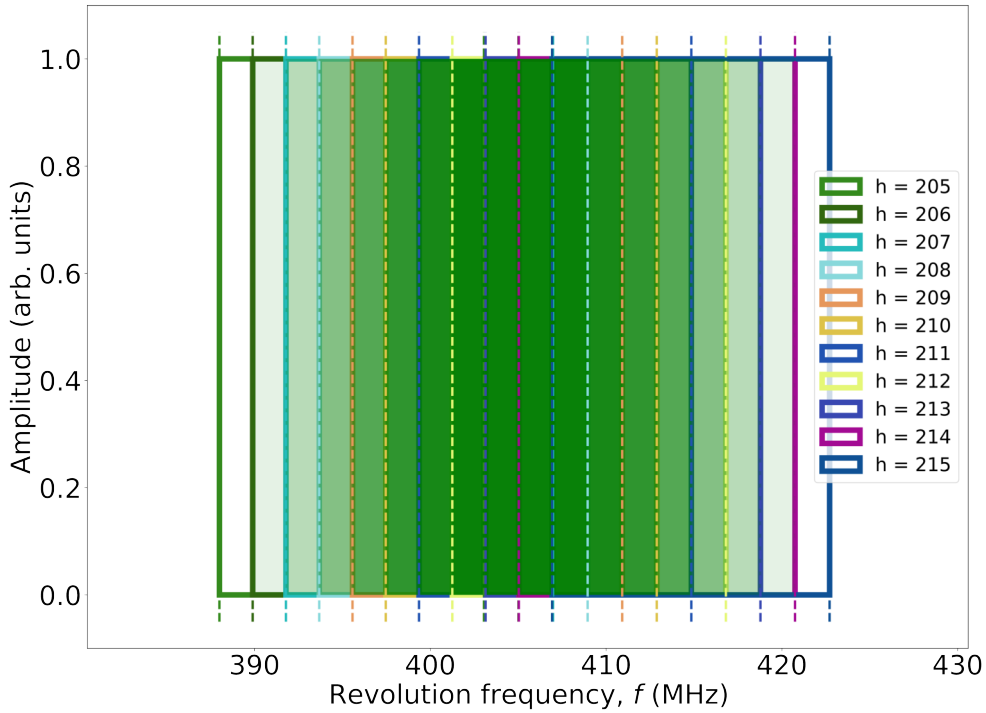

(c) Harmonic overlap between the 205^{th} and 215^{th} harmonic.

Figure B.1. Harmonic overlap for the different harmonics settings assuming there are only harmonics between them.

C. Peak Shape and Deconvolution of Isomers

The analysis of **peak shapes** in SCHOTTKY + ISOCHRONOUS MASS SPECTROMETRY (see Chap. 3) data reveals a one-to-one correlation with the mass-to-charge ratio (m/q) of the ions. This relationship allows for the identification of incorrect peak assignments and the presence of isomeric states (or contaminants), both characterized by deviations from the expected peak shape for a given m/q. Furthermore, this approach enables high-precision measurements of mass and half-life for unresolved isomers as I will demonstrate.

Initially, the goal is to define the probability distribution $f(m/q)$ that describes the peak's shape evolution across different m/q values. Given the complexity of directly solving this problem, we rely so far on "extrapolating" the shape of unresolved peaks to that of the nearest well-defined ion peak[1], by subtracting its distribution through interpolation. This CLEANED, normalized distribution is then used to model the shape of both the isomer and ground state[2], albeit at different scales and positions. The challenge lies in accurately determining these scales and positions through optimization techniques supported by various PYTHON libraries.

The optimization process requires a cost function to evaluate the accuracy of the model against experimental data, focusing on the peak's positions and their scaling. I assume that the isomer decays solely to the ground state following an exponential function and I also assume a stable ground state, in such a way that the number of ions under the ground state distribution should increase accordingly (see Eq. (C.2)). This allows us to link the scaling factors to this decay rate, thus simplifying the parameter space.

The peak's positions are determined by finding in the first and last time frame, the position that minimizes the cost function. These fix the position parameters (their masses) through the whole time. Similarly, the initial scales are fixed manually by finding the scaling factors minimizing the cost function.

This novel procedure extends our capability to analyze isomers beyond the ISOCHRONOUS WINDOW and refine peak contamination analysis within the ISOCHRONOUS WINDOW. It not only improves measurement uncertainties but also enables the determination of ISOMERIC RATIOS.

[1] A peak is considered well-defined if it exhibits a signal-to-noise ratio that clearly delineates the shape of the distribution and is free from contamination.

[2] For low-lying isomers we can assume that the isomer and ground state have the same shape.

The position of the peaks can be fixed easily, the challenge is to set the proper scale. We have one more ANSATZ, which is that we know that the isomer decays exponentially via photon emission to the ground state, at least in the isomers present in the data, and therefore the ground state increases its population accordingly (see Eq. (C.2)). In such a way that we can relate the scale to an exponential function and to the initial scale, for the isomer decaying and for the ground state increasing and with the same rate, thus reducing more the parameters needed. The initial scale can be determined by us by hand, since doing for one time frame (the first) is not so time demanding, and fed it into the minimization procedure, and apply it to the rest of frames, which can be hundreds. Therefore, with the minimization procedure we can find in each iteration the decay constant which make the peak distribution to "fit" (based on the cost function) the best the experimental peak. For the minimization we have used SCIPY-OPTIMIZE-DIFFERENTIAL-EVOLUTION, a PYTHON method from the library SCIPY [200]. If everything works, the average of the decay constant that reduced your cost function gives you the half-life of the isomeric state and the standard deviation of them, the error in your half-life. The energy is determined by the distance between both peaks. We this new procedure we can extend our analysis results to isomers far away from isochronicity and in addition, for the ones in the isochronous window if the had any contamination from the ground state which is very likely, this method can be applied to the case of one peak. In that case, it would be like the only thing in our data is that peak, no contamination, improving thus the uncertainties. It also allows us to determine the isomeric ratio.

The decay and growth of isomeric and (stable) ground states, respectively, can be mathematically expressed and related to the scaling parameters and decay constant as follows:

$$N\left(t\right)_{\text{iso}} = N\left(0\right)_{\text{iso}} \cdot exp\left(-\lambda_{\text{iso}} \cdot t\right), \tag{C.1}$$

$$N\left(t\right)_{\text{gs}} = N\left(0\right)_{\text{gs}} + N\left(0\right)_{\text{iso}} \cdot \left(1 - exp\left(-\lambda_{\text{iso}} \cdot t\right)\right), \tag{C.2}$$

$$N\left(0\right)_{\text{iso}} = S\left(0\right)_{\text{iso}} \cdot \sum PDF, \tag{C.3}$$

$$N\left(0\right)_{\text{gs}} = S\left(0\right)_{\text{gs}} \cdot \sum PDF, \tag{C.4}$$

$$N\left(t\right)_{\text{iso}} = S\left(0\right)_{\text{iso}} \cdot \sum PDF \cdot exp\left(-\lambda_{\text{iso}} \cdot t\right), \tag{C.5}$$

$$N\left(t\right)_{\text{gs}} = \left[S\left(0\right)_{\text{gs}} + S\left(0\right)_{\text{iso}} \cdot \left(1 - exp\left(-\lambda_{\text{iso}} \cdot t\right)\right)\right] \cdot \sum PDF, \tag{C.6}$$

where N is the number of ions of a specie, PDF is the probability density function which is given by the interpolated shape of reference, S is the scaling factor and λ_{iso} is the decay constant of the isomeric state.

These equations were implemented into the PYTHON methods below, where the scale at time TFRAME is computed and then the corresponding peaks' spectrograms to the isomer, ISO, and to the ground state, GS, are displaced to the proper position in the frequency axis by RI and RG respectively.

```
    def simulate_distribution(rates,tframe, ri, rg, scale_iso_0,
    ↪  scale_gs_0, PDF):
        scale_iso = np.exp(-rates[0] * tframe) * scale_iso_0
        scale_gs  = scale_gs_0 + scale_iso*(1-np.exp(-rates[0]*tframe))
        iso       = np.roll(PDF * scale_iso, ri)
        gs        = np.roll(PDF * scale_gs, rg)

        return iso + gs
```

```
    def cost_function(rates, tframe, ri, rg, experimental_distribution,
    ↪  scale_iso_0, scale_gs_0):
        simulated_distribution = simulate_distribution(rates, tframe,
        ↪  ri, rg, scale_iso_0, scale_gs_0)
        return np.average((experimental_distribution -
        ↪  simulated_distribution) ** 2)
```

D. Tables of Measured Data

Table D.1. Identified ions and their spectral characteristics from the second high-resolution setting optimized on $^{72}Ge^{32+}$ (I).

Ion	Harmonic	Revolution frequency (Hz)	Frequency spread (Hz)	Amplitude (arb. units)	Unresolved isomer
$^{71}Ga^{31+}$	127	242787896(15)	297(16)	86(3)	N
$^{48}Sc^{21+}$	127	243034987(24)	320(25)	67(4)	N
$^{64}Ni^{28+}$	127	243051471(8)	294(8)	236(6)	N
$^{73}Ge^{32+}$	127	243289249(5)	346(5)	1321(16)	Y
$^{57}Mn^{25+}$	127	243363087(6)	256(6)	444(9)	N
$^{41}Ar^{18+}$	127	243459012(15)	258(16)	160(8)	N
$^{66}Cu^{29+}$	127	243592265(3)	233(3)	2459(24)	N
$^{75}Se^{33+}$	127	243760902(4)	213(4)	2293(36)	N
$^{75}As^{33+}$	127	243762443(3)	205(3)	12118(155)	Y
$^{50}Ti^{22+}$	127	243769910(5)	234(5)	485(8)	N
$^{59}Fe^{26+}$	126	242043464(6)	184(6)	134(4)	N
$^{68}Zn^{30+}$	126	242185266(2)	168(3)	1116(14)	N
$^{77}Br^{34+}$	126	242283066(2)	169(2)	6801(64)	Y
$^{77}Se^{34+}$	126	242285300(3)	224(3)	2155(25)	Y
$^{43}K^{19+}$	126	242355225(8)	143(8)	89(4)	N
$^{52}V^{23+}$	126	242500462(2)	117(3)	196(5)	N
$^{61}Co^{27+}$	126	242595198(1)	100(1)	1579(15)	N
$^{70}Ga^{31+}$	126	242655062(1)	92(1)	11336(88)	N
$^{70}Ge^{31+}$	126	242658251(1)	90(1)	721(9)	N
$^{72}As^{32+}$	126	243097181(0.5)	58.9(0.4)	3380(22)	N
$^{72}Ge^{32+}$	126	243105253.5(0.4)	58.2(0.4)	170727(1070)	N
$^{63}Ni^{28+}$	126	243109532.5(0.5)	58.71(0.49)	15647(115)	N
$^{54}Cr^{24+}$	126	243111488.76(0.49)	58.36(0.48)	4527(33)	N
$^{74}As^{33+}$	126	243519180(1)	86(1)	353550(3008)	N
$^{74}Se^{33+}$	126	243521655(1)	91(1)	7044(69)	N
$^{65}Zn^{29+}$	126	243584870(3)	93(3)	686(16)	N
$^{65}Cu^{29+}$	126	243587634(1)	95(1)	45712(415)	N
$^{56}Mn^{25+}$	126	243661866(1)	102(1)	7827(75)	N
$^{47}Sc^{21+}$	126	243758076(1)	116(1)	2673(25)	N
$^{38}Cl^{17+}$	126	243892726(3)	134(3)	419(8)	N
$^{76}Se^{34+}$	126	243920211(2)	139(2)	153617(1486)	N

Table D.2. Identified ions and their spectral characteristics from the second high-resolution setting optimized on $^{72}Ge^{32+}$ (II).

Ion	Harmonic	Revolution frequency (Hz)	Frequency spread (Hz)	Amplitude (arb. units)	Unresolved isomer
$^{67}Ga^{30+}$	126	244030523(5)	138(5)	245(7)	N
$^{67}Zn^{30+}$	126	244032491(1)	149(1)	22886(173)	N
$^{58}Fe^{26+}$	126	244183201(1)	169(2)	3283(27)	N
$^{49}Ti^{22+}$	126	244367416(2)	197(2)	661(6)	N
$^{69}Ga^{31+}$	126	244451027(2)	206(2)	9458(72)	N
$^{40}Ar^{18+}$	126	244634011(8)	253(9)	107(3)	N
$^{60}Co^{27+}$	125	242712480(2)	240(2)	2267(16)	Y
$^{71}Ge^{32+}$	125	242899251(2)	309(2)	7059(39)	Y
$^{51}V^{23+}$	125	242979828(3)	265(3)	1464(13)	N
$^{62}Ni^{28+}$	125	243159130(2)	297(2)	9186(62)	N
$^{73}As^{33+}$	125	243265561(4)	333(4)	990(10)	Y
$^{42}K^{19+}$	125	243335898(4)	321(4)	830(9)	N
$^{53}Cr^{24+}$	125	243485373(2)	338(3)	3984(30)	N
$^{64}Cu^{29+}$	125	243562476(3)	354(3)	10457(77)	N
$^{33}P^{15+}$	125	243916763(12)	358(14)	174(5)	N
$^{44}Ca^{20+}$	125	243935785(4)	401(4)	788(7)	N
$^{66}Zn^{30+}$	125	243948979(4)	203(5)	1506(36)	N*
$^{55}Mn^{25+}$	125	243949584(5)	612(4)	3669(19)	N*
$^{68}Ga^{31+}$	125	244301175(10)	457(10)	169(3)	N
$^{57}Fe^{26+}$	125	244379484(4)	460(5)	749(6)	N
$^{46}Sc^{21+}$	125	244462245(7)	505(7)	254(3)	N
$^{59}Co^{27+}$	124	242818854(5)	504(6)	766(7)	N
$^{48}Ti^{22+}$	124	242999817(5)	546(6)	689(6)	N
$^{61}Cu^{28+}$	124	243181008(18)	600(26)	177(5)	N
$^{61}Ni^{28+}$	124	243185522(7)	551(7)	699(7)	N
$^{37}Cl^{17+}$	125	245238819(43)	567(47)	27(2)	N
$^{50}V^{23+}$	124	243435438(5)	633(5)	1492(10)	N
$^{63}Cu^{29+}$	125	245489985(100)	709(109)	13(2)	N
$^{39}Ar^{18+}$	124	243821322(11)	696(11)	328(5)	N
$^{52}Cr^{24+}$	124	243849050(6)	685(6)	794(6)	N
$^{54}Mn^{25+}$	124	244215705(13)	706(33)	162(3)	N
$^{41}K^{19+}$	124	244312145(18)	756(20)	102(2)	N
$^{56}Fe^{26+}$	124	244565855(45)	741(49)	34(2)	N
$^{43}Ca^{20+}$	124	244756319(32)	880(34)	50(2)	N
$^{30}Si^{14+}$	123	243168603(32)	880(35)	97(3)	N
$^{45}Sc^{21+}$	124	245158306(61)	984(66)	25(1)	Y
$^{47}Ti^{22+}$	123	243547435(23)	905(24)	214(5)	N
$^{32}P^{15+}$	123	243690848(41)	1009(44)	110(4)	N
$^{34}S^{16+}$	123	244170003(66)	950(95)	51(4)	N
$^{76}Kr^{36+}$	122	242959092(48)	1151(54)	62(2)	N

* They do not possess an unresolved isomer, however they are overlapped with each other due to their close mass-to-charge ratios. In the first data set they are completely unresolvable.

Table D.3. Identified ions and their spectral characteristics from the first high-resolution setting optimized on $^{72}Ge^{32+}$ (I).

Ion	Harmonic	Revolution frequency (Hz)	Frequency spread (Hz)	Amplitude (arb. units)	Unresolved isomer
$^{71}Ga^{31+}$	127	242788226(29)	607(32)	14(1)	N
$^{48}Sc^{21+}$	127	243035180(49)	696(54)	10(1)	N
$^{64}Ni^{28+}$	127	243051745(14)	554(15)	35(1)	N
$^{73}Ge^{32+}$	127	243289466(6)	535(6)	230(2)	Y
$^{57}Mn^{25+}$	127	243363270(11)	458(12)	66(1)	N
$^{41}Ar^{18+}$	127	243459204(31)	463(33)	23(1)	N
$^{66}Cu^{29+}$	127	243592450(5)	413(6)	391(4)	N
$^{75}Se^{33+}$	127	243761099(19)	404(28)	365(24)	N
$^{75}As^{33+}$	127	243762629(6)	348(6)	1938(28)	Y
$^{50}Ti^{22+}$	127	243770070(7)	354(7)	81(1)	N
$^{59}Fe^{26+}$	126	242043627(16)	363(20)	23(1)	N
$^{68}Zn^{30+}$	127	244107459(7)	287(8)	743(16)	N
$^{77}Br^{34+}$	127	244206032(5)	259(6)	3476(60)	Y
$^{77}Se^{34+}$	127	244208282(4)	298(5)	1221(14)	Y
$^{43}K^{19+}$	127	244278732(11)	243(12)	31(1)	N
$^{52}V^{23+}$	127	244425118(6)	197(7)	58(2)	N
$^{61}Co^{27+}$	127	244520592(5)	166(5)	248(6)	N
$^{70}Ga^{31+}$	126	242655155(4)	148(4)	1833(41)	N
$^{70}Ge^{31+}$	126	242658347(4)	139(4)	112(3)	N
$^{72}As^{32+}$	126	243097224(1)	77(1)	669(6)	N
$^{72}Ge^{32+}$	126	243105292(1)	75(1)	33444(265)	N
$^{63}Ni^{28+}$	126	243109571(1)	75(1)	3247(28)	N
$^{54}Cr^{24+}$	126	243111527(1)	76(1)	892(7)	N
$^{74}As^{33+}$	126	243519182(1)	98(1)	74655(450)	N
$^{74}Se^{33+}$	126	243521659(1)	101(1)	1376(17)	N
$^{65}Zn^{29+}$	126	243584823(3)	123(3)	162(3)	N
$^{65}Cu^{29+}$	126	243587629(2)	111(2)	9584(115)	N
$^{56}Mn^{25+}$	126	243661857(2)	128(2)	1604(20)	N
$^{47}Sc^{21+}$	126	243758052(2)	146(2)	538(7)	N
$^{38}Cl^{17+}$	126	243892686(4)	169(5)	89(2)	N
$^{76}Se^{34+}$	126	243920194(2)	193(2)	15583(214)	N
$^{67}Ga^{30+}$	126	244030478(7)	187(8)	40(1)	N
$^{67}Zn^{30+}$	126	244032448(2)	220(2)	4148(25)	N
$^{58}Fe^{26+}$	126	244183151(2)	264(2)	570(3)	N
$^{49}Ti^{22+}$	126	244367341(3)	318(3)	117(1)	N
$^{69}Ga^{31+}$	126	244450958(2)	342(2)	1540(7)	N
$^{40}Ar^{18+}$	126	244633879(12)	351(13)	20(1)	N
$^{60}Co^{27+}$	125	242712402(2)	405(3)	368(2)	Y
$^{71}Ge^{32+}$	125	242899162(2)	470(2)	1167(4)	Y

Table D.4. Identified ions and their spectral characteristics from the first high-resolution setting optimized on $^{72}Ge^{32+}$ (II).

Ion	Harmonic	Revolution frequency (Hz)	Frequency spread (Hz)	Amplitude (arb. units)	Unresolved isomer
$^{51}V^{23+}$	126	244923519(6)	483(6)	53(1)	N
$^{62}Ni^{28+}$	125	243159014(2)	518(2)	1420(5)	N
$^{73}As^{33+}$	125	243265506(7)	579(7)	143(1)	Y
$^{42}K^{19+}$	125	243335748(11)	639(12)	123(2)	N
$^{53}Cr^{24+}$	125	243485233(3)	624(4)	616(3)	N
$^{64}Cu^{29+}$	125	243562340(3)	632(4)	1662(7)	N
$^{33}P^{15+}$	125	243916608(24)	657(29)	27(1)	N
$^{44}Ca^{20+}$	125	243935621(6)	741(7)	133(1)	N
$^{68}Ga^{31+}$	124	242346686(34)	812(40)	11(1)	N
$^{57}Fe^{26+}$	125	244379274(6)	887(7)	116(1)	N
$^{46}Sc^{21+}$	125	244462013(12)	941(14)	40(1)	N
$^{59}Co^{27+}$	124	242818607(9)	1025(15)	117(1)	N
$^{48}Ti^{22+}$	124	242999564(8)	1062(9)	109(1)	N
$^{61}Cu^{28+}$	125	245146264(30)	1218(33)	14(1)	N
$^{61}Ni^{28+}$	124	243185262(12)	1043(14)	98(1)	N
$^{37}Cl^{17+}$	124	243276645(22)	1145(25)	46(1)	N
$^{50}V^{23+}$	124	243435134(8)	1159(9)	232(1)	N
$^{63}Cu^{29+}$	124	243525835(56)	1175(72)	29(1)	N
$^{39}Ar^{18+}$	124	243821075(22)	1343(24)	50(1)	N
$^{52}Cr^{24+}$	124	243848686(10)	1286(11)	127(1)	N
$^{54}Mn^{25+}$	124	244215249(24)	1380(27)	26(1)	N
$^{41}K^{19+}$	124	244311762(36)	1451(41)	17(1)	N
$^{56}Fe^{26+}$	124	244565163(124)	1252(136)	4(1)	N
$^{43}Ca^{20+}$	124	244755850(59)	1557(67)	8(1)	N
$^{30}Si^{14+}$	123	243168063(57)	1418(64)	16(1)	N
$^{45}Sc^{21+}$	123	243180688(47)	1661(81)	36(2)	Y
$^{47}Ti^{22+}$	123	243546842(45)	1781(52)	37(1)	N
$^{32}P^{15+}$	123	243690222(76)	1785(90)	19(1)	N
$^{34}S^{16+}$	123	244169703(91)	1912(108)	9(1)	N

Table D.5. Identified ions and their spectral characteristics from the first high-resolution setting optimized on $^{70}Se^{34+}$ (May).

Ion	Harmonic	Revolution frequency (Hz)	Frequency spread (Hz)	Amplitude (arb. units)	Unresolved isomer
$^{45}Sc^{21+}$	129	243905986(34)	587(40)	9.2(0.5)	Y
$^{47}Ti^{22+}$	129	244306086(19)	391(20)	9(0.4)	N
$^{32}P^{15+}$	129	244462993(43)	307(46)	2.7(0.3)	N
$^{49}V^{23+}$	128	242773153(6)	273(7)	21.4(0.4)	N
$^{34}S^{16+}$	128	243087999(12)	253(13)	16.6(0.7)	N
$^{51}Cr^{24+}$	128	243105715(3)	224(4)	81(1)	N
$^{53}Mn^{25+}$	128	243411462(3)	189(4)	258(4)	N
$^{36}Cl^{17+}$	128	243524805(5)	183(5)	65(1)	N
$^{55}Fe^{26+}$	128	243692929(3)	165(3)	77(2)	N
$^{38}Ar^{18+}$	128	243934065(4)	155(4)	56(1)	N
$^{57}Co^{27+}$	128	243951600(3)	178(3)	277(4)	N
$^{59}Ni^{28+}$	128	244191931(3)	194(3)	179(2)	N
$^{40}K^{19+}$	128	244278969(5)	221(6)	27.2(0.6)	N
$^{61}Cu^{29+}$	128	244413715(2)	232(3)	113(1)	N
$^{42}Ca^{20+}$	128	244610087(8)	291(8)	18.5(0.4)	N
$^{63}Zn^{30+}$	128	244619607(3)	280(3)	100.1(0.9)	N
$^{65}Ga^{31+}$	128	244812844(3)	332(3)	67(0.6)	N
$^{67}Ge^{32+}$	127	243079284(3)	365(3)	360(3)	Y
$^{69}As^{33+}$	127	243248450(3)	406(4)	556(4)	N
$^{46}Ti^{22+}$	127	243254557(4)	388(4)	146(1)	N
$^{71}Se^{34+}$	127	243406953(4)	456(4)	937(7)	Y
$^{48}V^{23+}$	127	243489584(4)	493(4)	235(2)	N
$^{73}Br^{35+}$	127	243557353(4)	485(4)	1065(7)	Y
$^{75}Kr^{36+}$	127	243699863(3)	556(3)	1380(6)	N
$^{50}Cr^{24+}$	127	243720022(4)	535(6)	268(2)	N
$^{77}Rb^{37+}$	127	243834444(5)	559(5)	388(3)	N
$^{52}Mn^{25+}$	127	243918202(4)	656(5)	177(1)	Y
$^{27}Al^{13+}$	127	244059198(24)	654(26)	10(0.3)	N
$^{54}Fe^{26+}$	127	244114259(5)	650(5)	155(1)	N
$^{56}Co^{27+}$	126	242358419(7)	666(8)	56(0.5)	N
$^{29}Si^{14+}$	127	244409561(60)	749(68)	3.4(0.2)	N
$^{58}Ni^{28+}$	127	244448008(5)	734(6)	93(1)	N
$^{60}Cu^{29+}$	127	244589000(6)	774(7)	65.8(0.5)	N
$^{62}Zn^{30+}$	126	242804012(6)	810(6)	143.7(0.9)	N
$^{64}Ga^{31+}$	126	242925051(6)	828(6)	158.2(0.9)	Y
$^{33}S^{16+}$	126	243031827(28)	775(29)	10.3(0.3)	N
$^{66}Ge^{32+}$	126	243048970(5)	860(6)	262(5)	N
$^{68}As^{33+}$	126	243154647(5)	915(6)	266(1)	N
$^{70}Se^{34+}$	126	243265120(6)	937(6)	406(2)	N

Table D.6. Identified ions and their spectral characteristics from the first high-resolution setting optimized on $^{70}Se^{34+}$ (May).

Ion	Harmonic	Revolution frequency (Hz)	Frequency spread (Hz)	Amplitude (arb. units)	Unresolved isomer
$^{72}Br^{35+}$	126	243358287(8)	990(9)	274(2)	Y
$^{74}Kr^{36+}$	126	243457511(7)	1045(8)	230(1)	N
$^{39}K^{19+}$	126	243638241(18)	997(21)	35(0.5)	N
$^{43}Sc^{21+}$	126	243939329(24)	1003(27)	22.3(0.5)	Y
$^{45}Ti^{22+}$	126	244074249(21)	1086(23)	20.7(0.3)	Y
$^{47}V^{23+}$	126	244197942(26)	1043(29)	13.9(0.3)	N
$^{49}Cr^{24+}$	126	244312448(21)	1199(25)	15.3(0.2)	N
$^{53}Fe^{26+}$	126	244512448(36)	1276(42)	8.1(0.2)	N
$^{55}Co^{27+}$	126	244601974(33)	1332(39)	8.3(0.2)	N
$^{57}Ni^{28+}$	125	242740982(33)	1368(38)	9.9(0.2)	N
$^{59}Cu^{29+}$	126	244753886(62)	1163(69)	3.5(0.2)	N
$^{61}Zn^{30+}$	125	242877123(54)	1385(62)	6.5(0.2)	N
$^{63}Ga^{31+}$	125	242938447(78)	1247(89)	4.5(0.2)	N

Table D.7. Identified ions and their spectral characteristics from the first high-resolution setting optimized on $^{70}Se^{34+}$ (June).

Ion	Harmonic	Revolution frequency (Hz)	Frequency spread (Hz)	Amplitude (arb. units)	Unresolved isomer
$^{56}Co^{27+}$	127	243892704(15)	143(16)	7990(739)	N
$^{58}Ni^{28+}$	127	244059164(11)	137(11)	13517(966)	N
$^{60}Cu^{29+}$	127	244200468(10)	116(10)	17204(1101)	N
$^{62}Zn^{30+}$	127	244342745(5)	97(6)	33342(1641)	N
$^{64}Ga^{31+}$	127	244464984(5)	88(6)	34683(1944)	Y
$^{66}Ge^{32+}$	127	244590137(3)	84(4)	58145(2108)	N
$^{68}As^{33+}$	127	244696837(3)	80(3)	59840(2013)	N
$^{70}Se^{34+}$	127	244808427(3)	87(3)	60089(1888)	N
$^{72}Br^{35+}$	127	244902584(9)	85(10)	31000(1848)	Y
$^{74}Kr^{36+}$	127	245002779(2)	72(3)	52910(1557)	N
$^{49}Cr^{24+}$	126	243930465(23)	113(24)	4936(869)	N
$^{53}Fe^{26+}$	126	244130861(26)	165(27)	6267(875)	N
$^{55}Co^{27+}$	126	244221002(23)	138(27)	8045(1192)	N
$^{57}Ni^{28+}$	126	244301627(19)	146(20)	10311(1198)	N
$^{59}Cu^{29+}$	126	244373018(23)	156(24)	9302(1252)	N

Table D.8. Isomers identified in the $^{70}Se^{34+}$ data sets, along with their nuclear properties [134].

Isomer	Energy (keV)	J^π	$T_{1/2}$	α
$^{45m}Sc^{21+}$	12.40(5)	$3/2^+$	325.8(42) ms	423(9)
$^{67m}Ge^{32+}$	18.20(5)	$5/2^-$	13.7(9) μs	364
$^{71m}Se^{34+}$	48.78(5)	$(1/2^-)$	5.6(7) μs	11.86
$^{73m}Br^{35+}$	26.92(9)	$(5/2)^-$	x	100.5(20)
$^{52m}Mn^{25+}$	377.749(5)	2^+	21.1(2) min	0.0399
$^{64m}Ga^{31+}$	42.86(8)	(2^+)	21.9(7) μs	16.23(27)
$^{72m}Br^{35+}$	100.76(15)	(3^-)	10.6(3) s	1.145(21)
$^{43m}Sc^{21+}$	151.79(8)	$3/2^+$	438(7) μs	0.0406
$^{45m}Ti^{22+}$	36.53(15)	$3/2^-$	3.0(2) μs	6.6(5)

[x] Not measured.

Table D.9. Isomers identified in the $^{72}Ge^{32+}$ data sets, along with their nuclear properties [134].

Isomer	Energy (keV)	J^π	$T_{1/2}$	α
$^{73m}Ge^{32+}$	13.2845(15)	$5/2^+$	2.91(3) μs	1063
$^{73m}Ge^{32+}$	66.725(9)	$1/2^-$	0.499(11) s	8.42
$^{75m}As^{33+}$	303.9243(8)	$9/2^+$	17.62(23) ms	205(5)
$^{77m}Br^{34+}$	105.86(8)	$9/2^+$	4.28(10) min	6.3
$^{77m}Se^{34+}$	161.9223(10)	$7/2^+$	17.36(5) s	0.881
$^{60m}Co^{27+}$	58.59(1)	2^+	10.467(6) min	47.3
$^{71m}Ge^{32+}$	198.371(12)	$9/2^+$	20.22(12) ms	207.5(30)
$^{73m}As^{33+}$	427.902(21)	$9/2^+$	5.7(2) μs	0.01315
$^{45m}Sc^{21+}$	12.40(5)	$3/2^+$	325.8(42) ms	423(9)

Table D.10. Results of the mass measurement of the $^{70}Se^{34+}$ data set from June.

Ion	Reference	T (ns)	$\Delta M_{\mathrm{exp}} - \Delta M_{\mathrm{AME}}$ (keV)	ΔM_{exp} (keV)	$\sigma_{\Delta M_{\mathrm{exp}}}$ (keV)	$\sigma_{\Delta M_{\mathrm{AME}}}$ (keV)
$^{59}Cu^{29+}$	Y	515.605	−2.493	−56360.947	15.249	0.528
$^{57}Ni^{28+}$	Y	515.756	0.164	−56083.797	10.884	0.566
$^{53}Fe^{26+}$	Y	516.117	1.737	−50945.745	12.140	1.669
$^{49}Cr^{24+}$	Y	516.541	1.824	−45330.528	12.085	2.202
$^{74}Kr^{36+}$	Y	518.361	−0.205	−62332.049	3.138	2.013
$^{72}Br^{35+}$	Y	518.574	2.180	−59059.570	5.006	1.025
$^{70}Se^{34+}$	Y	518.773	−1.722	−61931.622	2.130	1.584
$^{68}As^{33+}$	Y	519.010	0.502	−58894.025	2.007	1.846
$^{66}Ge^{32+}$	Y	519.236	0.710	−61606.331	1.971	2.401
$^{64}Ga^{31+}$	Y	519.502	1.576	−58831.251	2.823	1.429
$^{62}Zn^{30+}$	Y	519.762	−0.939	−61169.027	3.070	0.615
$^{60}Cu^{29+}$	Y	520.065	2.654	−58342.608	4.852	1.613
$^{58}Ni^{28+}$	Y	520.366	−7.928	−60236.799	5.622	0.349
$^{56}Co^{27+}$	Y	520.721	13.700	−56026.818	10.993	0.475

Table D.11. Results of the isochronicity curve of the $^{70}Se^{34+}$ data set from June.

Ion	σ_T (ps)	δ_{σ_T} (ps)	$\delta_{\sigma_{\mathrm{sys}}}$ (ps)
$^{59}Cu^{29+}$	0.329	0.051	0.006
$^{57}Ni^{28+}$	0.308	0.042	0.006
$^{53}Fe^{26+}$	0.349	0.057	0.006
$^{49}Cr^{24+}$	0.239	0.051	0.006
$^{74}Kr^{36+}$	0.152	0.006	0.006
$^{72}Br^{35+}$	0.180	0.021	0.006
$^{70}Se^{34+}$	0.184	0.006	0.006
$^{68}As^{33+}$	0.170	0.006	0.006
$^{66}Ge^{32+}$	0.178	0.008	0.006
$^{64}Ga^{31+}$	0.187	0.013	0.006
$^{62}Zn^{30+}$	0.206	0.013	0.006
$^{60}Cu^{29+}$	0.247	0.021	0.006
$^{58}Ni^{28+}$	0.292	0.023	0.006
$^{56}Co^{27+}$	0.305	0.034	0.006

Table D.12. Results of the mass measurement of the $^{70}Se^{34+}$ data set from May.

Ion	Reference	T (ns)	$\Delta M_{\mathrm{exp}} - \Delta M_{\mathrm{AME}}$ (keV)	ΔM_{exp} (keV)	$\sigma_{\Delta M_{\mathrm{exp}}}$ (keV)	$\sigma_{\Delta M_{\mathrm{AME}}}$ (keV)	$\sigma_{\Delta M_{\mathrm{sys}}}$ (keV)
$^{70}Se^{34+}$	Y	517.953	−10.996	−61940.896	5.824	1.584	8.730
$^{68}As^{33+}$	Y	518.189	−16.470	−58910.997	4.941	1.846	8.730
$^{66}Ge^{32+}$	Y	518.414	2.368	−61604.673	4.657	2.401	8.730
$^{62}Zn^{30+}$	Y	518.937	2.582	−61165.506	4.338	0.615	8.730
$^{74}Kr^{36+}$	Y	517.544	9.160	−62322.684	7.627	2.013	8.730
$^{39}K^{19+}$	Y	517.160	14.900	−33792.296	6.724	0.005	8.730
$^{45}Ti^{22+}$	Y	516.236	3.803	−39006.463	13.805	0.836	8.730
$^{49}Cr^{24+}$	Y	515.733	−12.148	−45344.500	24.670	2.202	8.730
$^{60}Cu^{29+}$	Y	519.238	22.375	−58322.887	3.752	1.613	8.730
$^{58}Ni^{28+}$	Y	519.538	0.978	−60227.893	3.528	0.349	8.730
$^{56}Co^{27+}$	Y	519.891	9.674	−56030.844	3.747	0.475	8.730
$^{54}Fe^{26+}$	Y	520.248	−3.742	−56258.357	2.996	0.343	8.730
$^{77}Rb^{37+}$	Y	520.845	15.435	−64815.065	4.018	1.304	8.730
$^{50}Cr^{24+}$	Y	521.089	−10.643	−50272.007	2.333	0.094	8.730
$^{75}Kr^{36+}$	Y	521.133	14.609	−64309.023	3.214	8.104	8.730
$^{73}Br^{35+}$	Y	521.438	19.389	−63626.398	3.401	6.741	8.730
$^{48}V^{23+}$	Y	521.583	−4.908	−44482.913	2.300	0.972	8.730
$^{71}Se^{34+}$	Y	521.760	−3.666	−63150.181	3.356	2.794	8.730
$^{46}Ti^{22+}$	Y	522.087	−6.501	−44134.770	2.157	0.09	8.730
$^{67}Ge^{32+}$	Y	522.463	−4.141	−62677.859	2.723	4.319	8.730
$^{65}Ga^{31+}$	Y	522.848	4.674	−62652.812	2.659	0.791	8.730
$^{63}Zn^{30+}$	Y	523.261	4.936	−62208.493	2.396	1.560	8.730
$^{61}Cu^{29+}$	Y	523.702	4.602	−61979.461	2.139	0.951	8.730
$^{59}Ni^{28+}$	Y	524.178	4.102	−61152.731	2.335	0.351	8.730
$^{57}Co^{27+}$	Y	524.694	−3.919	−59349.577	2.421	0.516	8.730
$^{38}Ar^{18+}$	Y	524.732	−1.590	−34716.417	1.743	0.195	8.730
$^{36}Cl^{17+}$	Y	525.614	−2.171	−29524.179	1.886	0.036	8.730
$^{53}Mn^{25+}$	Y	525.859	−3.541	−54693.891	2.511	0.346	8.730
$^{51}Cr^{24+}$	Y	526.520	3.755	−51446.96	3.526	0.167	8.730
$^{49}V^{23+}$	Y	527.241	0.995	−47961.162	7.193	0.824	8.730
$^{69}As^{33+}$	N	522.100	**-18.231**	−63130.412	**2.822**	**31.999**	**8.730**

Table D.13. Results of the isochronicity curve of the $^{70}Se^{34+}$ data set from May.

Ion	σ_T (ps)	δ_{σ_T} (ps)	$\delta_{\sigma_{\mathrm{sys}}}$ (ps)
$^{70}Se^{34+}$	1.995	0.013	0.040
$^{68}As^{33+}$	1.950	0.013	0.040
$^{66}Ge^{32+}$	1.834	0.013	0.040
$^{62}Zn^{30+}$	1.731	0.013	0.040
$^{74}Kr^{36+}$	2.221	0.017	0.040
$^{39}K^{19+}$	2.116	0.045	0.040
$^{45}Ti^{22+}$	2.297	0.049	0.040
$^{49}Cr^{24+}$	2.531	0.053	0.040
$^{60}Cu^{29+}$	1.643	0.015	0.040
$^{58}Ni^{28+}$	1.560	0.013	0.040
$^{56}Co^{27+}$	1.429	0.017	0.040
$^{54}Fe^{26+}$	1.385	0.011	0.040
$^{77}Rb^{37+}$	1.194	0.011	0.040
$^{50}Cr^{24+}$	1.144	0.013	0.040
$^{75}Kr^{36+}$	1.189	0.007	0.040
$^{73}Br^{35+}$	1.038	0.009	0.040
$^{48}V^{23+}$	1.056	0.009	0.040
$^{71}Se^{34+}$	0.977	0.009	0.040
$^{46}Ti^{22+}$	0.833	0.009	0.040
$^{67}Ge^{32+}$	0.785	0.006	0.040
$^{65}Ga^{31+}$	0.709	0.006	0.040
$^{63}Zn^{30+}$	0.599	0.006	0.040
$^{61}Cu^{29+}$	0.497	0.006	0.040
$^{59}Ni^{28+}$	0.416	0.006	0.040
$^{57}Co^{27+}$	0.383	0.006	0.040
$^{38}Ar^{18+}$	0.333	0.009	0.040
$^{36}Cl^{17+}$	0.395	0.011	0.040
$^{53}Mn^{25+}$	0.408	0.009	0.040
$^{51}Cr^{24+}$	0.485	0.009	0.040
$^{49}V^{23+}$	0.593	0.015	0.040
$^{69}As^{33+}$	0.871	0.009	0.040

Table D.14. Results of the mass measurement of the $^{72}Ge^{32+}$ first data set.

Ion	Reference	T (ns)	$\Delta M_{\mathrm{exp}} - \Delta M_{\mathrm{AME}}$ (keV)	ΔM_{exp} (keV)	$\sigma_{\Delta M_{\mathrm{exp}}}$ (keV)	$\sigma_{\Delta M_{\mathrm{AME}}}$ (keV)	$\sigma_{\Delta M_{\mathrm{sys}}}$ (keV)
$^{50}Ti^{22+}$	Y	520.983	14.604	−51417.263	7.414	0.082	8.530
$^{57}Mn^{25+}$	Y	521.854	−14.118	−57500.397	15.968	1.505	8.530
$^{66}Cu^{29+}$	Y	521.363	−8.576	−66266.865	15.261	0.649	8.530
$^{75}As^{33+}$	Y	520.999	−16.086	−73050.289	11.350	0.884	8.530
$^{68}Zn^{30+}$	Y	520.263	16.462	−69990.692	6.757	0.778	8.530
$^{72}Ge^{32+}$	Y	518.294	2.813	−72583.097	2.590	0.076	8.530
$^{63}Ni^{28+}$	Y	518.285	1.226	−65511.665	2.065	0.426	8.530
$^{54}Cr^{24+}$	Y	518.281	2.679	−56932.700	1.885	0.132	8.530
$^{74}As^{33+}$	Y	517.413	6.174	−70853.890	1.899	1.693	8.530
$^{74}Se^{33+}$	Y	517.408	−18.213	−72231.423	1.401	0.015	8.530
$^{65}Zn^{29+}$	Y	517.274	13.560	−65898.464	2.180	0.646	8.530
$^{65}Cu^{29+}$	Y	517.268	7.064	−67256.613	1.929	0.643	8.530
$^{56}Mn^{25+}$	Y	517.110	5.632	−56906.034	1.744	0.293	8.530
$^{47}Sc^{21+}$	Y	516.906	8.267	−44328.575	1.529	1.931	8.530
$^{38}Cl^{17+}$	Y	516.621	5.909	−29792.207	1.666	0.098	8.530
$^{76}Se^{34+}$	Y	516.562	−6.753	−75258.712	2.825	0.016	8.530
$^{67}Ga^{30+}$	Y	516.329	−8.795	−66887.951	4.214	1.176	8.530
$^{67}Zn^{30+}$	Y	516.325	10.004	−67870.372	2.576	0.755	8.530
$^{58}Fe^{26+}$	Y	516.006	7.261	−62148.010	2.417	0.316	8.530
$^{49}Ti^{22+}$	Y	515.617	14.510	−48549.502	2.166	0.078	8.530
$^{69}Ga^{31+}$	Y	515.441	3.965	−69323.855	3.021	1.197	8.530
$^{40}Ar^{18+}$	Y	515.055	15.989	−35023.911	3.952	0.002	8.530
$^{60}Co^{27+}$	Y	515.013	0.936	−61649.501	2.810	0.403	8.530
$^{71}Ge^{32+}$	Y	514.617	−1.438	−69908.095	3.434	0.815	8.530
$^{51}V^{23+}$	Y	514.446	8.974	−52194.131	3.243	0.097	8.530
$^{62}Ni^{28+}$	Y	514.067	−8.959	−66755.399	3.487	0.425	8.530
$^{42}K^{19+}$	Y	513.694	4.889	−35017.142	4.249	0.106	8.530
$^{53}Cr^{24+}$	Y	513.378	−1.507	−55289.125	4.002	0.116	8.530
$^{64}Cu^{29+}$	Y	513.216	−8.365	−65432.783	5.144	0.427	8.530
$^{57}Fe^{26+}$	Y	511.500	13.525	−60168.492	7.958	0.268	8.530
$^{44}Ca^{20+}$	Y	512.430	3.962	−41464.768	4.814	0.325	8.530
$^{59}Co^{27+}$	Y	510.669	4.519	−62225.319	9.686	0.397	8.530
$^{48}Ti^{22+}$	Y	510.289	−1.175	−48494.127	8.477	0.074	8.530
$^{61}Ni^{28+}$	Y	509.899	−8.172	−64230.201	12.357	0.355	8.530
$^{50}V^{23+}$	Y	509.376	−1.555	−49224.795	13.570	0.093	8.530
$^{52}Cr^{24+}$	Y	508.512	3.778	−55415.730	31.313	0.112	8.530
$^{72}As^{32+}$	N	518.311	**-28.411**	−68258.219	**2.143**	**4.083**	**8.530**

Table D.15. Results of the isochronicity curve of the $^{72}Ge^{32+}$ first data set (I).

Ion	σ_T (ps)	δ_{σ_T} (ps)	$\delta_{\sigma_{\text{sys}}}$ (ps)
$^{50}Ti^{22+}$	0.757	0.015	0.045
$^{57}Mn^{25+}$	0.982	0.026	0.045
$^{66}Cu^{29+}$	0.884	0.013	0.045
$^{75}As^{33+}$	0.744	0.013	0.045
$^{68}Zn^{30+}$	0.612	0.017	0.045
$^{72}Ge^{32+}$	0.160	0.002	0.045
$^{63}Ni^{28+}$	0.160	0.002	0.045
$^{54}Cr^{24+}$	0.162	0.002	0.045
$^{74}As^{33+}$	0.208	0.002	0.045
$^{74}Se^{33+}$	0.215	0.002	0.045
$^{65}Zn^{29+}$	0.261	0.006	0.045
$^{65}Cu^{29+}$	0.236	0.004	0.045
$^{56}Mn^{25+}$	0.272	0.004	0.045
$^{47}Sc^{21+}$	0.310	0.004	0.045
$^{38}Cl^{17+}$	0.358	0.011	0.045
$^{76}Se^{34+}$	0.409	0.004	0.045
$^{67}Ga^{30+}$	0.396	0.017	0.045
$^{67}Zn^{30+}$	0.465	0.004	0.045
$^{58}Fe^{26+}$	0.558	0.004	0.045
$^{49}Ti^{22+}$	0.671	0.006	0.045
$^{69}Ga^{31+}$	0.721	0.004	0.045
$^{40}Ar^{18+}$	0.739	0.027	0.045
$^{60}Co^{27+}$	0.859	0.006	0.045
$^{71}Ge^{32+}$	0.996	0.004	0.045
$^{51}V^{23+}$	1.015	0.013	0.045
$^{62}Ni^{28+}$	1.095	0.004	0.045
$^{42}K^{19+}$	1.349	0.025	0.045
$^{53}Cr^{24+}$	1.316	0.008	0.045
$^{64}Cu^{29+}$	1.332	0.008	0.045
$^{57}Fe^{26+}$	1.857	0.015	0.045
$^{44}Ca^{20+}$	1.557	0.015	0.045
$^{59}Co^{27+}$	2.156	0.032	0.045

Table D.16. Results of the isochronicity curve of the $^{72}Ge^{32+}$ first data set (II).

Ion	σ_T (ps)	δ_{σ_T} (ps)	$\delta_{\sigma_{\mathrm{sys}}}$ (ps)
$^{48}Ti^{22+}$	2.230	0.019	0.045
$^{61}Ni^{28+}$	2.187	0.029	0.045
$^{50}V^{23+}$	2.425	0.019	0.045
$^{52}Cr^{24+}$	2.682	0.023	0.045
$^{72}As^{32+}$	0.164	0.002	0.045

Table D.17. Results of the mass measurement of the $^{72}Ge^{32+}$ second data set.

Ion	Reference	T (ns)	$\Delta M_{\mathrm{exp}} - \Delta M_{\mathrm{AME}}$ (keV)	ΔM_{exp} (keV)	$\sigma_{\Delta M_{\mathrm{exp}}}$ (keV)	$\sigma_{\Delta M_{\mathrm{AME}}}$ (keV)	$\sigma_{\Delta M_{\mathrm{sys}}}$ (keV)
$^{64}Ni^{28+}$	Y	522.523	−20.738	−67119.772	15.912	0.463	7.920
$^{50}Ti^{22+}$	Y	520.983	19.369	−51412.498	3.971	0.082	7.920
$^{57}Mn^{25+}$	Y	521.854	−9.800	−57496.079	8.386	1.505	7.920
$^{66}Cu^{29+}$	Y	521.363	11.309	−66246.980	7.310	0.649	7.920
$^{75}Se^{33+}$	Y	521.002	−10.839	−72180.328	6.036	0.073	7.920
$^{68}Zn^{30+}$	Y	520.263	0.254	−70006.900	3.295	0.778	7.920
$^{52}V^{23+}$	Y	519.587	1.368	−51441.664	1.781	0.159	7.920
$^{61}Co^{27+}$	Y	519.384	1.702	−62896.477	1.726	0.839	7.920
$^{70}Ga^{31+}$	Y	519.256	−1.312	−68911.462	1.834	1.201	7.920
$^{70}Ge^{31+}$	Y	519.249	−15.757	−70577.793	1.734	0.820	7.920
$^{72}Ge^{32+}$	Y	518.294	1.446	−72584.464	1.481	0.076	7.920
$^{63}Ni^{28+}$	Y	518.285	0.221	−65512.670	1.015	0.426	7.920
$^{54}Cr^{24+}$	Y	518.281	1.524	−56933.855	0.947	0.132	7.920
$^{74}As^{33+}$	Y	517.413	3.539	−70856.525	1.390	1.693	7.920
$^{74}Se^{33+}$	Y	517.408	−17.122	−72230.332	1.129	0.015	7.920
$^{65}Zn^{29+}$	Y	517.274	−10.323	−65922.347	1.874	0.646	7.920
$^{65}Cu^{29+}$	Y	517.268	3.987	−67259.690	1.304	0.643	7.920
$^{56}Mn^{25+}$	Y	517.110	3.932	−56907.734	1.213	0.293	7.920
$^{47}Sc^{21+}$	Y	516.906	4.181	−44332.661	1.065	1.931	7.920
$^{38}Cl^{17+}$	Y	516.621	0.986	−29797.130	1.249	0.098	7.920
$^{76}Se^{34+}$	Y	516.562	−1.418	−75253.377	2.208	0.016	7.920
$^{67}Zn^{30+}$	Y	516.325	5.106	−67875.270	1.869	0.755	7.920
$^{58}Fe^{26+}$	Y	516.006	5.501	−62149.770	1.828	0.316	7.920
$^{49}Ti^{22+}$	Y	515.617	8.534	−48555.478	1.669	0.078	7.920
$^{69}Ga^{31+}$	Y	515.441	2.041	−69325.779	2.425	1.197	7.920
$^{40}Ar^{18+}$	Y	515.055	0.062	−35039.838	2.741	0.002	7.920
$^{60}Co^{27+}$	Y	515.013	1.862	−61648.575	2.270	0.403	7.920
$^{51}V^{23+}$	Y	514.446	−9.909	−52213.014	2.207	0.097	7.920
$^{62}Ni^{28+}$	Y	514.067	−10.106	−66756.546	2.732	0.425	7.920
$^{42}K^{19+}$	Y	513.693	−3.231	−35025.262	2.275	0.106	7.920
$^{53}Cr^{24+}$	Y	513.378	−3.638	−55291.256	2.980	0.116	7.920
$^{64}Cu^{29+}$	Y	513.215	−4.492	−65428.910	3.713	0.427	7.920
$^{57}Fe^{26+}$	Y	511.500	10.534	−60171.483	5.175	0.268	7.920
$^{46}Sc^{21+}$	Y	511.326	16.509	−41745.134	4.554	0.671	7.920
$^{44}Ca^{20+}$	Y	512.430	5.889	−41462.841	3.244	0.325	7.920
$^{68}Ga^{31+}$	Y	511.664	−7.054	−67093.108	7.418	1.430	7.920
$^{59}Co^{27+}$	Y	510.669	−0.065	−62229.903	6.110	0.397	7.920
$^{48}Ti^{22+}$	Y	510.288	−0.152	−48493.104	5.247	0.074	7.920
$^{61}Ni^{28+}$	Y	509.899	−0.710	−64222.739	7.302	0.355	7.920
$^{50}V^{23+}$	Y	509.375	−1.925	−49225.165	7.109	0.093	7.920
$^{39}Ar^{18+}$	Y	508.569	27.075	−33215.120	8.132	5.000	7.920
$^{52}Cr^{24+}$	Y	508.511	−2.023	−55421.531	13.078	0.112	7.920
$^{54}Mn^{25+}$	Y	507.748	−27.469	−55585.716	20.088	1.007	7.920
$^{41}K^{19+}$	Y	507.547	11.397	−35548.152	17.107	0.004	7.920
$^{72}As^{32+}$	N	518.311	**-27.458**	−68257.266	**1.110**	**4.083**	**7.920**

Table D.18. Results of the isochronicity curve of the $^{72}Ge^{32+}$ second data set (I).

Ion	σ_T (ps)	δ_{σ_T} (ps)	$\delta_{\sigma_{\mathrm{sys}}}$ (ps)
$^{64}Ni^{28+}$	0.632	0.017	0.022
$^{50}Ti^{22+}$	0.500	0.011	0.022
$^{57}Mn^{25+}$	0.549	0.013	0.022
$^{66}Cu^{29+}$	0.499	0.006	0.022
$^{75}Se^{33+}$	0.455	0.009	0.022
$^{68}Zn^{30+}$	0.361	0.006	0.022
$^{52}V^{23+}$	0.251	0.006	0.022
$^{61}Co^{27+}$	0.214	0.002	0.022
$^{70}Ga^{31+}$	0.197	0.002	0.022
$^{70}Ge^{31+}$	0.193	0.002	0.022
$^{72}Ge^{32+}$	0.124	0.001	0.022
$^{63}Ni^{28+}$	0.125	0.001	0.022
$^{54}Cr^{24+}$	0.124	0.001	0.022
$^{74}As^{33+}$	0.183	0.002	0.022
$^{74}Se^{33+}$	0.193	0.002	0.022
$^{65}Zn^{29+}$	0.197	0.006	0.022
$^{65}Cu^{29+}$	0.202	0.002	0.022
$^{56}Mn^{25+}$	0.216	0.002	0.022
$^{47}Sc^{21+}$	0.246	0.002	0.022
$^{38}Cl^{17+}$	0.284	0.006	0.022
$^{76}Se^{34+}$	0.294	0.004	0.022
$^{67}Zn^{30+}$	0.315	0.002	0.022
$^{58}Fe^{26+}$	0.357	0.004	0.022
$^{49}Ti^{22+}$	0.416	0.004	0.022
$^{69}Ga^{31+}$	0.434	0.004	0.022
$^{40}Ar^{18+}$	0.533	0.019	0.022
$^{60}Co^{27+}$	0.509	0.004	0.022
$^{51}V^{23+}$	0.561	0.006	0.022
$^{62}Ni^{28+}$	0.628	0.004	0.022
$^{42}K^{19+}$	0.678	0.008	0.022
$^{53}Cr^{24+}$	0.713	0.006	0.022
$^{64}Cu^{29+}$	0.746	0.006	0.022
$^{57}Fe^{26+}$	0.963	0.010	0.022

Table D.19. Results of the isochronicity curve of the $^{72}Ge^{32+}$ second data set (II).

Ion	σ_T (ps)	δ_{σ_T} (ps)	$\delta_{\sigma_{\text{sys}}}$ (ps)
$^{46}Sc^{21+}$	1.056	0.015	0.022
$^{44}Ca^{20+}$	0.842	0.008	0.022
$^{68}Ga^{31+}$	0.957	0.021	0.022
$^{59}Co^{27+}$	1.060	0.013	0.022
$^{48}Ti^{22+}$	1.147	0.013	0.022
$^{61}Ni^{28+}$	1.155	0.015	0.022
$^{50}V^{23+}$	1.325	0.010	0.022
$^{39}Ar^{18+}$	1.452	0.023	0.022
$^{52}Cr^{24+}$	1.428	0.013	0.022
$^{54}Mn^{25+}$	1.468	0.069	0.022
$^{41}K^{19+}$	1.571	0.042	0.022
$^{72}As^{32+}$	0.126	0.001	0.022

List of Publications

Parts of this work have been submitted to, and will be submitted to, various scientific journals. Below is my list of publications and their corresponding usage within this thesis.

Utilized publications

- D. Freire-Fernández, *et al.*, "*Measurement of the Isolated Nuclear Two-Photon Decay in* ^{72}Ge", under review in Physical Review Letters. A pre-printed version can be found under 10.48550/arXiv:2312.11313. This latter version is cited as [180].
  - Parts of the text, tables and figures of §4.5.1, §4.6.1 and §5.1 have been taken from [180], as indicated in their first paragraph.

Developed software packages

- D. Freire-Fernández, and G. Hudson-Chang, "*RionID: Collection of code for the identification of ringed ions in Python*", Zenodo: 10.5281/zenodo.8169342. Cited as [162].
  - This software was utilized for the ion identification (refer to §3.3.2.1 and §4.2).
- D. Freire-Fernández, "*TDMchopS: A toolkit for automatic chopping of continuously acquired complex valued radio frequency samples*", Zenodo: 10.5281/zenodo.8172227. Cited as [161].
  - This software was used for the determination of the time of injection in the NTCAP data (refer to §3.3.1.3).

All my software can be found in GitHub: @DFreireF

Manuscripts in preparation

The following manuscripts are currently under preparation and will incorporate text, figures and tables from this thesis:

- D. Freire-Fernández, *et al.*, *"First electron conversion factor measurements at storage rings"*, (in preparation).

- D. Freire-Fernández, *et al.*, "*$B\rho$-allowed combined Schottky plus Isochronous Mass Spectrometry (S+IMS)*", (in preparation).

Non-used publications

The following publications, to which I also contributed as a co-author, have not been used in this thesis:

- M. Sguazzin, *et al.*, "*First measurement of the neutron-emission probability with a surrogate reaction in inverse kinematics at a heavy-ion storage ring*", under review in Physical Review Letters. The pre-print can be found under 10.48550/arXiv.2312.13742.
- S. F. Dellmann, *et al.*, "*Proton capture on stored radioactive Te ions*". EPJ Web of Conferences 279, 11018.
- M. Sguazzin, *et al.*, "*Indirect measurements of neutron-induced reaction crosssections at heavy-ion storage rings*". EPJ Web of Conferences 279, 11006.

All my past, present and future research will be found at: https://orcid.org/0000-0002-5898-9291.

Bibliography

[1] A. Einstein. *Annalen der Physik* 323.13 (1905), pp. 639–641. DOI: https://doi.org/10.1002/andp.19053231314. eprint: https://onlinelibrary.wiley.com/doi/pdf/10.1002/andp.19053231314. URL: https://onlinelibrary.wiley.com/doi/abs/10.1002/andp.19053231314

[2] Eite Tiesinga et al. en. 93 (2021). DOI: https://doi.org/10.1103/RevModPhys.93.025010. URL: https://tsapps.nist.gov/publication/get_pdf.cfm?pub_id=931443

[3] Terry Renner et al. The Royal Society of Chemistry, 2007. DOI: 10.1039/9781847557889. URL: https://doi.org/10.1039/9781847557889

[4] J. Repp et al. *Applied Physics B* 107.4 (2012), pp. 983–996. DOI: 10.1007/s00340-011-4823-6. URL: https://doi.org/10.1007/s00340-011-4823-6

[5] A. Rischka et al. *Phys. Rev. Lett.* 124 (2020), p. 113001. DOI: 10.1103/PhysRevLett.124.113001. URL: https://link.aps.org/doi/10.1103/PhysRevLett.124.113001

[6] C.E. Rolfs and W.S. Rodney. Theoretical Astrophysics. University of Chicago Press, 1988. URL: https://books.google.de/books?id=BHKLFPUS1RcC

[7] Mary K. Gaillard, Paul D. Grannis, and Frank J. Sciulli. *Rev. Mod. Phys.* 71 (1999), S96–S111. DOI: 10.1103/RevModPhys.71.S96. URL: https://link.aps.org/doi/10.1103/RevModPhys.71.S96

[8] Paul Langacker. Publication place not specified: Taylor & Francis, 2017. DOI: 10.1201/b22175. URL: https://library.oapen.org/handle/20.500.12657/50890

[9] Klaus Blaum. *Physics Reports* 425.1 (2006), pp. 1–78. DOI: https://doi.org/10.1016/j.physrep.2005.10.011. URL: https://www.sciencedirect.com/science/article/pii/S0370157305004643

[10] Lowell S. Brown and Gerald Gabrielse. *Rev. Mod. Phys.* 58 (1986), pp. 233–311. DOI: 10.1103/RevModPhys.58.233. URL: https://link.aps.org/doi/10.1103/RevModPhys.58.233

[11] S. Sturm et al. *Nature* 506.7489 (2014), pp. 467–470. DOI: 10.1038/nature13026. URL: https://doi.org/10.1038/nature13026

[12] C. Smorra et al. *Nature* 550.7676 (2017), pp. 371–374. DOI: 10.1038/nature24048. URL: https://doi.org/10.1038/nature24048

[13] F. Heiße et al. *Phys. Rev. A* 100 (2019), p. 022518. DOI: 10.1103/PhysRevA.100.022518. URL: https://link.aps.org/doi/10.1103/PhysRevA.100.022518

[14] Markus Steck and Yuri A. Litvinov. *Progress in Particle and Nuclear Physics* 115 (2020), p. 103811. DOI: https://doi.org/10.1016/j.ppnp.2020.103811. URL: https://www.sciencedirect.com/science/article/pii/S0146641020300582

[15] Yury A. Litvinov and Rui Jiu Chen. *The European Physical Journal A* 59.5 (2023), p. 102. DOI: 10.1140/epja/s10050-023-00978-w. URL: https://doi.org/10.1140/epja/s10050-023-00978-w

[16] J. Glorius et al. *Phys. Rev. Lett.* 122 (2019), p. 092701. DOI: 10.1103/PhysRevLett.122.092701. URL: https://link.aps.org/doi/10.1103/PhysRevLett.122.092701

[17] J. Glorius et al. *Nuclear Instruments and Methods in Physics Research Section B: Beam Interactions with Materials and Atoms* 541 (2023), pp. 190–193. DOI: https://doi.org/10.1016/j.nimb.2023.04.059. URL: https://www.sciencedirect.com/science/article/pii/S0168583X23001957

[18] S. F. Dellmann. PhD thesis. Johann Wolfgang Goethe-Universität Frankfurt am Main, 2024. DOI: 10.21248/gups.82236. URL: https://doi.org/10.21248/gups.82236

[19] H. Reich et al. *Nuclear Physics A* 626.1 (1997). Proceedings of the Third International Conference on Nuclear Physics at Storage Rings, pp. 417–425. DOI: https://doi.org/10.1016/S0375-9474(97)00564-2. URL: https://www.sciencedirect.com/science/article/pii/S0375947497005642

[20] René Reifarth and Yuri A. Litvinov. *Phys. Rev. ST Accel. Beams* 17 (2014), p. 014701. DOI: 10.1103/PhysRevSTAB.17.014701. URL: https://link.aps.org/doi/10.1103/PhysRevSTAB.17.014701

[21] René Reifarth et al. *Phys. Rev. Accel. Beams* 20 (2017), p. 044701. DOI: 10.1103/PhysRevAccelBeams.20.044701. URL: https://link.aps.org/doi/10.1103/PhysRevAccelBeams.20.044701

[22] J.W. Xia et al. *Nuclear Instruments and Methods in Physics Research Section A: Accelerators, Spectrometers, Detectors and Associated Equipment* 488.1 (2002), pp. 11–25. DOI: https://doi.org/10.1016/S0168-9002(02)00475-8. URL: https://www.sciencedirect.com/science/article/pii/S0168900202004758

[23] A. Ozawa et al. *Progress of Theoretical and Experimental Physics* 2012.1 (2012), p. 03C009. DOI: 10.1093/ptep/pts060. eprint: https://academic.oup.com/ptep/article-pdf/2012/1/03C009/11594752/pts060.pdf. URL: https://doi.org/10.1093/ptep/pts060

[24] Bernhard Franzke. *Nuclear Instruments and Methods in Physics Research Section B: Beam Interactions with Materials and Atoms* 24-25 (1987), pp. 18–25. DOI: https://doi.org/10.1016/0168-583X(87)90583-0. URL: https://www.sciencedirect.com/science/article/pii/0168583X87905830

[25] Bernhard Franzke, Hans Geissel, and Gottfried Münzenberg. *Mass Spectrometry Reviews* 27 (2008), pp. 428–469. DOI: 10.1002/mas.20173. URL: https://onlinelibrary.wiley.com/doi/abs/10.1002/mas.20173

[26] Markus Steck and Yuri A Litvinov. *Progress in Particle and Nuclear Physics* 115 (2020), p. 103811. DOI: 10.1016/j.ppnp.2020.103811. URL: https://doi.org/10.1016/j.ppnp.2020.103811

[27] B Franzke et al. *Physica Scripta* 1995.T59 (1995), p. 176. DOI: 10.1088/0031-8949/1995/T59/021. URL: https://dx.doi.org/10.1088/0031-8949/1995/T59/021

[28] M. Hausmann et al. *Nuclear Instruments and Methods in Physics Research Section A: Accelerators, Spectrometers, Detectors and Associated Equipment* 446.3 (2000), pp. 569–580. DOI: http://dx.doi.org/10.1016/S0168-9002(99)01192-4. URL: http://www.sciencedirect.com/science/article/pii/S0168900299011924

[29] T. Radon et al. *Phys. Rev. Lett.* 78 (1997), pp. 4701–4704. DOI: 10.1103/PhysRevLett.78.4701. URL: https://link.aps.org/doi/10.1103/PhysRevLett.78.4701

[30] E. Métral and D. Möhl. Ed. by S. Gilardoni and D. Manglunki. Vol. 1. CERN-2011-004. 2011, p. 59. DOI: 10.5170/CERN-2011-004. URL: http://dx.doi.org/10.5170/CERN-2011-004

[31] G I Budker and Aleksandr N Skrinskiĭ. *Soviet Physics Uspekhi* 21.4 (1978), p. 277. DOI: 10.1070/PU1978v021n04ABEH005537. URL: https://dx.doi.org/10.1070/PU1978v021n04ABEH005537

[32] S van der Meer. Tech. rep. Geneva: CERN, 1972. URL: https://cds.cern.ch/record/312939

[33] S. Schröder et al. *Phys. Rev. Lett.* 64 (1990), pp. 2901–2904. DOI: 10.1103/PhysRevLett.64.2901. URL: https://link.aps.org/doi/10.1103/PhysRevLett.64.2901

[34] M. Steck et al. *Nuclear Instruments and Methods in Physics Research Section A: Accelerators, Spectrometers, Detectors and Associated Equipment* 532.1 (2004). International Workshop on Beam Cooling and Related Topics, pp. 357–365. DOI: https://doi.org/10.1016/j.nima.2004.06.065. URL: https://www.sciencedirect.com/science/article/pii/S0168900204012689

[35] F Nolden et al. *Nuclear Instruments and Methods in Physics Research Section A: Accelerators, Spectrometers, Detectors and Associated Equipment* 441.1 (2000), pp. 219–222. DOI: https://doi.org/10.1016/S0168-9002(99)01136-5. URL: https://www.sciencedirect.com/science/article/pii/S0168900299011365

[36] F. M. Gonzalez et al. (UCNτ Collaboration Collaboration). *Phys. Rev. Lett.* 127 (2021), p. 162501. DOI: 10.1103/PhysRevLett.127.162501. URL: https://link.aps.org/doi/10.1103/PhysRevLett.127.162501

[37] M. Goeppert-Mayer. *Phys. Rev.* 48 (1935), pp. 512–516. DOI: 10.1103/PhysRev.48.512. URL: https://link.aps.org/doi/10.1103/PhysRev.48.512

[38] J. Schechter and J. W. F. Valle. *Phys. Rev. D* 25 (1982), pp. 2951–2954. DOI: 10.1103/PhysRevD.25.2951. URL: https://link.aps.org/doi/10.1103/PhysRevD.25.2951

[39] Jonathan Engel and Javier Menéndez. *Reports on Progress in Physics* 80.4 (2017), p. 046301. DOI: 10.1088/1361-6633/aa5bc5. URL: https://dx.doi.org/10.1088/1361-6633/aa5bc5

[40] B. Romeo, J. Menéndez, and C. Peña Garay. *Physics Letters B* 827 (2022), p. 136965. DOI: https://doi.org/10.1016/j.physletb.2022.136965. URL: https://www.sciencedirect.com/science/article/pii/S0370269322000995

[41] V. F. Weisskopf. *Phys. Rev.* 83 (1951), pp. 1073–1073. DOI: 10.1103/PhysRev.83.1073. URL: https://link.aps.org/doi/10.1103/PhysRev.83.1073

[42] Gordon R. Gilmore. John Wiley & Sons, Ltd, 2008. DOI: 10.1002/9780470861981. URL: https://doi.org/10.1002/9780470861981

[43] S. Akkoyun et al. *Nuclear Instruments and Methods in Physics Research Section A: Accelerators, Spectrometers, Detectors and Associated Equipment* 668 (2012), pp. 26–58. DOI: https://doi.org/10.1016/j.nima.2011.11.081. URL: https://www.sciencedirect.com/science/article/pii/S0168900211021516

[44] W. Korten et al. *The European Physical Journal A* 56.5 (2020), p. 137. DOI: 10.1140/epja/s10050-020-00132-w. URL: https://doi.org/10.1140/epja/s10050-020-00132-w

[45] J. Eberth et al. *The European Physical Journal A* 59.8 (2023), p. 179. DOI: 10.1140/epja/s10050-023-01093-6. URL: https://doi.org/10.1140/epja/s10050-023-01093-6

[46] T. Kibédi et al. *Nuclear Instruments and Methods in Physics Research Section A: Accelerators, Spectrometers, Detectors and Associated Equipment* 589.2 (2008), pp. 202–229. DOI: https://doi.org/10.1016/j.nima.2008.02.051. URL: https://www.sciencedirect.com/science/article/pii/S0168900208002520

[47] Philip M. Walker and James J. Carroll. *Physics Today* 58.6 (2005), pp. 39–44. DOI: 10.1063/1.1996473. eprint: https://pubs.aip.org/physicstoday/article-pdf/58/6/39/16746664/39_1_online.pdf. URL: https://doi.org/10.1063/1.1996473

[48] James J. Carroll. *Nuclear Instruments and Methods in Physics Research Section B: Beam Interactions with Materials and Atoms* 261.1 (2007). The Application of Accelerators in Research and Industry, pp. 960–964. DOI: https://doi.org/10.1016/j.nimb.2007.04.128. URL: https://www.sciencedirect.com/science/article/pii/S0168583X07009275

[49] Powell Richards, Walter D. Tucker, and Suresh C. Srivastava. *The International Journal of Applied Radiation and Isotopes* 33.10 (1982), pp. 793–799. DOI: https://doi.org/10.1016/0020-708X(82)90120-X. URL: https://www.sciencedirect.com/science/article/pii/0020708X8290120X

[50] Benedict Seiferle et al. *Nature* 573.7773 (2019), pp. 243–246. DOI: 10.1038/s41586-019-1533-4. URL: https://doi.org/10.1038/s41586-019-1533-4

[51] Sandro Kraemer et al. *Nature* 617.7962 (2023), pp. 706–710. DOI: 10.1038/s41586-023-05894-z. URL: https://doi.org/10.1038/s41586-023-05894-z

[52] Yuri Shvyd'ko et al. *Nature* 622.7983 (2023), pp. 471–475. DOI: 10.1038/s41586-023-06491-w. URL: https://doi.org/10.1038/s41586-023-06491-w

[53] Philip Walker and George Dracoulis. *Nature* 399.6731 (1999), pp. 35–40. DOI: 10.1038/19911. URL: https://doi.org/10.1038/19911

[54] Philip M. Walker and Zsolt Podolyák. *Handbook of Nuclear Physics*. Ed. by Isao Tanihata, Hiroshi Toki, and Toshitaka Kajino. Singapore: Springer Nature Singapore, 2020, pp. 1–37. DOI: 10.1007/978-981-15-8818-1_46-1. URL: https://doi.org/10.1007/978-981-15-8818-1_46-1

[55] Ashok Kumar Jain, Bhoomika Maheshwari, and Alpana Goel. *A Primer*. 1st ed. Springer Cham, 2021, pp. XV, 144. DOI: 10.1007/978-3-030-78675-5. URL: https://doi.org/10.1007/978-3-030-78675-5

[56] Peter Ring and Peter Schuck. 1st ed. Theoretical and Mathematical Physics. Springer Berlin, Heidelberg, 1980

[57] David Freire-Fernández. https://github.com/DFreireF/nudeform. 2024

[58] E. Bouchez et al. *Phys. Rev. Lett.* 90 (2003), p. 082502. DOI: 10.1103/PhysRevLett.90.082502. URL: https://link.aps.org/doi/10.1103/PhysRevLett.90.082502

[59] M. Girod et al. *Phys. Rev. Lett.* 62 (1989), pp. 2452–2455. DOI: 10.1103/PhysRevLett.62.2452. URL: https://link.aps.org/doi/10.1103/PhysRevLett.62.2452

[60] Marta Borrajo, Tomás R. Rodríguez, and J. Luis Egido. *Physics Letters B* 746 (2015), pp. 341–346. DOI: https://doi.org/10.1016/j.physletb.2015.05.030. URL: https://www.sciencedirect.com/science/article/pii/S0370269315003676

[61] Kris Heyde and John L. Wood. *Rev. Mod. Phys.* 83 (2011), pp. 1467–1521. DOI: 10.1103/RevModPhys.83.1467. URL: https://link.aps.org/doi/10.1103/RevModPhys.83.1467

[62] Paul E. Garrett, Magda Zielińska, and Emmanuel Clément. *Progress in Particle and Nuclear Physics* 124 (2022), p. 103931. DOI: https://doi.org/10.1016/j.ppnp.2021.103931. URL: https://www.sciencedirect.com/science/article/pii/S0146641021000922

[63] Y. L. Yang, P. W. Zhao, and Z. P. Li. *Phys. Rev. C* 107 (2023), p. 024308. DOI: 10.1103/PhysRevC.107.024308. URL: https://link.aps.org/doi/10.1103/PhysRevC.107.024308

[64] Andreas Görgen and Wolfram Korten. *Journal of Physics G: Nuclear and Particle Physics* 43.2 (2016), p. 024002. DOI: 10.1088/0954-3899/43/2/024002. URL: https://dx.doi.org/10.1088/0954-3899/43/2/024002

[65] T. Kibedi, A.B. Garnsworthy, and J.L. Wood. *Progress in Particle and Nuclear Physics* 123 (2022), p. 103930. DOI: 10.1016/j.ppnp.2021.103930. URL: https://www.sciencedirect.com/science/article/pii/S0146641021000910

[66] S. E. Woosley and W. M. Howard. *Astrophysical Journal Supplement Series* 36 (1978), pp. 285–304. DOI: 10.1086/190501

[67] C. Freiburghaus, S. Rosswog, and F.-K. Thielemann. *The Astrophysical Journal* 525.2 (1999), p. L121. DOI: 10.1086/312343. URL: https://dx.doi.org/10.1086/312343

[68] F. Käppeler et al. *Rev. Mod. Phys.* 83 (2011), pp. 157–193. DOI: 10.1103/RevModPhys.83.157. URL: https://link.aps.org/doi/10.1103/RevModPhys.83.157

[69] John J. Cowan, Friedrich-Karl Thielemann, and James W. Truran. *Physics Reports* 208.4 (1991), pp. 267–394. DOI: https://doi.org/10.1016/0370-1573(91)90070-3. URL: https://www.sciencedirect.com/science/article/pii/0370157391900703

[70] H. Schatz et al. *Physics Reports* 294.4 (1998), pp. 167–263. DOI: https://doi.org/10.1016/S0370-1573(97)00048-3. URL: https://www.sciencedirect.com/science/article/pii/S0370157397000483

[71] G. Wendell Misch et al. *The Astrophysical Journal Supplement Series* 252.1 (2020), p. 2. DOI: 10.3847/1538-4365/abc41d. URL: https://dx.doi.org/10.3847/1538-4365/abc41d

[72] G. Wendell Misch, T. M. Sprouse, and M. R. Mumpower. *The Astrophysical Journal Letters* 913.1 (2021), p. L2. DOI: 10.3847/2041-8213/abfb74. URL: https://dx.doi.org/10.3847/2041-8213/abfb74

[73] René Reifarth et al. *International Journal of Modern Physics A* 33.09 (2018), p. 1843011. DOI: 10.1142/S0217751X1843011X. eprint: https://doi.org/10.1142/S0217751X1843011X. URL: https://doi.org/10.1142/S0217751X1843011X

[74] Wenru Fan et al. *Phys. Rev. Res.* 5 (2023), p. 043120. DOI: 10.1103/PhysRevResearch.5.043120. URL: https://link.aps.org/doi/10.1103/PhysRevResearch.5.043120

[75] N. Gerken. PhD thesis. 2021. URL: https://purl.lib.fsu.edu/diginole/2021_Summer_Gerken_fsu_0071E_16472

[76] Eric B. Norman. *Atoms* 11.11 (2023). DOI: 10.3390/atoms11110140. URL: https://www.mdpi.com/2218-2004/11/11/140

[77] I. Tews et al. *Phys. Rev. Lett.* 110 (2013), p. 032504. DOI: 10.1103/PhysRevLett.110.032504. URL: https://link.aps.org/doi/10.1103/PhysRevLett.110.032504

[78] A. Tamii et al. *Phys. Rev. Lett.* 107 (2011), p. 062502. DOI: 10.1103/PhysRevLett.107.062502. URL: https://link.aps.org/doi/10.1103/PhysRevLett.107.062502

[79] Maria Göppert. *Naturwissenschaften* 17 (1929), p. 932. DOI: 10.1007/BF01506585. URL: https://doi.org/10.1007/BF01506585

[80] Maria Göppert-Mayer. *Annalen der Physik* 401 (1931), pp. 273–294. DOI: 10.1002/andp.19314010303. URL: https://onlinelibrary.wiley.com/doi/abs/10.1002/andp.19314010303

[81] J. R. Oppenheimer and J. S. Schwinger. *Phys. Rev.* 56 (1939), pp. 1066–1067. DOI: 10.1103/PhysRev.56.1066. URL: https://link.aps.org/doi/10.1103/PhysRev.56.1066

[82] D.P. Grechukhin. *Journal of Experimental and Theoretical Physics (U.S.S.R.)* 32 (1957), pp. 1036–1049. URL: http://www.jetp.ras.ru/cgi-bin/dn/e_005_05_0846.pdf

[83] D.P. Grechukhin. *Nuclear Physics* 35 (1962), pp. 98–113. DOI: https://doi.org/10.1016/0029-5582(62)90099-8. URL: https://www.sciencedirect.com/science/article/pii/0029558262900998

[84] D.P. Grechukhin. *Nuclear Physics* 47 (1963), pp. 273–292. DOI: 10.1016/0029-5582(63)90873-3. URL: https://www.sciencedirect.com/science/article/pii/0029558263908733

[85] D.P. Grechukhin. *Nuclear Physics* 62.2 (1965), pp. 273–295. DOI: https://doi.org/10.1016/0029-5582(65)90870-9. URL: https://www.sciencedirect.com/science/article/pii/0029558265908709

[86] Jörg Eichler and Gerhard Jacob. *Zeitschrift für Physik* 157 (1959), pp. 286–300. DOI: 10.1007/BF01374909. URL: https://doi.org/10.1007/BF01374909

[87] Jörg Eichler. *Physical Review A* 9 (1974), pp. 1762–1764. DOI: 10.1103/PhysRevA.9.1762. URL: https://link.aps.org/doi/10.1103/PhysRevA.9.1762

[88] J.L Friar and M Rosen. *Annals of Physics* 87 (1974), pp. 289–326. DOI: 10.1016/0003-4916(74)90038-4. URL: https://www.sciencedirect.com/science/article/pii/0003491674900384

[89] J.L Friar. *Annals of Physics* 95 (1975), pp. 170–201. DOI: 10.1016/0003-4916(75)90049-4. URL: https://www.sciencedirect.com/science/article/pii/0003491675900494

[90] J. Kramp et al. *Nuclear Physics A* 474 (1987), pp. 412–450. DOI: 10.1016/0375-9474(87)90625-7. URL: https://www.sciencedirect.com/science/article/pii/0375947487906257

[91] A Bohr and B R Mottelson (1969). URL: https://www.osti.gov/biblio/4785718

[92] W. Heisenberg. *Zeitschrift für Physik* 43.3 (1927), pp. 172–198. DOI: 10.1007/BF01397280. URL: https://doi.org/10.1007/BF01397280

[93] Michael E. Peskin and Daniel V. Schroeder. Reading, USA: Addison-Wesley, 1995

[94] J Speth and A van der Woude. *Reports on Progress in Physics* 44.7 (1981), p. 719. DOI: 10.1088/0034-4885/44/7/002. URL: https://dx.doi.org/10.1088/0034-4885/44/7/002

[95] M N Harakeh and A van der Woude. Oxford University Press, 2001. DOI: 10.1093/oso/9780198517337.003.0001. eprint: https://academic.oup.com/book/0/chapter/422644891/chapter-pdf/52568788/isbn-9780198517337-book-part-1.pdf. URL: https://doi.org/10.1093/oso/9780198517337.003.0001

[96] B. Margolis. *Nuclear Physics* 28.1 (1961), pp. 524–528. DOI: https://doi.org/10.1016/0029-5582(61)91074-4. URL: https://www.sciencedirect.com/science/article/pii/0029558261910744

[97] J. Schirmer et al. *Phys. Rev. Lett.* 53 (1984), pp. 1897–1900. DOI: 10.1103/PhysRevLett.53.1897. URL: https://link.aps.org/doi/10.1103/PhysRevLett.53.1897

[98] R. S. Simon. Tech. rep. Germany: GSI–80-2, 1980, p. 13. URL: https://hal.science/jpa-00220650/document

[99] V. Metag et al. *Detectors in Heavy-Ion Reactions: Proceedings of the Symposium Commemorating the 100th Anniversary of Hans Geiger's Birth Held at the Hahn-Meitner-Institut für Kernforschung Berlin October 6–8, 1982*. Springer Berlin Heidelberg, 1983, pp. 163–178. URL: https://link.springer.com/content/pdf/10.1007/3-540-12001-7_251.pdf

[100] V. Metag et al. *Nuclear Physics A* 409 (1983), pp. 331–342. DOI: https://doi.org/10.1016/0375-9474(83)90695-4. URL: https://www.sciencedirect.com/science/article/pii/0375947483906954

[101] S. Gorodetzky et al. *Phys. Rev. Lett.* 7 (1961), pp. 170–172. DOI: 10.1103/PhysRevLett.7.170. URL: https://link.aps.org/doi/10.1103/PhysRevLett.7.170

[102] D. E. Alburger and P. D. Parker. *Phys. Rev.* 135 (1964), B294–B300. DOI: 10.1103/PhysRev.135.B294. URL: https://link.aps.org/doi/10.1103/PhysRev.135.B294

[103] W. J. Bralthwalte, A. W. Obst, and C. H. King. 1973. URL: https://inis.iaea.org/collection/NCLCollectionStore/_Public/06/184/6184201.pdf

[104] B. A. Watson et al. *Phys. Rev. Lett.* 35 (1975), pp. 1333–1336. DOI: 10.1103/PhysRevLett.35.1333. URL: https://link.aps.org/doi/10.1103/PhysRevLett.35.1333

[105] Gorodetzky, S. et al. *J. Phys. Radium* 22.10 (1961), pp. 688–689. DOI: 10.1051/jphysrad:019610022010068800. URL: https://doi.org/10.1051/jphysrad:019610022010068800

[106] M. Nessin, T. H. Kruse, and K. E. Eklund. *Phys. Rev.* 125 (1962), pp. 639–647. DOI: 10.1103/PhysRev.125.639. URL: https://link.aps.org/doi/10.1103/PhysRev.125.639

[107] P. Harihar, J. D. Ullman, and C. S. Wu. *Phys. Rev. C* 2 (1970), pp. 462–467. DOI: 10.1103/PhysRevC.2.462. URL: https://link.aps.org/doi/10.1103/PhysRevC.2.462

[108] E. Beardsworth et al. *Phys. Rev. C* 8 (1973), pp. 216–229. DOI: 10.1103/PhysRevC.8.216. URL: https://link.aps.org/doi/10.1103/PhysRevC.8.216

[109] H. Langhoff and H.-H. Hennies. *Zeitschrift für Physik* 164.2 (1961), pp. 166–173. DOI: 10.1007/BF01377806. URL: https://doi.org/10.1007/BF01377806

[110] Hans Ryde, Pedro Thieberger, and Torsten Alväger. *Phys. Rev. Lett.* 6 (1961), pp. 475–478. DOI: 10.1103/PhysRevLett.6.475. URL: https://link.aps.org/doi/10.1103/PhysRevLett.6.475

[111] Gilbert Sutter. PhD thesis. 1963, pp. 323–351. DOI: 10.1051/anphys/196313080323. URL: https://doi.org/10.1051/anphys/196313080323

[112] H Ryde. *Arkiv Fysik* 23 (1963). URL: https://www.osti.gov/biblio/4728283

[113] J.C. Vanderleeden and P.S. Jastram. *Physics Letters* 19.1 (1965), pp. 27–29. DOI: https://doi.org/10.1016/0031-9163(65)90950-9. URL: https://www.sciencedirect.com/science/article/pii/0031916365909509

[114] J. C. Vanderleeden and P. S. Jastram. *Phys. Rev. C* 1 (1970), pp. 1025–1035. DOI: 10.1103/PhysRevC.1.1025. URL: https://link.aps.org/doi/10.1103/PhysRevC.1.1025

[115] Yasuyuki Nakayama. *Phys. Rev. C* 7 (1973), pp. 322–330. DOI: 10.1103/PhysRevC.7.322. URL: https://link.aps.org/doi/10.1103/PhysRevC.7.322

[116] Y. Asano and C.S. Wu. *Nuclear Physics A* 215.3 (1973), pp. 557–569. DOI: https://doi.org/10.1016/0375-9474(73)90488-0. URL: https://www.sciencedirect.com/science/article/pii/0375947473904880

[117] J. Henderson et al. *Physical Review C* 89 (2014), p. 064307. DOI: 10.1103/PhysRevC.89.064307. URL: https://link.aps.org/doi/10.1103/PhysRevC.89.064307

[118] G.J. McCallum, D.A. Bromley, and J.A. Kuehner. *Nuclear Physics* 20 (1960), pp. 382–394. DOI: https://doi.org/10.1016/0029-5582(60)90181-4. URL: https://www.sciencedirect.com/science/article/pii/0029558260901814

[119] Gorjana Jerbić-Zorc et al. *Fizika (Zagreb)* 22.2 (1990), pp. 413–422. URL: https://www.bib.irb.hr:8443/525407

[120] K. Knauf and H. Sommer. *Zeitschrift für Physik* 183.1 (1965), pp. 10–24. DOI: 10.1007/BF01384431. URL: https://doi.org/10.1007/BF01384431

[121] Ksenofont Ilakovac et al. *Fizika* 20.1 (1988), pp. 91–98. URL: https://www.bib.irb.hr:8443/525421

[122] Z. Grabowski, S. Gustafsson, and G. Bäckström. *Nuclear Physics* 38 (1962), pp. 648–653. DOI: https://doi.org/10.1016/0029-5582(62)91075-1. URL: https://www.sciencedirect.com/science/article/pii/0029558262910751

[123] E. L. Church and T. R. Gerholm (1965). URL: https://www.osti.gov/servlets/purl/4567165

[124] E. L. Church and T. R. Gerholm. *Phys. Rev.* 143 (1966), pp. 879–894. DOI: 10.1103/PhysRev.143.879. URL: https://link.aps.org/doi/10.1103/PhysRev.143.879

[125] Torsten Alväger and Hans Ryde. *Phys. Rev. Lett.* 4 (1960), pp. 363–364. DOI: 10.1103/PhysRevLett.4.363. URL: https://link.aps.org/doi/10.1103/PhysRevLett.4.363

[126] Ali A. Abdulla. PhD thesis. Oklahoma State University, 1969

[127] Werner Beusch. PhD thesis. 1960. DOI: https://doi.org/10.3929/ethz-a-000090199

[128] Christopher Walz. en. PhD thesis. Darmstadt: Technische Universität, 2014. URL: http://tuprints.ulb.tu-darmstadt.de/4056/

[129] C. Walz et al. *Nature* 526 (2015), pp. 406–409. DOI: 10.1038/nature15543. URL: https://www.nature.com/articles/nature15543

[130] P.-A. Söderström et al. *Nature Communications* 11 (2020), p. 3242. DOI: 10.1038/s41467-020-16787-4. URL: https://www.nature.com/articles/s41467-020-16787-4

[131] José Nicolás Orce, Cebo Ngwetsheni, and B. Alex Brown. *Phys. Rev. C* 108 (2023), p. 044309. DOI: 10.1103/PhysRevC.108.044309. URL: https://link.aps.org/doi/10.1103/PhysRevC.108.044309

[132] Swati Garg et al. *Atomic Data and Nuclear Data Tables* 150 (2023), p. 101546. DOI: 10.1016/j.adt.2022.101546. URL: https://www.sciencedirect.com/science/article/pii/S0092640X22000468

[133] Yu.A Litvinov et al. *Physics Letters B* 573 (2003), pp. 80–85. DOI: 10.1016/j.physletb.2003.08.077. URL: http://www.sciencedirect.com/science/article/pii/S0370269303013479

[134] Brookhaven National Laboratory. 2020. URL: https://www.nndc.bnl.gov/ensdf/

[135] Gerd Braun, Andreas Bockisch, and Wolfgang Neuwirth. *Nuclear Instruments and Methods in Physics Research* 224.1 (1984), pp. 112–116. DOI: https://doi.org/10.1016/0167-5087(84)90454-X. URL: https://www.sciencedirect.com/science/article/pii/016750878490454X

[136] W. Henning. *Nuclear Physics A* 734 (2004), pp. 654–660. DOI: https://doi.org/10.1016/j.nuclphysa.2004.01.119. URL: https://www.sciencedirect.com/science/article/pii/S0375947404001393

[137] R. Loetzsch et al. *Nature* 625.7996 (2024), pp. 673–678. DOI: 10.1038/s41586-023-06910-y. URL: https://doi.org/10.1038/s41586-023-06910-y

[138] Evan Williams et al. *Nuclear Instruments and Methods in Physics Research Section B: Beam Interactions with Materials and Atoms* 548 (2024), p. 165248. DOI: https://doi.org/10.1016/j.nimb.2024.165248. URL: https://www.sciencedirect.com/science/article/pii/S0168583X2400017X

[139] Gerhard Kraft. *GSI Helmholtzzentrum für Schwerionen forschung GmbH, Planckstraße* 2.64 (2013), p. 291. URL: https://three.jsc.nasa.gov/articles/Krafts_GSI.pdf

[140] W. Korten (spokesperson) et al. Experiment Proposal. 2021. URL: https://wiki.gsi.de/pub/ESR_EXP/E143Experiment/E143%20Two-photon%20decay-proposal.pdf

[141] GSI Helmholtzzentrum für Schwerionenforschung GmbH. https://www.gsi.de/en/researchaccelerators/accelerator_facility. Accessed: April 7, 2024

[142] H. Geissel et al. *Nuclear Instruments and Methods in Physics Research Section B: Beam Interactions with Materials and Atoms* 70.1 (1992), pp. 286–297. DOI: https://doi.org/10.1016/0168-583X(92)95944-M. URL: https://www.sciencedirect.com/science/article/pii/0168583X9295944M

[143] K. Abrahamsson et al. *Nuclear Instruments and Methods in Physics Research Section B: Beam Interactions with Materials and Atoms* 79.1 (1993), pp. 269–272. DOI: https://doi.org/10.1016/0168-583X(93)95341-2. URL: https://www.sciencedirect.com/science/article/pii/0168583X93953412

[144] M. Lestinsky et al. *The European Physical Journal Special Topics* 225.5 (2016), pp. 797–882. DOI: 10.1140/epjst/e2016-02643-6. URL: https://doi.org/10.1140/epjst/e2016-02643-6

[145] H.-J. Kluge et al. *Current Trends in Atomic Physics*. Ed. by S. Salomonson and E. Lindroth. Vol. 53. Advances in Quantum Chemistry. Academic Press, 2008, pp. 83–98. DOI: https://doi.org/10.1016/S0065-3276(07)53007-8. URL: https://www.sciencedirect.com/science/article/pii/S0065327607530078

[146] F. P. Lossing and Ikuzo Tanaka. *The Journal of Chemical Physics* 25.5 (1956), pp. 1031–1034. DOI: 10.1063/1.1743092. eprint: https://pubs.aip.org/aip/jcp/article-pdf/25/5/1031/18811378/1031_1_online.pdf. URL: https://doi.org/10.1063/1.1743092

[147] K H Becker and V Tarnovsky. *Plasma Sources Science and Technology* 4.2 (1995), p. 307. DOI: 10.1088/0963-0252/4/2/015. URL: https://dx.doi.org/10.1088/0963-0252/4/2/015

[148] P. Spädtke et al. *Review of Scientific Instruments* 69.2 (1998), pp. 1079–1081. DOI: 10.1063/1.1148638. eprint: https://pubs.aip.org/aip/rsi/article-pdf/69/2/1079/19172644/1079_1_online.pdf. URL: https://doi.org/10.1063/1.1148638

[149] Mario Conte and William W. MacKay. 2008. DOI: 10.1142/6683

[150] William A. Friedman. *Phys. Rev. C* 27 (1983), pp. 569–577. DOI: 10.1103/PhysRevC.27.569. URL: https://link.aps.org/doi/10.1103/PhysRevC.27.569

[151] O.B. Tarasov and D. Bazin. *Nuclear Physics A* 746 (2004). Proceedings of the Sixth International Conference on Radioactive Nuclear Beams (RNB6), pp. 411–414. DOI: https://doi.org/10.1016/j.nuclphysa.2004.09.063. URL: https://www.sciencedirect.com/science/article/pii/S0375947404010048

[152] M S Sanjari et al. *Physica Scripta* 2013.T156 (2013), p. 014088. DOI: 10.1088/0031-8949/2013/T156/014088. URL: https://dx.doi.org/10.1088/0031-8949/2013/T156/014088

[153] M. S. Sanjari et al. *Review of Scientific Instruments* 91.8 (2020), p. 083303. DOI: 10.1063/5.0009094. URL: https://doi.org/10.1063/5.0009094

[154] Swapan Chattopadhyay. CERN Yellow Reports: Monographs. Geneva: CERN, 1984. DOI: 10.5170/CERN-1984-011. URL: https://cds.cern.ch/record/155458

[155] Mohammad Shahab Sanjari. doctoralthesis. Universitätsbibliothek Johann Christian Senckenberg, 2013, pp. IX, 164. URL: http://publikationen.ub.uni-frankfurt.de/frontdoor/index/index/docId/29902

[156] Friedhelm Caspers (2009). DOI: 10.5170/CERN-2009-005.407. URL: http://cds.cern.ch/record/1213284

[157] C Trageser et al. *Physica Scripta* 2015.T166 (2015), p. 014062. DOI: 10.1088/0031-8949/2015/T166/014062. URL: https://dx.doi.org/10.1088/0031-8949/2015/T166/014062

[158] Christian Trageser. de. PhD thesis. Justus Liebig University Giessen, 2018. DOI: 10.22029/JLUPUB-9788. URL: https://jlupub.ub.uni-giessen.de//handle/jlupub/10404

[159] M. S. Sanjari. *Zenodo* 7615693 (2023). DOI: 10.5281/zenodo.7615693. URL: https://zenodo.org/record/7615693

[160] E143 Collaboration. GSI Helmholtz Center for Heavy Ion Research. 2024. URL: https://elog.gsi.de/esr/E143/page

[161] David Freire-Fernández. Version v1.0.0 (2023). DOI: 10.5281/zenodo.8172227. URL: https://doi.org/10.5281/zenodo.8172227

[162] David Freire-Fernández and George Hudson-Chang. *Zenodo* 8169341 (2023). DOI: 10.5281/zenodo.8169341. URL: https://zenodo.org/record/8169341

[163] Georges Audi, Walter G. Davies, and Graham E. Lee-Whiting. *Nuclear Instruments and Methods in Physics Research Section A: Accelerators, Spectrometers, Detectors and Associated Equipment* 249.2 (1986), pp. 443–450. DOI: https://doi.org/10.1016/0168-9002(86)90700-X. URL: https://www.sciencedirect.com/science/article/pii/016890028690700X

[164] Y. A. Litvinov. PhD thesis. University of Giessen, 2003

[165] M. Matoš. PhD thesis. University of Giessen, 2004

[166] D. Shubina. PhD thesis. University of Heidelberg, 2012

[167] T. Radon et al. *Nuclear Physics A* 677.1 (2000), pp. 75–99. DOI: https://doi.org/10.1016/S0375-9474(00)00304-3. URL: https://www.sciencedirect.com/science/article/pii/S0375947400003043

[168] David Freire-Fernández. https://github.com/DFreireF/rionmass. 2024

[169] Meng Wang et al. *Chinese Physics C* 45.3 (2021). The numerical table used was taken from the Atomic Mass Data Center: https://www-nds.iaea.org/amdc/, p. 030003. DOI: 10.1088/1674-1137/abddaf. URL: https://doi.org/10.1088/1674-1137/abddaf

[170] A. Kramida et al. NIST Atomic Spectra Database (ver. 5.11), [Online]. Available: https://physics.nist.gov/asd [2024, January 24]. National Institute of Standards and Technology, Gaithersburg, MD. 2023

[171] Shahab Sanjari. https://github.com/xaratustrah/barion. 2023

[172] F. G. Kondev et al. *Chinese Physics C* 45.3 (2021), p. 030001. DOI: 10.1088/1674-1137/abdd52

[173] Yu. A. Litvinov et al. *Phys. Rev. Lett.* 99 (2007), p. 262501. DOI: 10.1103/PhysRevLett.99.262501. URL: https://link.aps.org/doi/10.1103/PhysRevLett.99.262501

[174] Yu.A. Litvinov et al. *Phys. Lett. B* 664 (2008), pp. 162–168. DOI: 10.1016/j.physletb.2008.04.062. URL: http://www.sciencedirect.com/science/article/pii/S0370269308005613

[175] P. Kienle et al. *Physics Letters B* 726.4 (2013), pp. 638–645. DOI: https://doi.org/10.1016/j.physletb.2013.09.033. URL: https://www.sciencedirect.com/science/article/pii/S0370269313007624

[176] F.C. Ozturk et al. *Physics Letters B* 797 (2019), p. 134800. DOI: https://doi.org/10.1016/j.physletb.2019.134800. URL: https://www.sciencedirect.com/science/article/pii/S0370269319305040

[177] M. Shahab Sanjari. personal communication. 2023

[178] Z. Ge et al. *Phys. Rev. C* 103 (2021), p. 065502. DOI: 10.1103/PhysRevC.103.065502. URL: https://link.aps.org/doi/10.1103/PhysRevC.103.065502

[179] I. Mardor et al. *Phys. Rev. C* 103 (2021), p. 034319. DOI: 10.1103/PhysRevC.103.034319. URL: https://link.aps.org/doi/10.1103/PhysRevC.103.034319

[180] D. Freire-Fernández et al. (2023). arXiv: 2312.11313 [nucl-ex]

[181] M. Honma et al. *Phys. Rev. C* 80 (2009), p. 064323. DOI: 10.1103/PhysRevC.80.064323. URL: https://link.aps.org/doi/10.1103/PhysRevC.80.064323

[182] S. R. Johnson et al. *Phys. Rev. C* 108 (2023), p. 024315. DOI: 10.1103/PhysRevC.108.024315. URL: https://link.aps.org/doi/10.1103/PhysRevC.108.024315

[183] A.D. Ayangeakaa et al. *Physics Letters B* 754 (2016), pp. 254–259. DOI: https://doi.org/10.1016/j.physletb.2016.01.036. URL: https://www.sciencedirect.com/science/article/pii/S0370269316000538

[184] A.D. Ayangeakaa et al. *Physics Letters B* 754 (2016), pp. 254–259. DOI: 10.1016/j.physletb.2016.01.036. URL: https://www.sciencedirect.com/science/article/pii/S0370269316000538

[185] D. Abriola and A.A. Sonzogni. *Nuclear Data Sheets* 111.1 (2010), pp. 1–140. DOI: https://doi.org/10.1016/j.nds.2009.12.001. URL: https://www.sciencedirect.com/science/article/pii/S0090375209001136

[186] Léo Morel et al. *Nature* 588.7836 (2020), pp. 61–65. DOI: 10.1038/s41586-020-2964-7. URL: https://doi.org/10.1038/s41586-020-2964-7

[187] Yuri A Litvinov and Fritz Bosch. *Reports on Progress in Physics* 74 (2011), p. 016301. DOI: 10.1088/0034-4885/74/1/016301. URL: https://doi.org/10.1088%5C%2F0034-4885%5C%2F74%5C%2F1%5C%2F016301

[188] Jun Chen and Balraj Singh. *Nuclear Data Sheets* 164 (2020), pp. 1–477. DOI: https://doi.org/10.1016/j.nds.2020.01.001. URL: https://www.sciencedirect.com/science/article/pii/S0090375220300016

[189] Wolfram Korten et al. GSI Research Proposal. 2022. URL: https://gate.gsi.de/cgi-bin/gate?NJOB=PDF;JOB=proppdf;pnr=281;MID=3

[190] B.P. (Spokesperson) Crider et al. Experimental Proposal. 2023

[191] D. Abriola and A.A. Sonzogni. *Nuclear Data Sheets* 111.1 (2010), pp. 1–140. DOI: https://doi.org/10.1016/j.nds.2009.12.001. URL: https://www.sciencedirect.com/science/article/pii/S0090375209001136

[192] E. Bouchez et al. *Phys. Rev. Lett.* 90 (2003), p. 082502. DOI: 10.1103/PhysRevLett.90.082502. URL: https://link.aps.org/doi/10.1103/PhysRevLett.90.082502

[193] Balraj Singh. *Nuclear Data Sheets* 130 (2015), pp. 21–126. DOI: https://doi.org/10.1016/j.nds.2015.11.002. URL: https://www.sciencedirect.com/science/article/pii/S0090375215000563

[194] J.C. Batchelder, A.M. Hurst, and M.S. Basunia. *Nuclear Data Sheets* 183 (2022), pp. 1–346. DOI: https://doi.org/10.1016/j.nds.2022.06.001. URL: https://www.sciencedirect.com/science/article/pii/S009037522200031X

[195] Balraj Singh and Jun Chen. *Nuclear Data Sheets* 169 (2020), pp. 1–390. DOI: https://doi.org/10.1016/j.nds.2020.10.001. URL: https://www.sciencedirect.com/science/article/pii/S0090375220300430

[196] Coral M. Baglin. *Nuclear Data Sheets* 113.8 (2012), pp. 1871–2111. DOI: https://doi.org/10.1016/j.nds.2012.08.001. URL: https://www.sciencedirect.com/science/article/pii/S0090375212000579

[197] Bosch, F. et al. *EPJ Web Conf.* 123 (2016), p. 04003. DOI: 10.1051/epjconf/201612304003. URL: https://doi.org/10.1051/epjconf/201612304003

[198] P. Spiller and G. Franchetti. *Nuclear Instruments and Methods in Physics Research Section A: Accelerators, Spectrometers, Detectors and Associated Equipment* 561.2 (2006). Proceedings of the Workshop on High Intensity Beam Dynamics, pp. 305–309. DOI: https://doi.org/10.1016/j.nima.2006.01.043. URL: https://www.sciencedirect.com/science/article/pii/S0168900206000507

[199] J.C. Yang et al. *Nuclear Instruments and Methods in Physics Research Section B: Beam Interactions with Materials and Atoms* 317 (2013). XVIth International Conference on ElectroMagnetic Isotope Separators and Techniques Related to their Applications, December 2–7, 2012 at Matsue, Japan, pp. 263–265. DOI: https://doi.org/10.1016/j.nimb.2013.08.046. URL: https://www.sciencedirect.com/science/article/pii/S0168583X13009877

[200] Pauli Virtanen et al. *Nature Methods* 17 (2020), pp. 261–272. DOI: 10.1038/s41592-019-0686-2. URL: https://doi.org/10.1038/s41592-019-0686-2